Novel Methods of Optical Data Analysis to Assess Radiation

Responses in the Tumor Microenvironment

by

Andrew Nicholas Fontanella

Department of Biomedical Engineering
Duke University

Date:_____

Approved:

_____

Mark Dewhirst, Supervisor

_____

Joseph Izatt

_____

Bruce Klitzman

_____

Nimmi Ramanujam

_____

Victoria Seewaldt

Dissertation submitted in partial fulfillment of
the requirements for the degree of Doctor
of Philosophy in the Department of
Biomedical Engineering in the Graduate School
of Duke University

2013

ABSTRACT

Novel Methods of Optical Data Analysis to Assess Radiation

Responses in the Tumor Microenvironment

by

Andrew Nicholas Fontanella

Department of Biomedical Engineering
Duke University

Date:_____
Approved:

_____
Mark Dewhirst, Supervisor

_____
Joseph Izatt

_____
Bruce Klitzman

_____
Nimmi Ramanujam

_____
Victoria Seewaldt

An abstract of a dissertation submitted in partial
fulfillment of the requirements for the degree
of Doctor of Philosophy in the Department of
Biomedical Engineering in the Graduate School of
Duke University

2013

Abstract

The vascular contribution to tumor radiation response is controversial, but may have profound clinical implications. This is especially true of a new class of radiation therapies which employ spatial fractionation techniques—high radiation doses delivered in a spatially modulated pattern across the tumor. Window chamber tumor models may prove useful in investigating vascular parameters due to their facilitation of non-invasive, serial measurements of living tumors. However, presently there do not exist automated and accurate algorithms capable of quantitatively analyzing window chamber data.

Here we attempt to address these two problems through (1) the generation of novel optical data processing techniques for the quantification of vascular structural and functional parameters, and (2) the application of these methods to the study of vascular radiation effects in window chamber models.

Results presented here demonstrate the versatility and functionality of the data processing methods that we have developed. In the first part of Aim 1, we have developed a vessel segmentation algorithm specifically designed for processing tumor vessels, which present a challenge to existing algorithms due to their highly branching, tortuous structure. This provides us with useful information on vascular structural parameters. In the second part of Aim 1, we demonstrate a complementary vascular

functional analysis algorithm, which generates quantitative maps of speed and direction. We prove the versatility of this method by applying it to a number of different studies, including hemodynamic analysis in the dorsal window chamber, the pulmonary window, and after neural electro-stimulation. Both the structural and functional techniques are shown capable of generating accurate and unbiased vascular structural and functional information. Furthermore, that automated nature of these algorithms allow for the rapid and efficient processing of large data sets. These techniques are validated against existing techniques.

The application of these methods to the study of vascular radiation effects produced invaluable quantitative data which suggest startling tumor adaptations to radiation injury. Window chamber grown tumors were treated with either widefield, microbeam, or mock irradiation. After microbeam treatment, we observed a profound angiogenic effect within the radiation field, and no signs of vascular disruption. Upregulation of HIF-1, primarily in the tumor rim, suggested that this response may have been due to bystander mechanisms initiated by oxidative stress. This HIF-1 response may have also initiated an epithelial-mesenchymal transition in the cells of the tumor rim, as post-treatment observation revealed evidence of tumor cell mobilization and migration away from the primary tumor to form secondary satellite clusters. These data indicate the possibility of significant detrimental effects after microbeam treatment facilitated through a HIF-1 response.

Dedication

This work is dedicated to Roberta Ritter, who was an inspiration in many ways.

Contents

List of Tables

List of Figures

Acknowledgements

1. Background and Rationale

Despite persistent advances in early detection and treatment, cancer has remained the second most likely cause of death in the United States for the past 75 years, behind only heart disease[1]. Approximately one quarter of all deaths this year will be the result of a cancerous malignancy, a figure that has consistently grown in proportion over the same 75 year time period (Figure 1).
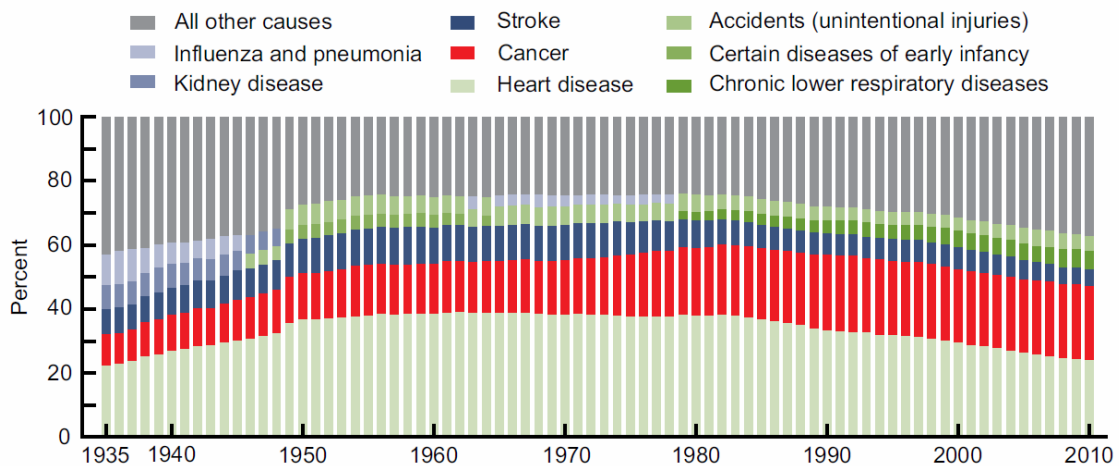
Figure 1: Causes of Death from 1935-2010: Over this timespan, death due to cancer has consistently increased as a percentage of all combined causes of death. (From ref. 1: public domain)

As a disease, cancer often carries with it a devastating psychological factor that stems in no small part from the impact it has upon the sufferer's quality of life. Treatments intended to cure the disease may in many cases contribute significantly to this drop in quality—a result of severe side-effects and complications that are not

uncommon in many instances of the disease. Furthermore, the financial cost associated

with the cancer treatment is staggering. A recent estimate of the total cost of care in the

US was $89 billion in one year alone[2]. When indirect costs associated with loss of

productivity and death are factored in, the total cost of the disease exceeds $200 billion.

This figure has been growing yearly, along with its proportional contribution to total

health care costs.

Such statistics would seem to imply inefficient spending and marginal advances

in the treatment of the disease over the past decades. However, these figures fail to

distinguish cancer as a diverse collection of diseases, each with its own evolving

prevalence, treatment protocols, and prognosis, within the context of a similarly

evolving national demographic profile. For example, between 1975 and 2007, the US

saw a doubling in the age-adjusted death rate among females due to pulmonary and

bronchial carcinomas, according to a historical analysis of cancer prevalence and

outcome[3]. Over the same period, though, five-year survival rates for this same class of

cancers increased significantly. Taken together, these data suggest that the dramatic

increase in the *incidence* of lung and bronchial cancers (associated with increases in the

prevalence of smoking among women in the preceding decades[4]) was the primary factor

in the continual rise in death rates; advances in treatment could not completely

compensate for this, despite their success in achieving a better individual chance of

survival.

Such advances in treatment efficacy over the past decades are common among a broad range of cancers. In fact, the five-year survival rates for 23 out of the 24 major cancer types considered in the aforementioned study all increased significantly over this same period. However, these advances in care are often accompanied by increases in cost and resources, along with uncertainties as to the safest and most efficient modes of delivery. And within the context of an aging society, the strain imposed by the expected increases in total cancer diagnoses highlights this urgent need for more efficient and effective treatments.

It is therefore paramount that cancer research not only works towards the discovery of new therapies, but it must also make a concerted investigation into the basic biological mechanisms involved. It is only through this understanding of effects at the most basic biological level that a large scale assessment of ideal treatment plans can be achieved. Thus, the discovery of underlying facets of treatment response will allow the therapies to be administered more efficiently, safely, and effectively.

1.1 The Tumor Lifecycle

1.1.1 Tumorigenesis

The transformation of a normally functioning cell to a cancerous one involves a variable number of mutations which alter the genetically encoded mechanisms controlling cellular metabolism, genomic integrity, cell-to-cell interactions, survival, proliferation, etc. The number of mutations necessary for a malignant transformation

varies according to cancer type. They can be as few as two, but may often be many more[5,6]. These mutations tend to be specific to certain genes that are commonly mutated across a broad range of cancer types. Furthermore, these mutations may need to occur in a specific sequence in order to avoid the initiation of apoptosis (a form of programmed cell death).

The two classes of genes whose mutations are implicated in oncogenic transformation are tumor suppressor genes and proto-oncogenes[7]. Tumor suppressor genes encode proteins that are involved in maintaining the integrity of the genome, regulating the cell cycle, and initiating an apoptotic response to potentially harmful and irreparable DNA damage. p53 is the preeminent protein in this class, and its inhibition through mutation or deletion has been observed in greater than 50% of human tumors[8]. The other class, proto-oncogenes, consists of genes that have the potential to contribute to cancer through their mutation or overexpression. These genes typically serve as regulators of cellular metabolism, proliferation, or differentiation. The alteration of their functionality due to a number of possible factors (e.g. mutation, modification of regulatory regions, changes in upstream regulatory elements, translocation) can lead to deregulation of these functions and tumor initiation.

1.1.2 Tumor Growth and Survival

1.1.2.1 Hallmarks of Cancer

In a model of cancer put forth by Hanahan and Weinberg in 2000, the modification of cellular functionality elicited by mutation requires six essential components for a complete oncogenic transformation and tumor viability[9]. Two additional hallmarks were later added due to an emergent body of research which indicated additional requirement[10]. The model was also expanded to include enabling characteristics which promote tumor development, but are not strictly vital components (Figure 2).
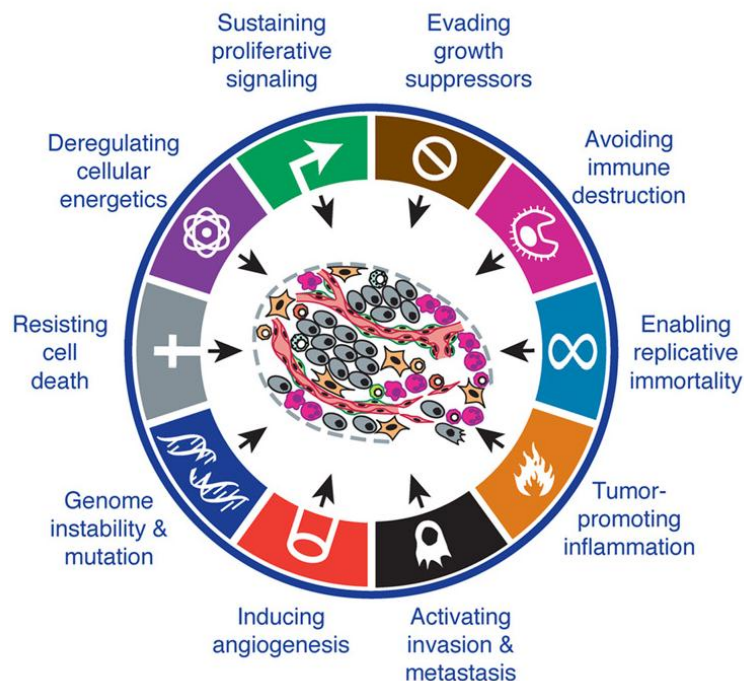
Figure 2: Hanahan's and Weinberg's Hallmarks of Cancer: Complete oncogenic transformation is achieved through the acquisition of eight essential components. Two enabling characteristics help drive this process. (From ref. 10: permission from pub.)

First, sustained proliferative signaling must be achieved. This is one of the most fundamental aspects of malignancy and is achieved through the deregulation of the cellular cycle of growth and proliferation. The next (and related) hallmark of cancer is the evasion of growth suppressors. Not only must the cell acquire the ability to upregulate proliferative factors, but it must also overcome the influence of negative regulators of cellular proliferation.

The third hallmark of cancer is resistance to cell death. This can occur after the inactivation or absence of tumor suppressor proteins which would normally initiate an apoptotic response to dysregulated gene expression or after exposure to environmental stimuli typically found in the tumor microenvironment (low oxygen supply, high acidity, etc.)

Fourth is the enabling of replicative immortality. Most differentiated cell types have a limited replicative potential do to the degradation of the chromosomal end caps, known as telomeres, which are progressively shortened during each instance of mitosis. This shortening is due to the inability of the cell to replicate the very end regions of its DNA, resulting in a progressive loss of these non-encoding end regions. However, eventually the telomeres will be degraded nearly completely, and cell division can no longer occur without the loss of functional DNA. The cell has, at this point, reached its "Hayflick limit", the total number of divisions the cell lineage is ultimately capable of.

Tumors are able to escape this limit through the expression of telomerase, an enzyme that regenerates telomeres, enabling unlimited replicative potential[11].

The fifth hallmark is the induction of angiogenesis, which will be more thoroughly discusses in a later section. This involves the proliferation of blood vessels to supply vital oxygen and nutrients to the expanding tumor. This process may be intimately linked with the sixth hallmark, activation of invasion and metastasis, as the study presented here suggests.

An emerging hallmark of cancer is the reprogramming of energy metabolism. While this aspect of tumor viability was only recently added to Hanahan's and Weinberg's model, it has been long known that tumors alter their metabolism to make greater use of anaerobic glycolysis. Although a normally employed metabolic pathway under hypoxic conditions, Otto Warburg first noted that some cancers tend to preferentially employ this process even when oxygen is plentiful enough to employ more efficient aerobic metabolism[12,13]. This is known as the "Warburg Effect". The reasons for this alteration in metabolism are still not thoroughly understood, but one theory suggests that anaerobic glycolysis allows for the enhanced incorporation of intermediate products into biosynthetic pathways, thereby facilitating more rapid cellular proliferation[14,15]. Recent work has also shown that two different subpopulations of cells may exist symbiotically in tumors: one preferentially employing anaerobic

glycolysis, the other preferentially importing and utilizing as an energy source the

lactate produced by this reaction[16].

The second emerging hallmark is the evasion of immune destruction. Current

understanding suggests that the immune system is an efficient mechanism for detecting

and eliminating the majority of incipient tumors within the body. An ability to evade

immune response is therefore early adaptation necessarily acquired by the tumor in

order to avoid destruction.

The two newly proposed enabling characteristics of cancer are genomic

instability and tumor-promoting inflammation. Genomic instability allows for the rapid

acquisition of mutations which represent a micro-evolutionary mechanism by which

tumors cells are selected for survival characteristics such as metabolic adaptation,

inhibition of apoptosis, treatment resistance, etc. As part of a normal injury response

coopted as a tumor-promoting mechanism, tumor-promoting inflammation may

provide important pro-survival, proliferation, and angiogenic signaling molecules,

along with paths of invasion and metastasis generated through the degradation of the

extracellular matrix.

As highlighted in a number of these hallmarks, sustained tumor growth and

survival are achieved through complex interactions among (genetically) normal tissues.

These interactions are typically aspects of beneficial, non-pathological processes that are

dysregulated and ultimately utilized by the tumor as pathological mechanisms. A

specific cycle of interaction through which blood vessel growth and radiation therapy response are modulated by the tumor was elucidated by our lab. The central, driving components of this cycle are **H**ypoxia, **R**eactive Oxygen/Nitrogen Species, **H**IF-1, and **V**EGF. We refer to this as the HRHV axis (Figure 3).
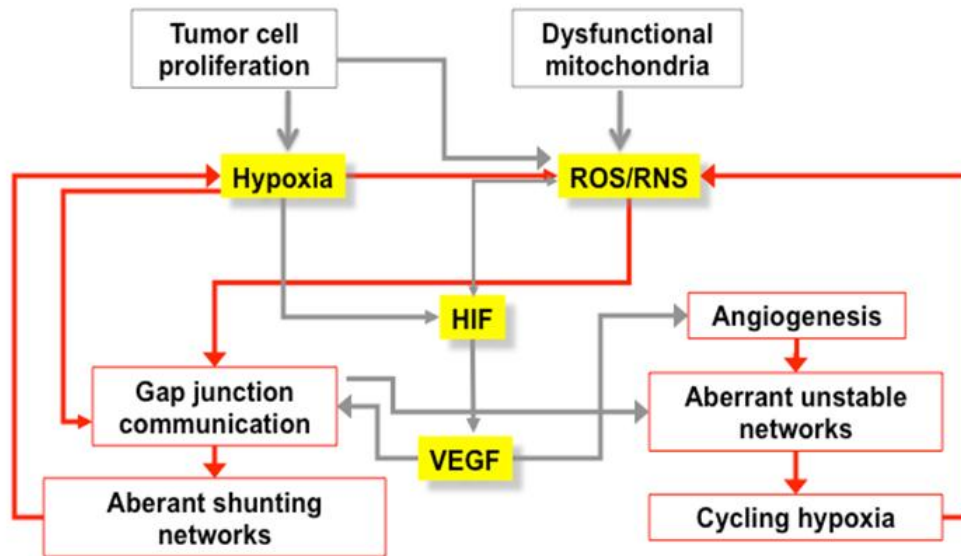
Figure 3: The HRHV Axis: Hypoxia, Reactive Oxygen/Nitrogen Species, HIF-1, and VEGF drive a cycle of angiogenesis and hypoxia which ultimately lead to detrimental changes in phenotype and treatment resistance.

1.1.2.2 The HRHV Axis

Hypoxia is a state of pathologically low oxygen tension in a tissue. Whereas most normally functioning organs have oxygen partial pressures greater than 20 mmHg, values below 10 mmHg will typically cause an alteration in gene expression in response

to this adverse condition[17]. Hypoxia is also a common feature among solid tumors, and it has been shown to have a negative effect on the management of many cancer types[18,19].

Hypoxia induces the expression of HIF-1 (of the family of hypoxia inducible factors)[20]. HIF-1 is a major transcription factor regulating cellular adaptation to low oxygen conditions[18], and one of the primary regulators of vascular endothelial growth factor (VEGF), a critical inducer of angiogenesis within tumors. Overexpression of HIF-1 has been observed in human breast, cervix, lung, brain, ovarian, and prostate cancers, and is thought to be a common feature among solid tumors in general[18]. Along with angiogenesis, studies have shown that HIF-1 is an important transcription factor for metabolic adaptation, apoptosis regulation, and metastasis—all of which are major aspects of tumorigenesis and tumor progression[17].

HIF-1 is also known to be expressed in an oxygen-independent manner through various mechanisms that are often associated with radiation therapy and other cytotoxic treatments. These mechanisms involve the production of free radicals—highly reactive chemical species with unpaired electrons. The two of the most biologically relevant free radicals include superoxide (O_2^-) and hydrogen peroxide (H_2O_2). Superoxide is a highly toxic chemical that is produced as a byproduct of mitochondrial respiration. In order to prevent cellular damage, superoxide is chemically processed by the superoxide dismutase enzyme to convert it to neutral oxygen and the much more chemically stable hydrogen peroxide[21].

Studies have shown that when reactive oxygen species are produced in large quantities, HIF-1α appears to be stabilized, even in the presence of oxygen. However, when cells were induced to overexpress catalase (an enzyme responsible for the chemical conversion of hydrogen peroxide into neutral oxygen and water), HIF-1α was degraded, indicating hydrogen peroxide facilitates its stabilization[22]. Nitric oxide also stabilizes HIF-1α in a hypoxia-independent manner that is highly relevant to radiation therapy response. (This process is detailed in a later section.) Additionally, reactive species tend to increase during periods of hypoxia, and these radicals also play a distinct role in hypoxia-*dependent* HIF-1 expression[23,24].

The four components of the HRHV feedback loop stimulate a pattern of tumor growth which promotes angiogenesis. Rather than improve the oxygenation state of the tumor, however, the disorganized vascular structure that tumor angiogenesis produces tends to limit oxygen delivery, and a state of spatial/temporal fluctuations in oxygen delivery emerges[24]. Normoxic cells will proliferate until they reach the oxygen perfusion limit and become hypoxic. Hypoxic cells will, in turn, drive free radical/HIF-1 production, stimulating angiogenesis and further exacerbating the malignant cycle. Additionally, many cytotoxic treatments have been shown to stimulate this cycle, indirectly leading to increased tumor aggression and resistance to future treatment. The HRHV axis thus presents a major therapeutic hurdle, and the hypoxia that results may lead to detrimental long term effects.

1.1.3 Metastasis

The migration of cancer cells to remote locations within the body is the ultimate

detrimental consequence of a series of oncogenic transformations. The formation of

metastatic nodes is typically associated with a drastically poorer prognosis than that of

locally controlled tumors of the same type. A tumor's capacity to progress to metastatic

disease is not a trivial process, however. It consists of a multi-step process of host tissue

invasion, lymph or blood vessel intravasation, transit through the invaded vasculature,

extravasation, and finally proliferation at the remote location[25]. A concurrent series of

changes in gene expression are often necessary to facilitate the mobility and survival of

these cells outside of their tissue of origin.

1.1.3.1 Epithelial to Mesenchymal Transition

Epithelial to mesenchymal transition (EMT) refers to changes in functional

behavior which enable cell migration during embryonic development, tissue

morphogenesis, or wound healing processes. This process induces morphological

changes within the cell, and they will begin to take on a characteristic fibroblast-like

appearance. The genetic mechanisms facilitating EMT may be exploited by carcinomas

during invasion and metastatic progression[26]. EMT is typically envisioned as a critical

transformation through which potentially metastatic cells escape the primary tumor and

avoid an apoptotic response normally induced by the loss of cell-to-cell contact.

Although this process is an implied characteristic of cancers of epithelial origin (i.e.

carcinomas, which constitute the majority of human cancers), its relevance to cancers of other origins is poorly understood.

The downregulation of the E-cadherin protein is one of the first steps in the carcinogenic process[27,28]. E-cadherin enables intercellular junctions that bind sheets of epithelial cells together. The loss of this protein, concurrent with the upregulation of adhesion molecules associated with cell migration (such as N-cadherin), enable cellular detachment. The expression of various enzymes that degrade the basement membrane/extracellular matrix allow these detached cells to overcome physical barriers to migration. Finally, the release of angiogenic factors attracts vascular modes of metastasis and induces vascular permeability, easing the intravasation process[29].

It is unclear if and to what extent this mesenchymal phenotype persists after metastatic colonization. The reverse process of mesenchymal to epithelial transition is proposed to play a role in the successful growth of metastatic cells once they invade their target tissue[30]. This would help to explain the epithelial morphology and histopathological similarities of metastases to their primary tumor. Alternative hypotheses propose that these metastatic cells never have undergone EMT in the first place. In fact, the overall incidence of EMT and its requirement for metastatic spread is a controversial subject, and a number of researchers have insisted that its role has been significantly overstated[25].

1.1.3.2 Stromal Contributions to Metastasis

It has long been known that stromal interactions play a significant role in determining the success of metastatic colonization for remote tissues. In 1889, Stephen Paget compiled a report of the sites of metastasis in women who had died of breast cancer. He noted that certain organs were more commonly affected than others, leading him to propose the "seed and soil" cancer dissemination[31]. In this model, certain target organs (the soil) present a more hospitable environment for metastatic cells (the seeds) due to their various similarities to the cancer's tissue of origin. For example, melanomas show a propensity for brain metastasis, possibly due to common origination of both melanocytes and glia from the neural crest during embryogenesis[32].

It has also been show that the host stroma may help to initiate the process of metastasis within the primary tumor through paracrine signaling factors[33]. Tumor-associated macrophages, for instance, have been shown to secrete the proliferative epidermal growth factor (EGF) and assist in cellular intravasation, while tumor cells likewise stimulate these macrophages through the production of CSF-1 (a cytokine that regulates macrophage function)[34,35]. Furthermore, tumor infiltrating macrophages may assist in the degradation of the extracellular matrix at the tumor periphery, easing cellular motility[36,37].

1.1.3.3 Radiation-Induced EMT

The observation of EMT-positive markers in human tumors is associated with poor prognosis and resistance to therapy[38]. Mounting evidence suggests that radiation may play a direct role in stimulating this process. A number of preclinical studies have shown that cancer cells that survive radiation insult are more prone to migration and invasion, and metastatic growth may be potentiated[39,40]. *In vitro* studies by our collaborators in the lab of Mariano Garcia-Blanco have demonstrated that these *in vivo* effects may be facilitated by a radiation-induced EMT.

In their study, the gene sequence encoding a green fluorescent protein (GFP) was interrupted by an intron differentially expressed while the cell is in a mesenchymal state. Expression of functional GFP thus reports cells in the epithelial state. After exposure to radiation, the frequency of GFP expression was shown to decrease, suggesting that it had induced EMT (Figure 4).
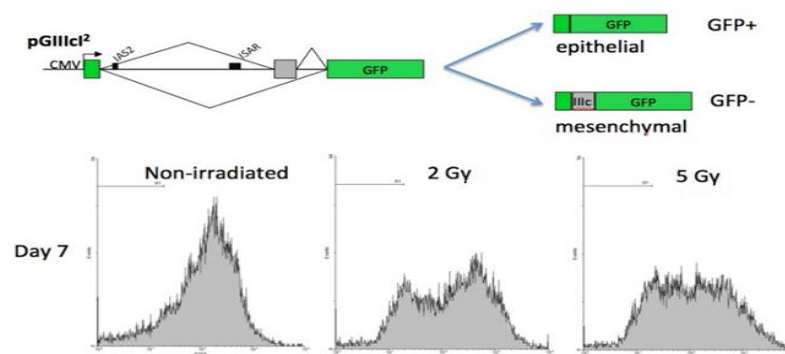
Figure 4: Radiation Induces EMT *In Vitro*: A reporter cell line was used to demonstrate the effects of radiation on cellular phenotype. After doses of two and five Gray, cells displayed a shift from an epithelial to a mesenchymal state (Garcia-Blanco, Dewhirst, and Somarelli: unpublished data).

The implications of this effect are clinically profound. If radiation is capable of effecting a transition of cancers to a more malignant phenotype, radiation therapies may be directly stimulating the metastatic spread of the disease in cells non-lethally irradiated. Clearly further investigation into this process is necessary in order to formulate strategies to counteract EMT in the tumors of patient undergoing radiation treatment.

1.2 The Tumor Microenviornment

1.2.1 Hypoxia and Hypoxia-Inducible Factors

Solid tumors are generally associated with a state of insufficient oxygen supply[41]. Tumor hypoxia originates from both deficiencies in the vascular network and from the rapid consumption of oxygen by proliferating tumor cells (**Error! Reference source not ound.**)[24]. High oxygen consumption rates and deficiencies in arterial supply will cause cells farther downstream from the tumor periphery to receive a relatively deoxygenated blood supply. Exacerbating this effect, irregularities in the vascular network lead to inefficient flow patterns and highly heterogeneous oxygen delivery rates. Furthermore, deoxygenated red blood cells will tend to adhere to one another, increasing blood viscosity and resistance to flow into already oxygen-starved tumor regions.
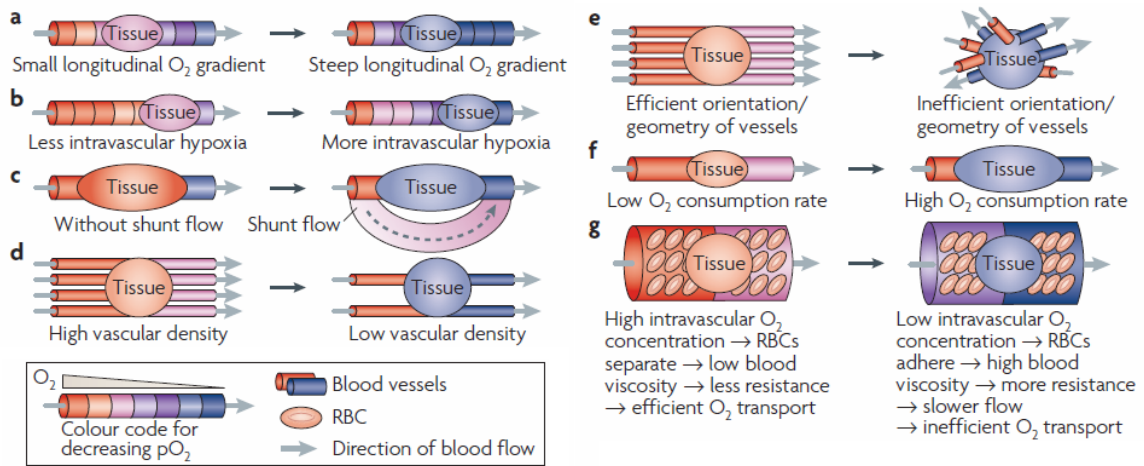
Figure 5: The Origins of Hypoxia in Tumors: Seven main sources of hypoxia are identified—the result of poorly regulated consumption rates in tumors and inefficient blood transport characteristics. (From ref. 24: permission from pub.)

Hypoxic cells will release angiogenic factors in an attempt to alleviate low oxygen supply through vascular proliferation. However, significant imbalances in angiogenesis regulation inevitably lead to a failure of the vascular network to furnish an ideal environment for cellular growth and survival. Angiogenic vessels are tortuous, leaky, and display little overall coordination in growth patterns. Rather than improve the delivery of oxygen to hypoxic cells, tumor angiogenesis will tend to exacerbate the condition on a global level.

The scarcity of important substrates delivered by blood vessels contributes to the tumor's pathophysiologic response to its harsh environment. Through complex signal transduction pathways, tumors will initiate ameliorative adaptations to hypoxia that

will contribute to resistance to many forms of treatment, including radiation[42],

chemotherapy[43], and perhaps even targeted agents, such as VEGF inhibitors.

Hypoxia also directly reduces the biological effect of x-ray radiation through

chemical processes; free radicals produced by radiation will react with DNA to modify

its chemical structure. In the absence of oxygen, the DNA can be chemically restored

after the initial interaction. However, when molecular oxygen is present, the formation

of an organic peroxide may occur. This "fixes" (makes permanent) the DNA lesion.

Under low-oxygen conditions, this chemical reaction is less likely, rendering hypoxic

cells more radio-resistant. This decreased treatment efficacy is exacerbated by the

tumor's selective adaptation to hypoxic conditions. For example, the tumor-suppressor

protein p53 triggers apoptosis under oxygen starvation; this leads to a selection for p53

mutated cells in which apoptosis is not stimulated by hypoxia, thus facilitating the

survival and expansion of cells that have adopted dangerous mutations[44].

1.2.1.1 Hypoxia-Independent HIF-1 Expression within the Context of Radiation Therapy

HIF-1's role as a hypoxia-mediated transcription factor is facilitated through its

depletion in an oxygen-rich environment. Structurally, HIF-1 is a heterodimer consisting

of α and β subunits[45]. Normally, HIF-1's α subunit is rapidly destroyed in the presence

of oxygen when oxygen-dependent prolyl hydroxylation of proline residues in its

oxygen-dependent degradation domain occurs. This marks the protein for proteosomal

degradation, facilitated by the von Hippel-Lindau protein complex. The oxygen-

dependent process yields HIF-1 significantly active primarily under hypoxic conditions[46-48].

HIF-1 has also been shown to be stabilized following radiation treatment, however, implicating it in many post-treatment tumor responses[49]. After radiation therapy, the tumor may experience a transient period of increased oxygenation, due to the death of the more radio-sensitive, oxygenated cells surrounding well-perfused vessels[50]. With the death of these cells and their halted consumption of substrates, more oxygen and nutrients are freed up for cells farther away from vessels. These cells, which were previously in hypoxic zones, now become normoxic. (A secondary source of reoxygenation may be an increase in vascular perfusion associated with decreased interstitial fluid pressure[51].) After reoxygenation, HIF-1 and a number of its downstream targets are expressed in an oxygen-independent manner through three different mechanisms.

The first mechanism involves the disassociation of stress granule aggregates after reoxygenation[49]. These stress granules form under adverse (e.g. hypoxic) conditions and are composed of complexes in which mRNA are sequestered to conserve energy by preventing their translation. Some of these mRNA will include HIF-1-regulated protein templates. When these mRNA are released in the newly normoxic environment, they are translated into their corresponding proteins in a process much delayed from their hypoxia-dependent transcription.

The second mechanism is the result the generation of reactive oxygen species. It had been previously shown that hypoxia increases mitochondrial reactive oxygen species production, which is sufficient to stabilize HIF-1α[52]. Our group then demonstrated that radiation-induced reoxygenation produces enough oxidative stress to enable reactive oxygen species-mediated stabilization[49].

The third mechanism involves the direct stabilization of HIF-1α through the S-nitrosylation of its oxygen-dependent degradation domain, which is mediated by nitric oxide[53]. One of the major sources of this nitric oxide is tumor-infiltrating macrophages. These macrophages will aggregate in the tumor after irradiation to clear out the cellular debris left after radiation-induced tumor cell death. As part of their immunological function, macrophages produce large quantities of nitric oxide, which stabilizes HIF-1 after their infiltration.

1.2.1.2 Cycling Hypoxia

In contrast to chronic hypoxia, certain regions of the tumor undergo fluctuations in oxygenation, an effect often referred to as "acute" or "cycling" hypoxia. (This effect is distinct from and should not be confused with the reoxygenation of the tumor after radiation treatment, as discussed previously.) These fluctuations tend to occur on two different time scales. Faster cycles (on the order of minutes to hours) have been observed in various animal models and within human tumors[54-58]. These are primarily due to fluctuations in red blood cell flux brought about through changes in flow

20

resistance[54,59]. Alterations in resistance may, in turn, be the result of vascular

intussusception[60], vasomotion[61,62], and uneven flow at bifurcation points[63]. Since blood

flow in tumors is unstable to begin with, minor variations in flow resistance in upstream

vessels may elicit profound effects in terms of the redirection of flow to downstream

locations[64,65]. Longer scale fluctuations in tumor oxygenation (on the order of hours to

days) have also been observed in human tumors[66]. These may be due to the relatively

rapid rate of vascular reorganization often observed in tumors[67].

As discussed previously, hypoxia-induced expression of HIF-1 is associated with

increased malignancy and treatment resistance in human tumors. This effect may be

even more pronounced in tumors subject to cycling hypoxia. Increased phosphorylation

of HIF-1 during cycling hypoxia, as well as increased free radical production during

repeated reoxygenation injury, leads to enhanced HIF-1 expression compared to cells

which are chronically hypoxic[68-72]. The implications of this effect during treatment-

induced alterations in oxygen delivery are currently poorly understood.

1.2.2 Angiogenesis

Angiogenesis occurs through a process of *endothelial sprouting* in which new

vessels branch from an existing vessel, and through *intussusception*, wherein endothelial

cells within an existing vessel form a longitudinally dividing column that bifurcates the

vessel[73]. Vasculogenesis is also an important aspect of vascular expansion.

Vasculogenesis involves the recruitment of bone marrow–derived endothelial-precursor

cells into the vascular architecture[74]. Whereas angiogenesis refers to endothelial cell proliferation and migration, vasculogenesis refers specifically to the de novo differentiation of endothelial cells from progenitor cells. While angiogenesis is known to be a major factor in tumor-mediated vascular proliferation, the role that vasculogenesis plays, especially after radiation therapy, is an area that is just beginning to be explored. Martin Brown proposed that after high dose irradiation of tissue beds, tumors depend upon vasculogenesis for endothelial cell repopulation. He showed that this is achieved through the infiltration of endothelial progenitor cells from the peripheral blood, assisted by bone marrow-derived myelomonocytes expressing MMP-9 (an extracellular matrix degrading enzyme)[75]. Notably, the endothelial progenitor cells were not themselves bone marrow-derived, suggesting a circulating repository of cells capable of initiating vasculogenesis.

The formation of new blood vessels and the remodeling of existing ones must inevitably lead to instability of flow and distribution of red blood cells within the developing vascular network[76]. The primary determinants of flow are pressure gradients and flow resistance. Flow resistance is extremely sensitive to changes in microvessel diameter (flow resistance is often modeled as inversely proportional to the fourth power of vessel radius) and the rheologic properties of the blood cells[77]. Despite the flourishing angiogenic activity that hypoxia induces, oxygen diffusion is hindered by the erratic and

22

inefficient structure of the newly formed vessels, and the hypoxic condition is not

rectified, even at the earliest stages of growth[67].

Tumor growth and metastasis are dependent upon angiogenesis[78]. It has

generally been thought that, as tumor cells expand beyond the oxygen diffusion

distance, the transcription factor HIF-1 is stabilized, and it begins to regulate

downstream angiogenic factors[17]. Recent results from our laboratory present a different

paradigm, suggesting that angiogenesis initiation may not require hypoxia or HIF-1

activation, but that HIF-1 activation is strongly associated with angiogenesis acceleration

(discussed in 1.2.4.1)[67].

1.2.3 Angiogenic Factors

1.2.2.1 Vascular Endothelial Growth Factor (A History of Discovery)

For more than a century, physicians and scientists have noted the abundant and

uniquely structured vasculature of tumors and speculated on the significance of this

finding. Indeed, the ubiquity of this observation led some researchers to propose that the

pathology of malignant tumor growth involved a corresponding disorder of the vascular

system[79].

However, insight into the proper role and mechanism of vascular proliferation

needed to wait until the early twentieth century and the emergence of in vivo imaging

technologies before its pathophysiologic significance could begin to be understood. In

1928, a window chamber model for the optical imaging of living tissue in a rabbit ear

was developed[80]. The model was later incorporated into rabbit carcinoma studies by

Gordon Ide, in 1939. Ide observed a strong correlation between vascular proliferation

and tumor expansion. This and following optical studies showed that the capacity of the

vascular endothelium to deliver oxygen and nutrients was a crucial rate-limiting step in

tumor progression[79]. It was now apparent that chemical growth factors must play some

role in the recruitment of blood vessels by the expanding tumor. Further discovery

was accelerated in 1943, when Glenn Algire pioneered the application of optical

methods to mouse tumor models. A paper discussing a number of the window

chambers he had developed was published in that year[81]. The most important of these

models among early cancer investigators would be the dorsal skin-fold chamber. Prior

to this development, *in vivo* optical measurements were performed primarily in rabbits,

dogs, and animals with ears large enough to facilitate a window chamber. With Algire's

murine model, the optical observation of tumors within the biologic sciences'

quintessential laboratory animal was developed.

In 1968, the interstitial diffusion of a proangiogenic growth factor was

demonstrated in hamster carcinoma studies by Melvin Greenblatt and Philippe Shubik.

They observed that the vascular response to a tumor transplanted into a hamster cheek

pouch was not inhibited by a semipermeable filter that separated the tumor from the

host tissue[82]. It was thus assumed that the growth factor researchers were looking for

could be characterized as an interstitial protein produced by tumor cells that induce

24

radical modifications to an otherwise healthy vasculature. With the basic properties and

mechanism of action established, work toward identifying the angiogenic factors began.

In 1983, Donald Senger and Harold Dvorak were able to identify a protein that

induced vascular leakage. The protein was named vascular permeability factor, or VPF[83].

A few years later, Napoleone Ferrara's group described vascular endothelial growth

factor (VEGF), which was thought to be a major cytokine in the regulation of blood

vessel growth[84]. These molecules were later determined to be the same, proving that this

single protein (thereafter referred to as VEGF) was responsible for the disparate

functions of regulating vascular permeability and vascular expansion[85,86]. Judah Folkman

would also make invaluable contributions to the discovery of VEGF functionality,

establishing VEGF as a mitogenic factor and a primary promoter of angiogenesis[85,87,88].

Eventually, different isoforms of VEGF would be discovered, along with a number of

related growth factors. Years of investigation would substantially broaden the known

functions and targets of this family of growth factors, although a complete model of

their complex signaling pathways is still being established.

1.2.2.2 The VEGF Family

The VEGF family contains a number of isoforms and related proteins. The class

of proteins associated with most tumor cells is commonly referred to as VEGF, although

it is more precisely named VEGF-A. VEGF-A is known to have at least five splice

variants consisting of 121, 145, 165, 189, and 206 amino acid residues, of which the 121,

165, and 189 variants are most commonly expressed. These are encoded by an approximately 14,000 base-pair gene with eight exons, of which the sixth and seventh encode a heparin-binding domain[89,90]. VEGF-A121 lacks both heparin-binding domains and does not attach to the extracellular matrix or cell membrane[91,92]. Conversely, VEGF-A189 binds to heparin with a high affinity and is found sequestered predominantly in the extracellular matrix and, to a small extent, on cell surfaces[92,93]. Despite the fact that it becomes soluble with the cleaving of its carboxyl terminus, VEGF-A189 does not appear to be active in the signal transduction process to a significant degree[94]. VEGF-A165 has a moderate affinity toward heparin. This splice variant lacks the heparin-binding domain encoded in the sixth exon, but retains that of seventh[95,96]. About half of the 165-isoform growth factors that are produced will bind to the cell surface or extracellular matrix[93].

The heparin-binding ability of VEGF-A165 is significant in that by binding to the heparan-sulfates of the extracellular matrix, VEGF-A165 is also able to release other angiogenic factors stored there. One such factor, basic fibroblast growth factor (bFGF), induces a strong angiogenic response, as it operates synergistically with VEGF[97,98]. The heparin affinity of VEGF-A165 also assists in the amelioration of oxidative damage to the growth factor. Once oxidized, both VEGF-A165 and VEGF-A121 lose their ability to bind to the VEGF receptor VEGFR-2. VEGF-A165, however, is able to use heparan-sulfate proteoglycans as surrogate receptor-binding facilitators, compensating for this defect and significantly prolonging the bioactive lifetime of the growth factor[99,100].

The ubiquity and persistence of VEGF-A165 has led to a strong association of the isoform with angiogenesis. Historically, the diffusible heparin-binding protein that was revealed to be the archetypal angiogenic factor strongly corresponds to this particular isoform.

VEGF-B, has two isoforms, VEGF-B167 and VEGF-B186[101,102]. Both isoforms are most abundant in cardiac and skeletal muscles and bind to the VEGF receptors VEGFR-1 and neuropilin-1, but not to VEGFR-2[103-105]. VEGF-C and VEGF-D both bind to VEGFR-3, a receptor involved in lymphogenesis[106-111]. They also bind to VEGFR-2, but generally do not display strong mitogenic effects in endothelial cells, as compared with VEGF-A[107,110]. VEGF-E is a potent angiogenic factor[112]. It binds to VEGFR-2 and is very similar in structure to VEGF-A, but its production is facilitated by the orf virus and it is not part of the human proteome[113]. Although the B, C, D, and E families of VEGF serve important roles in angiogenesis and lymphogenesis, they are more specific than VEGF-A and play a lesser function in general tumor pathophysiology.

Various studies have shown a distinct spatial and temporal correlation between the expression of VEGF-A proteins and an increase in vascular permeability and endothelial cell mitosis[114-117]. VEGF-A is distinct among the native VEGF proteins and related growth factors in that its expression is highly affected by hypoxia[118-121]. An upstream hypoxia regulatory element that binds HIF-1 is a transcription enhancer, mobilizing VEGF-A as an adaptive response to oxygen starvation[122,123]. Here, VEGF-A

represents a critical component in the initiation of angiogenesis. It has been shown that VEGF-A is necessary for angiogenesis and vasculogenesis to occur, leading to a lethal embryonic vascular deficiency in animals with even a single nonfunctional VEGF-A allele[124,125]. It is generally agreed that VEGF-A represents a critical bottleneck in angiogenic signal transduction. But, although this linchpin factor plays an indispensable role in vascular adaptation, it is by no means the only significant player.

1.2.2.3 The VEGF Receptors

The various forms of VEGF bind to receptor tyrosine kinases (RTKs) (Figure 6)[126]. Of primary importance to angiogenesis are VEGFR-1 and VEGFR-2 (alternatively named flt-1 and flk-1/KDR, respectively). The cell-bound form of these receptors consists of seven immunoglobulin-like domains in the extracellular region, a transmembrane segment, and a split tyrosine kinase (TK) domain in the intracellular region[127,128]. The VEGFR-1 and VEGFR-2 binding domains occur at opposite ends of the VEGF monomer; two growth factor proteins will form disulfide bonds linking them in an antiparallel arrangement, such that the VEGFR-1 or VEGFR-2 binding domains of each monomer portion occur at opposite ends of the combined structure[129]. The bound monomers thus contain a binding domain for both receptor types at both ends of the structure.
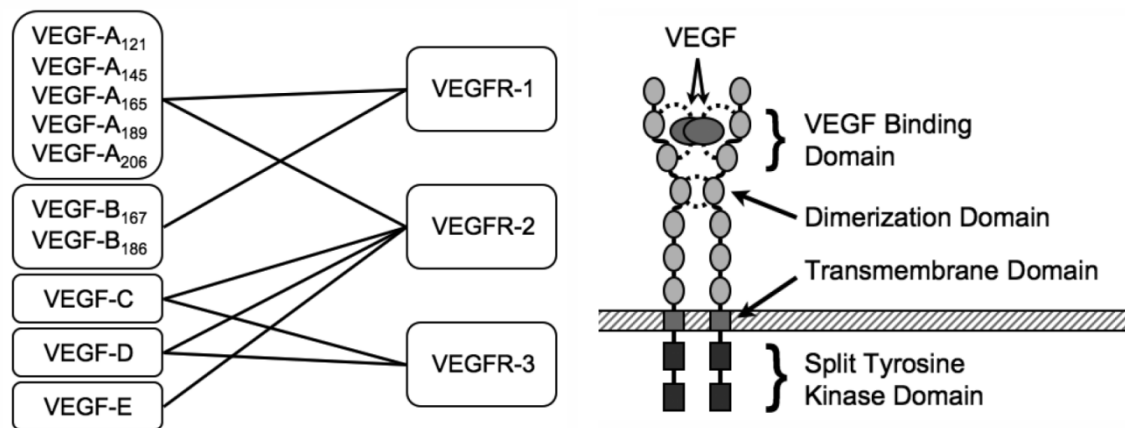
Figure 6: The Binding of VEGF to its Receptors: Different forms of VEGF will bind to certain receptors to stimulate various signaling pathways (left). VEGFR-1 and VEGFR-2 (the most relevant in terms of angiogenesis) consist of extracellular and intracellular domains with specific binding and signal transduction functions (right). (From ref. 126: permission from pub.)

The VEGF binding site occurs at the second and third immunoglobin-like domains for both VEGFR-1 and VEGFR-2[130]. Upon binding to the receptors, the VEGF ligand will cause the fourth immunoglobin-like domains of two adjacent receptors to bind to each other[131]. This domain is referred to as the *dimerization domain*. Dimerization will induce a chemical cascade in which tyrosine phosphorylation facilitates the phosphorylation of intracellular proteins, thus initiating signal transduction[132]. Once VEGF binds to its receptor, the complex is absorbed into the cell and digested.

VEGFR-2 is the primary receptor for the physiologic responses associated with VEGF[129,133]. It has been shown that endothelial cell mitogenesis and vascular permeability enhancement are suppressed in the lethal knockout of VEGFR-2. Mice

devoid of VEGFR-2 fail to undergo vasculogenesis and will die in utero at approximately 9 days post-fertilization due to inadequate blood supply to vital tissues[134]. This suggests that VEGFR-2 plays a primary role in angiogenesis, vessel maintenance, and endothelial cell survival.

Although the function of VEGFR-2 is well characterized, the function of VEGFR-1 is not. Mice lacking VEGFR-1 also die in utero, but in this case the lethality is due to the extreme proliferation of angioblasts[135,136]. Therefore, at least during the early developmental stage, VEGFR-1 seems to serve as a suppressor of VEGF vasculogenic signaling. In fact, it has been proposed that the primary function of VEGFR-1 is to serve as a decoy receptor for VEGF[137]. By sequestering growth factors, VEGFR-1 moderates VEGFR-2 binding and thus serves as an inhibitor to angiogenesis even though it displays no overt anti-angiogenic signaling properties[133,137]. This theory is supported by the observation that a mutated form of VEGFR-1 that binds VEGF but lacks the TK domain is observed to cause no apparent deviation from normal vascular development[138]. Other studies have shown that VEGFR-1 is able to facilitate monocyte chemotaxis and weak mitogenic signals, along with significant tissue-specific effects[139,140]. So, although it is widely accepted that VEGFR-2 plays the major role in angiogenic signaling transduction, the function of VEGFR-1 seems to be more subtle and arrayed.

A third receptor, VEGFR-3 (flt-4), has been identified, although this receptor is

primarily involved in lymphogenesis and plays little role in angiogenesis or

vasculogenesis[141]. Of the VEGF proteins, the VEGFR-3 receptor binds only VEGF-C and

VEGF-D[107,108,110]. A soluble splice variant of VEGFR-1 also exists. Since this receptor is not

bound to the cell membrane, it cannot initiate signaling transduction and serves

exclusively as a VEGF scavenger[142].

1.2.2.4 The Angiopoietins

The angiopoietins are protein growth factors that play a major role in

maintaining the functional stability of the vasculature. Four angiopoietins are known, of

which Ang-1 and Ang-2 are most thoroughly understood in terms of their contribution

to angiogenesis[143]. Both ligands bind to the TKR Tie-2 (**T**yrosine kinase receptors with

Immunoglobulin and **E**pidermal growth factor homology domains). The Tie-2 receptor

was first identified as an important component of the angiogenic process in 1997, when a

soluble truncated form of the receptor was shown to stifle tumor growth and inhibit

vascular proliferation[144,145]. The antitumor effect elicited by the soluble receptor was

shown to be primarily due to the limiting effect of vascular regression rather than any

cell lethality, as viability was not altered in cultured tumor cells. This work firmly

established the Tie-2 receptor and its ligands as important elements of angiogenic signal

transduction.

Ang-1 is involved in the angiogenic process of pericyte recruitment (which provides structural support to the vasculature and defines the transition from immature to mature vessels) and the stabilization of the vasculature, although its ability to induce endothelial cell mitosis is not clearly defined[146-148]. In fact, Ang-1 seems to play a complementary role to VEGF in the angiogenic process. Overexpression of VEGF produces a marked increase in vascular density by promoting the tortuous and branching expansion of immature vessels. On the other hand, Ang-1 overexpression causes an increase in vessel diameter[146]. Under normal conditions, the constitutive expression of Ang-1 is necessary for the development, stabilization, and maintenance of a functional vascular network[149].

The action of Ang-2 is more complex. Ang-2 knockouts have shown that the absence of Ang-2 does not affect vasculogenesis; the prenatal vasculature develops normally in these animals[150]. Ang-2 is normally upregulated at remodeling sites, and it is required for postnatal vascular reorganization[151]. Accordingly, Ang-2 knockdown animals are unable to initiate angiogenic remodeling.

Whereas Ang-1 expression promotes vessel stabilization, Ang-2 has been shown to cause a destabilizing effect. It is upregulated in areas undergoing vascular restructuring, and whereas the Ang-2 ligand does not induce receptor kinase phosphorylation, it effectively blocks Ang-1 signaling by binding to their common Tie-2 receptor[151]. This causes a degradation of the basement membrane and the detachment of

vessel pericytes from the lumen[152,153]. Hypoxia has been shown to increase the levels of both angiopoietins, although the induced amplification of Ang-2 is much greater than that of Ang-1[120,154,155]. Ang-2 is also observed in higher concentrations under increased VEGF expression, relative to Ang-1[120,154]. This suggests that the ratio of Ang-2 to Ang-1 is more important in predicting the dominant physiologic response than are absolute quantities[156]. Ang-2's effects contribute to either angiogenic or anti-angiogenic action depending on the context of its expression.

In the presence of VEGF signaling, the destabilization of mature vessels by Ang-2 is one of the first steps in the angiogenic process. The degradation of the basement membrane and the detachment of pericytes allow endothelial tubes to initiate budding and intussusception (the bifurcation and separation of a single vessel), hallmark features of angiogenesis and the primary features of proliferation[157]. In the absence of VEGF signaling, the devolution of the vasculature initiated by Ang-2 will lead to vascular regression and an eventual depletion of the network—an anti-angiogenic response[151] (Figure 7). The complex functionality of Ang-2 is emphasized in a recent paper that showed that when Ang-2 was systemically overexpressed, vascular regression was observed even in the absence of VEGF inhibition[153].
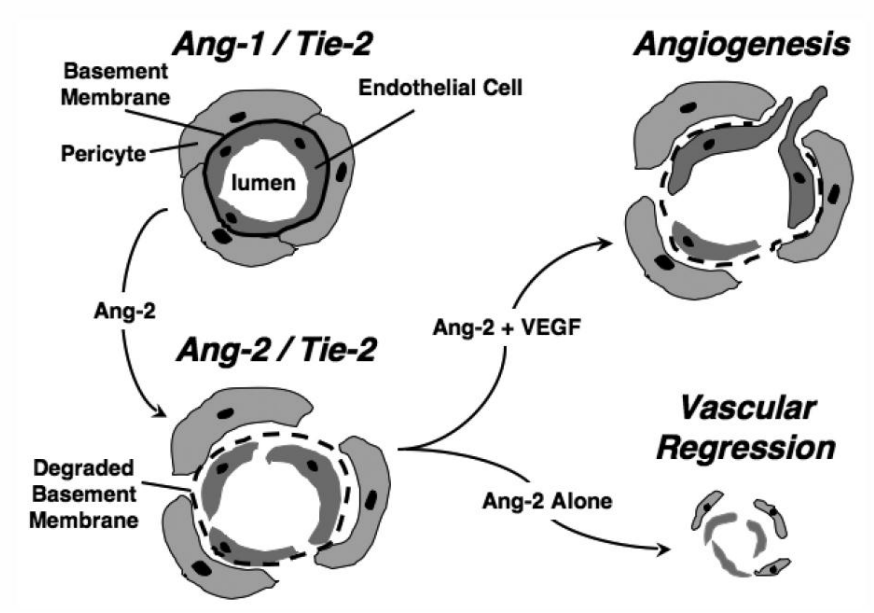
Figure 7: The Physiological Effects of the Angiopoietins: Ang-1 maintains vessel stability, whereas Ang-2 destabilized the vasculature. In the presence of VEGF, Ang-2 contributes to angiogenesis. In its absence, Ang-2 leads to vascular regression. (Figure courtesy of C. Kontos)

Ang-2 overexpression also caused a transient exacerbation of hypoxia, with a return to an intertumoral oxygenation similar to the untreated control group with continued overexpression. Angiogenesis and tumor growth was inhibited, while the apoptotic response was enhanced. Interestingly, despite vascular regression and transient hypoxia, tumors showed an increased perfusion in the surviving vessels. After vascular regression, the remaining vessels became dilated due to the loss of pericytes. The overexpression of Ang-2 was shown to cause an inability of pericytes to remain attached to endothelial cells, although it did not directly lead to pericyte death.

Ang-2 overexpression, with or without VEGF inhibition, inhibits angiogenesis and promotes apoptosis; it has no apparent long-term effect upon hypoxia. Neither does it have an effect on cell proliferation, leading to the conclusion that the suppression of tumor growth caused by Ang-2 is attributed to enhanced tumor cell apoptosis[153]. This suggests that the role Ang-2 plays as an adjunct to VEGF is dependent on a certain balance between the two ligands.

1.2.4 Models of Angiogenesis in Tumors

The VEGF variants, the angiopoietins, and their receptors— although among the most important components of an angiogenic response—are only a selection of the myriad of proteins capable of influencing vascular growth or regression. Yet, despite the sheer number of such factors, the vasculature of healthy tissue is maintained in a state of optimal balance through their precise regulation[158]. Proangiogenic factors are upregulated in response to stimuli such as hypoxia[159]. They initiate vascular expansion to the point at which the hypoxic condition is rectified or the cells undergo apoptosis[158]. This healthy angiogenic response is uncommon during adult life and is typically limited to wound healing, physiologic organ growth, and female reproductive processes[160,161]. In fact, the stability of adult vasculature is highlighted by the longevity of endothelial cells, which normally exhibit periods of turnover on the order of years[162].

The model of a balance between pro- and anti-angiogenic factors readily lends itself to the concept of an "angiogenic switch." The angiogenic switch is the point at

which the balanced regulation of angiogenic factors fails[158]. For example, in healthy tissues, angiogenesis is initiated to assist in the process of reforming tissue that has been damaged by physical trauma. As the tissue repairs itself, angiogenic factors are downregulated again, and the vasculature returns to a static state. However, cancerous cells continue to proliferate and induce vessel expansion, thereby preventing a state of vascular stasis—the tumor becomes much like a "wound that never heals"[163]. Although this model adequately explains the process of angiogenesis in well-established tumors, an accurate model of vascular adaptation in nascent tumors has only lately emerged.

1.2.4.1 Evidence for Hypoxia-Independent Angiogenesis

The role of angiogenesis in incipient tumor growth is an important aspect of the tumorigenic process, although until recently, discovery in this area was obstructed by the technical difficulties of observing nascent tumor growth. In work done by our group, a small number of cancer cells engineered to express green fluorescent protein (GFP) were injected into a murine window chamber. The constitutive expression of GFP allowed the cells to be observed and tracked even while the burgeoning cancer was a collection of only a few cells. At the earliest stages of growth, the cells would preferentially divide in the direction of microvessels[164]. The cells would take on a fibroblast-like form (a typical morphology associated with epithelial-to-mesenchymal transition) as they elongated and divided unidirectionally toward their nutrient supply

36

(Figure 8). This chemotaxis-like feature is possibly due to oxygen, nutrient, growth

factor, or other cytokine gradients emanating from the vasculature.
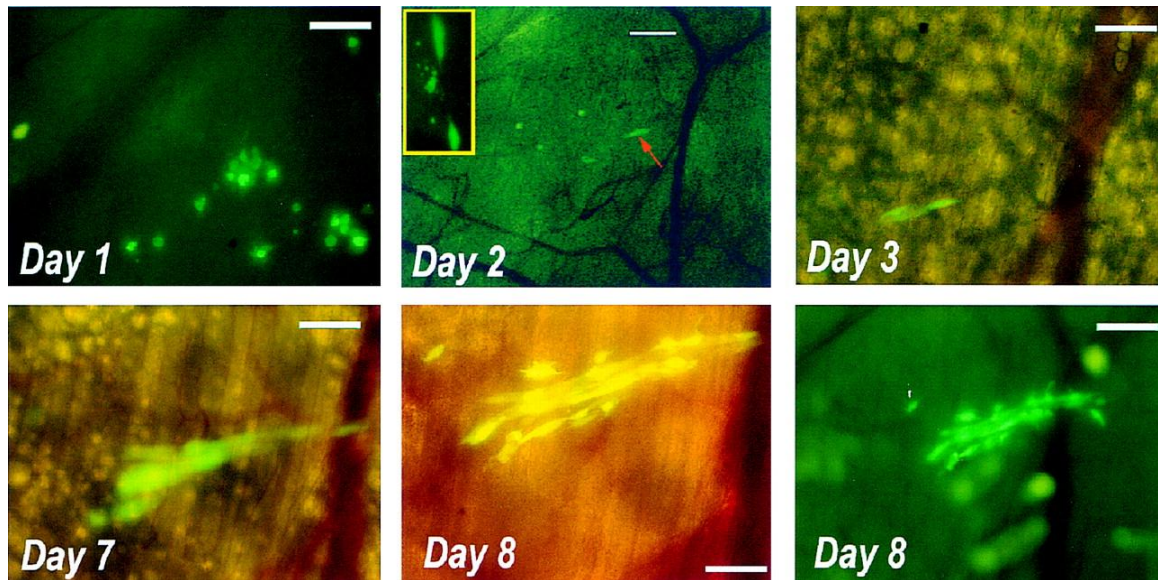
Figure 8: Tumor Cell Migration During Early Tumor Development: Approximately 20 tumor cells expressing a fluorescent protein were injected into a murine dorsal skin-fold window chamber on Day 1. Over the course of 8 days, some cells were observed to elongate and directionally divide towards the nearest vessel (Day 2: red arrow). The cells that failed to elongate underwent apoptosis (Day 2: inset). Days 3, 7 and 8 show a magnified image of the elongated cell noted on Day 2. The preferential proliferation of the daughter cells towards the vessel is apparent. (From ref. 164: permission from pub.)

These observations may lend support to the model of vascular cooption that has

been observed in a number of tumor types. Cooption was reported by Yancopoulos and

Wiegand in brain tumor models[165] and by Pezzella and colleagues in primary and

metastatic lung cancers[166]. Rather than initiate new vessel growth, tumor cells will

sustain themselves on oxygen and nutrients supplied by the existing vasculature for a

period of time. The cancer will incorporate itself into the preexisting architecture of the primary or metastatic site before any expansive vascular remodeling occurs.

Yancopoulos reports that this relationship is short-lived, however, as Ang-2 expression is induced in the endothelium of coopted vessels not long after tumor association, causing pericyte dissociation[165]. It has been proposed that this response is part of an antitumor defense mechanism. In the absence of concurrent VEGF expression, this induces vascular regression and a hypoxic crisis that kills off most of the newly formed tumor. What's left of the viable mass initiates a survival reaction, upregulating VEGF expression. This facilitates the angiogenic response classically associated with tumor growth and saves the tumor. Although this is an interesting model for tumor angiogenesis initiation, Yancopoulus' group did not directly prove that a hypoxic crisis was necessary.

Recent work from our laboratory challenges the idea that hypoxia is responsible for the angiogenic switch. Two different tumor lines genetically engineered to express red fluorescent protein (RFP) and GFP as a reporter of HIF-1 activation were grown in skin-fold window chambers in mice. In both tumor models, angiogenesis preceded the first positive detection of hypoxia (through optical identification of green fluorescent cells) by a few days[67].

To further prove that angiogenesis initiation was independent of hypoxia, the animals were treated with tirapazamine (a drug that selectively kills hypoxic cells). It

was hypothesized that this treatment would delay the onset of angiogenesis if hypoxia were required for angiogenesis initiation. The results did not validate this hypothesis: tirapazamine delayed the detection of hypoxic, HIF-1+ cells, but had no effect on the initiation of angiogenesis[67]. These results do not support Yancopoulus' theory. Both cell lines were shown to express low levels of VEGF under aerobic conditions, which likely explains the independence of angiogenesis initiation from hypoxia.

Our group also examined the role of VEGF in the early phases of tumor angiogenesis by adding soluble VEGF receptor protein (which binds VEGF, but does not initiate signal transduction) to window chambers at the time of tumor cell transplant. When the soluble receptor was added, tumor growth was suppressed before any signs of angiogenesis were manifest[164]. Conversely, the control group displayed vascular tortuosity and budding at even a few hundred cells, and newly formed vasculature filled the tumor by 20 days post-injection. This indicates that angiogenesis or angiogenic signaling plays a critical role in tumor survival and progression long before the tumor reaches a critical vascular perfusion limit and the onset of hypoxia.

The study also reported that the chemotactic signaling of endothelial cells induced an epithelial–mesenchymal transformation of tumor cells. After the tumor cells migrated to the vasculature, they did not grow randomly, but aligned themselves longitudinally along the direction of the nearby vessels, further indicating the presence of a signaling agent secreted by the endothelium. The ability of the earliest tumor cells to

39

communicate with the vasculature through mutual signaling is likely a crucial aspect of tumorigenesis, as tumors cells that failed to show the epithelial–mesenchymal transition died after a few days. Folkman has expressed strong support for this model of cosignaling; he has further suggested that the angiogenic signals released by the cancer cells not only prepare the endothelium for remodeling, but also elicit the release of chemo-attractants that guide the burgeoning tumor to the vasculature[167].

A paper by Raleigh and colleagues further draws into questions the assumption that hypoxia is a prerequisite for VEGF induction. In their study, an agent that binds preferentially to hypoxic tissues was employed. After performing immuno-histochemistry to detect this agent in a number of human tumor types, they were able to find no spatial correlation between hypoxia and VEGF abundance[168].

These studies establish an interesting model for VEGF functionality beyond the scope of angiogenesis. They suggest a new model of tumorigenesis that challenges the longstanding paradigm in which tumors grow as an avascular mass to a state of vascular deficiency and chronic hypoxia (1–2 mm diameter) before angiogenesis is induced. They force a reevaluation of the classical relationship between hypoxia and angiogenesis. A relationship that was once generally causal in nature has been shown to be much more complex and interdependent than previously believed.

1.2.4.2 The Rational for Anti-Angiogenic Approaches in Cancer Therapy

The untreated tumor vasculature is malformed and inefficient. Its physical structure is in a constant state of flux. The imbalance between pro- and anti-angiogenic factors leads to excessive endothelial cell proliferation and pericyte detachment[158]. Vessels become tortuous and hyper-permeable, leading to longitudinal variations in nutrient concentrations[76]. Tumors are also prone to pathologically high interstitial pressure, due to microvessel hyper-permeability, the lack of a functional lymphatic system, and the solid stress of confined growth[169,170]. This solid stress increases interstitial and intravascular pressure, inhibiting the ability of the vasculature to maintain a cross-sectional gradient sufficient for adequate perfusion.

Vascular remodeling and constant angiogenic signaling in tumors ultimately lead to spatial and temporal heterogeneity in oxygenation[76]. Despite this severe environment, many tumor cells manage to subsist on what oxygen they receive and increasingly incorporate more plentiful substrates into their metabolic cycle[171]. The hypoxic environment promotes a number of pathologic adaptations, including anti-apoptosis[18,44], metastasis[172,173], and further angiogenic signaling. To yield the tumor environment less conducive to aggressive growth, many cancer treatments thus focus on breaking the vicious cycle of angiogenesis.

Anti-angiogenesis was first considered as a treatment option based upon the hope that it would destroy tumor vasculature to the point at which the tumor regressed under severe oxygen starvation[174]. Treatments that employed anti-angiogenic agents

alone showed some benefits; however, significant gains in overall survival were not realized[175,176]. At high dosages, anti-angiogenic agents begin to adversely affect healthy vasculature, as evidenced by the increased risk of arterial thromboembolisms and congestive heart failure associated with the anti-angiogenic drug bevacizumab[177]. Therefore, clinical doses are more moderate and probably incapable of causing total vascular regression. It is important to note, however, that because of the abnormality and instability of the tumor vasculature, tumor vessels are usually more sensitive to anti-angiogenic therapies than are normal vessels. The optimization of clinical doses is therefore a highly faceted problem requiring extensive clinical assessment.

As opposed to lone administration, evidence suggests that when anti-angiogenic agents are combined with cytotoxic treatment, the antitumor effect is heightened[178]. Such responses were predicted by Beverly Teicher, who proposed that, by using combinational treatments, disparate aspects of tumor pathophysiology could be targeted; cytotoxic treatments would destroy the tumor cells directly, while anti-angiogenic agents would destroy the vasculature that provides nutritional support to the growing tumor.

However, if anti-angiogenic treatment caused vascular regression through an indiscriminate destruction of vessels, one would expect that this would lead to increased hypoxia and cell starvation. Destroying the vasculature would destroy the delivery route of the tumor's oxygen and nutrients. Concurrent anti-angiogenesis would

42

therefore be expected to decrease the efficacy of cytotoxic therapy. The synergistic effect of combined therapy observed in preclinical studies is thus at odds with the established anti-angiogenic model.

1.2.4.3 Vascular Normalization

Rakesh Jain would later suggest an explanation for this in terms of a new model of anti-angiogenic activity that emphasizes a process of vascular "normalization." Although the precise mechanism of this process is not well understood, his theory involves the ordered pruning and reorganization of vessels, such that the vasculature develops a structure more similar to normal tissue, increasing its oxygen and drug transport capacity[179].

It is likely that potent and continued anti-angiogenic induction will result in a severe depletion of the vasculature and inadequate supply. However, Jain suggests that with proper dosage and scheduling of anti-angiogenic agents, there may develop a critical window en route to vascular regression in which vessels become "normalized". During this transient time frame, the vasculature takes on a structure more similar to that found in normal tissues than the tortuous and inefficient architecture that is characteristic of tumors. As the inhibition of angiogenic factors induces vascular regression, immature vessels are preferentially pruned[180]. These immature vessels contribute most predominantly to the inefficiencies of an excessive architecture. The degree of vascular pericyte coverage (which defines vessel maturity) is a major factor in

determining the fate of vessels exposed to anti-angiogenic factors[153,181]. Thus, blocking angiogenic factors would have a different effect on the pruning of microvessels, depending on the degree of maturation.

A further proposed mechanism of action involves the inhibition of nitric oxide production by anti-VEGF agents. VEGF has been shown to interact with nitric oxide in a reciprocal pattern of regulation[182]. The regulation of nitric oxide by VEGF is mediated through VEGF's upregulation eNOS (endothelial nitric oxide synthase)[183]. Inhibition of VEGF would elicit a concurrent reduction of nitric oxide through the blocking of this signaling pathway. Since nitric oxide is a vasodilator, it is possible that anti-VEGF therapies my help to normalize flow patterns by causing the constriction of dilated shunting vessels. In the absence of VEGF-mediated nitric oxide production, these vessels shrink in diameter. Since excessively large vessels dominate flow through the tumor because due to their low flow resistance, smaller vessels are prone to weak or static blood flow. With the inhibition of VEGF, vascular diameter becomes more uniform, and blood flows more evenly throughout the vascular network[184] (Figure 9).
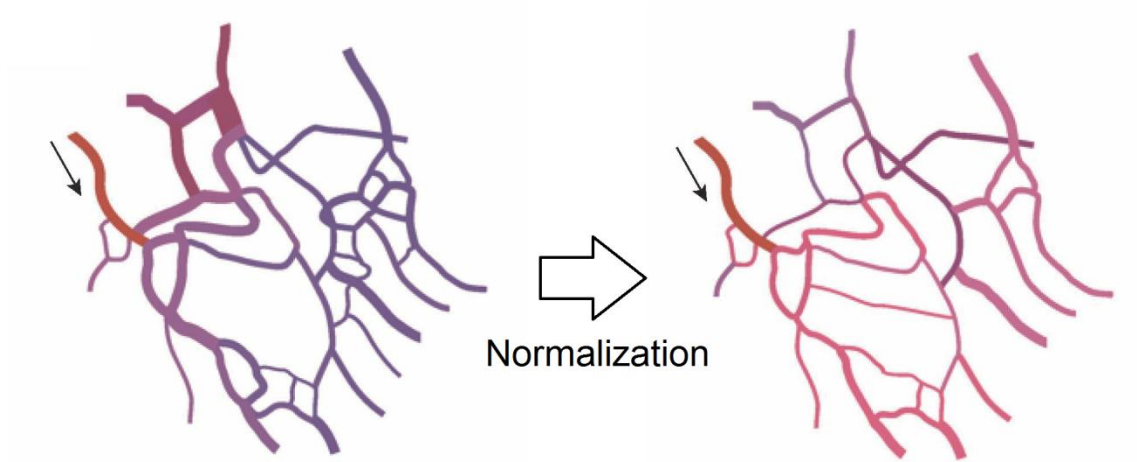
Figure 9: Normalization of Blood Flow: Inhibition of nitric oxide production causes dilated vessels to constrict, producing more uniform vessel diameters and normalized blood flow. Oxygen delivery in a normalized vascular network is more efficient. (From ref. 184: permission from pub.)

With the temporary transition to a somewhat normalized structure through these combined effects, oxygenation is improved[179]. Blockade of VEGF signaling reduces vascular permeability and interstitial fluid pressure, allowing nutrients to perfuse more freely. Although hypoxia is reduced and nutrient delivery is improved during the normalization window, a number of clinical and preclinical trials have shown that this does not have an accelerating effect on tumor growth.

The effect of anti-angiogenesis on perfusion was observed in a rectal carcinoma trial in which patients underwent combined anti-angiogenic, radiation, and chemotherapy treatments prior to surgery. At 12 days after the first anti-angiogenic (bevacizumab) treatment, functional computed tomography showed significant

decreases in tumor blood perfusion and blood volume[185]. Interstitial fluid pressure and vascular density were also reduced. However, despite vascular regression, these tumors showed no decrease in the uptake of fluorodeoxyglucose, a radioactive glucose analog, as measured by positron emission tomography. Despite vascular regression, the tumors showed no signs of impaired transport, suggesting a normalization effect was induced. At the lower of two investigated bevacizumab doses, all six patients showed a marked response to therapy, through the analysis of the surgical specimen. Furthermore, at the higher dose, combinational treatment induced two complete pathologic responses out of five patients.

In a later study, Batchelor and Jain presented evidence for normalization in human glioblastoma patients[186]. These patients, who all failed under conventional treatment, underwent anti-angiogenic monotherapy. Using an array of magnetic resonance imaging techniques, it was shown that the treatment achieved a reduction in edema, which is consistent with a reduction in hyper-permeability. A simultaneous drop in vessel diameter suggested an improvement in pericyte coverage. These normalization responses accompanied a decrease in the rate of tumor growth.

1.2.5 Angiogenesis within the Context of Radiation Therapy

The vascular component of radiation damage, long poorly understood, is presently emerging as a critical component of radiotherapy models. This is chiefly due to a better understanding of the role blood vessels play in modulating tumor

proliferation, the mechanisms of endothelial cell destruction, and the modes of vessel repopulation after radiation exposure.

The tumor vasculature plays a number of roles necessary for maintaining tumor survival and proliferation. Most obviously, nutrient and oxygen transport are facilitated by blood vessels. We have already discusses how alterations in these delivery patterns may have a profound impact on tumor phenotype. Furthermore, the vasculature plays an important role in facilitating immune response by providing a route of leukocyte infiltration into the tumor, which, in terms of tumor control, may be beneficial (when immune cells target the tumor for destruction) or detrimental (when immune cells initiate tumor-promoting inflammation).

Thus, alterations in vascular function would be expected to have important implications for tumor response to radiation therapy. The details of vascular degradation and recovery after irradiation are intimately tied to tumor regression and repopulation. Cellular interactions between tumor and endothelial cells enable a coordinate response which enables tumor survival. Therefore, angiogenesis and angiogenic factors play a pivotal role in facilitating recovery from radiation insult, and their effects may at least partially determine the likelihood of local tumor control.

47

1.3 Radiation Therapy

1.3.1 Basic Radiobiology

The biological effect of ionizing radiation was first observed by Antoine-Henri Becquerel, who developed acute skin erythema and ulceration after accidental radium exposure[187]. Within a year, x-rays were being explored as a treatment for cancer. However, it wasn't until the genetic basis of the cellular lifecycle was established that biological mechanisms of radiation damage were truly understood.

Ionizing radiation achieves its cellular toxicity through the generation of DNA lesions. These occur when the chemical structure of the DNA strand at a particular point is altered by direct or indirect ionization events. Many simple lesions can be corrected through innate repair mechanisms. In fact, of the over 100,000 lesions experienced daily by the average mammalian cell (due to a variety of factors), the vast majority will be effectively repaired with no biological consequence[187]. As radiation exposure increases, however, the probability of a double strand break rises. These types of lesions are much more prone to permanent alterations in the DNA due to less effective repair mechanisms. In some cases, these alterations will induce an apoptotic response. However, in most cancers, resistance to apoptosis arises as part of their initial stages of oncogenic transformation. In this case, radiation-induced lesions will tend to accumulate until the cell attempts to undergo mitosis. Structural abnormalities will result in improper chromosomal segregation at this point, resulting in a state of limited

mitotic potential, known as "reproductive death"; the cell (or daughter cells within a limited number of generations) will be unable to divide due to gross chromosomal aberrations[188]. This may lead to senescence or cell death. This is mechanism of tumor cell death forms the underlying basis of radiation therapy.

1.3.2 Modern Radiation Delivery Techniques and Future Directions

Recent advances in medical physics have enabled the emergence of radiation technologies capable of delivering precise conformal doses with high degree of spatial definition. These techniques are motivated by the clinical goal of delivering maximal dose to the tumor, while sparing nearby organs at risk. Intensity modulated radiation therapy (IMRT), one such technique commonly used in the clinic, has enabled great advances in the treatment of various cancer types due to its ability to generate arbitrary radiation fields with steep dose gradients. The fields are calculated from three-dimensional patient data generated from MRI or CT. Radiation dose patterns are computationally simulated to determine the ideal setup for delivering maximum dose to the tumor with minimal normal tissue irradiation. This enables better tumor control while minimizing normal tissue effects, especially in cases where flat-field doses would present unacceptable risks of complications due to the proximity of highly sensitive organs.

Furthermore, a number of new technologies have been developed which allow for the spatial fractionation of doses wherein radiation intensity is spatially modulated

to deliver a non-homogenous dose distribution. GRID and microbeam radiotherapy are two such techniques. In both of the schemes, relatively high doses are delivered to a fractional volume of the tumor, while areas outside the high-dose regions receive minimal irradiation. Microbeam therapy typically delivers doses of hundreds of Gray in repeated, sub-millimeter line patterns separated by wider regions that receive very little dose (Figure 10)[189]. As this technique is in pre-clinical development, these doses and geometries vary greatly between studies, and ideal treatment schemes are currently unknown. GRID therapy delivers 10-20Gy in daily doses along hundreds of narrow, cylindrical entry beams[190]. Microbeam therapy still has a number of technical obstacles to its incorporation in the clinic. Primarily, maintaining spatial fractionation patterns at depth is a problem, as lower energy particles will scatter within tissue, resulting in beam broadening. The generation of particles with energies high enough to alleviate this effect currently requires accelerators impractical for clinical use. GRID therapy, on the other hand, is presently emerging as a treatment option for very large tumors volumes (primarily palliative), with encouraging results[191-193].
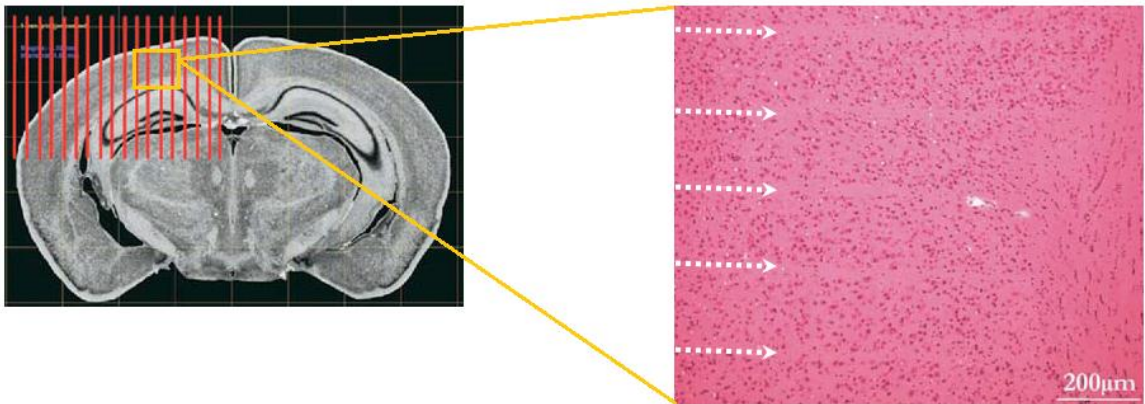
Figure 10: Microbeam Irradiation of a Normal Mouse Brain: Due to the postulated vascular recovery from small irradiation volumes, microbeam therapy has been shown to be well tolerated in normal tissues. Here a portion of a normal mouse brain was irradiated in a series of 18 parallel micro-planar beams (left). The beams were 25μm in width and spaced 211μm apart. The beam dose was 1000Gy. Irradiated mice showed no apparent physical or cognitive defects in three-month post-irradiation observation. Histological analysis of the irradiated tissue showed remnants of radiation injury, however (arrows, right). (From ref. 189: permission from pub.)

Both of these techniques have reported specific tumor cell kill with relatively minimal normal tissue effects. One of the theories explaining this normal tissue resistance involves a greater capacity for morphologically and functionally normal vasculature to recover from spatially fractionated treatment, relative to the dysregulated, angiogenic vasculature associated with tumors. However, lacking a means of serial observation of vascular depletion and recovery, this theory has not been rigorously tested.

1.3.3 Vascular Radiation Response

Until recently, the prevailing model of radiation lethality in tumors involved the direct targeting of clonogenic cell populations. This model was based off of a wealth of *in vivo* and *in vitro* data: Radiation generates DNA lesions either through a direct interaction, or (more commonly in an oxygenated environment) through the generation of highly reactive oxygen radicals. If normal DNA repair mechanisms are unable to correct this damage, an apoptotic response may be initiated, or (much more commonly in cancers) mitotic cell death will occur.

Although this mitotic cell death after radiation therapy has been well established, its relative contribution to tumor-wide radiation response was questioned in a high-profile publication by Fuks and Kolesnick in 2003[194]. This paper followed from an earlier study which proposed that gastrointestinal damage following whole body irradiation was primarily facilitated through radiation-induced endothelial cell apoptosis, with secondary depletion of the epithelial stem cells that replenish the constantly sloughed off outer layer of intestinal villi[195]. This idea of microvascular depletion as the primary cause of systemic disease was controversial[196], considering the known radio-sensitivity of the rapidly dividing epithelial stem cells[197]. No less controversial, however, was the follow-up paper, which extended the hypothesis of "vessel-mediated radiation response" to tumor models. In this report, regulation of endothelial cell apoptosis is presented as the major inherent limiter of tumor growth. Mice rendered deficient in their

ability to initiate endothelial cell apoptosis by elimination of the acid sphingomyelinase

(asmase) gene were shown to harbor tumors that grew at up to a four-fold increased rate

compared to their wild type counterparts. Tumors grown in these mice were also

significantly radio-resistant, with 15Gy treated tumors continuing to grow at rates which

exceeded those of even non-irradiated tumors grown in wild type mice.

The major concerns that arose after the presentation of this report were not

primarily addressed towards the idea of vascular-regulation of tumor mass (which had

already been eloquently advocated by Folkman and largely accepted as the basis for

understanding oxygen-limited proliferation potential[198]). Neither was the idea of

endothelial cells undergoing radiation-induced apoptosis largely contested, as this too

had previously been shown to be initiated through the activation of asmase[199], which is

found in high concentrations in endothelial cells[200] and is known to initiate production of

the pro-apoptotic ceramide molecule[201,202]. Rather, criticism largely consisted of objection

to the potentially paradigm-shifting role of endothelial cell apoptosis (rather than

induction of mitotic catastrophe in the clonogenic tumor cell population) as the *primary*

mechanism of radiation induced lethality. Commentary generally highlighted

abnormally high radio-sensitivities of tumors grown in the wild type littermates of

asmase knockout mice, suggesting unique host-tumor interactions in this particular

model system[203,204]. Despite resistance to the proposed redefinition of the primary

mechanism of radiation response, the paper succeeded in presenting a provocative

hypothesis and elicited calls for "further work with other systems… to determine the contribution of endothelial cell response"[204].

Soon after Fuks and Kolesnick presented their argument for vascular radiation sensitivity, new light was shed upon radiation-induced mechanisms that seemed to present a biological resistance to endothelial cell destruction[49]. HIF-1, a hypoxia-associated transcription factor normally degraded in the presence of oxygen, was shown to be stabilized after radiation, despite radiation's known short-term reoxygenation effect. In fact, HIF-1 expression increased significantly from baseline levels up to 72 hours post-treatment, and this increased expression coincided both spatially and temporally with reoxygenation of previously hypoxic regions, evidently correlating these two phenomena. A combination of radiation-induced reactive oxygen species production, stress granule formation, and nitric oxide-mediated stabilization after macrophage infiltration were implicated in this effect[53].

The end result of radiation-induced HIF-1 expression is complicated. In p53-competent tumor cells incubated under hypoxia, HIF-1 was shown to potentiate apoptosis after radiation, compared to cells where HIF-1 expression was inhibited. However, *in vivo* studies showed that when HIF-1 was inhibited after radiation, tumor regrowth was significantly delayed due to vascular depletion. HIF-1 imparted a protective effect upon irradiated endothelial cells grown in vitro, possibly due to the induction of downstream vascular-targeting proteins, such as VEGF and bFGF[205]. Thus,

evidence suggests that in tumors that are p53-deficient (greater than 50% of human tumors[8]), or otherwise impaired in their ability to initiate apoptosis, HIF-1 may have the primary effect of diminishing the efficacy of radiation treatment.

The vascular radio-protective effect of HIF-1 induction presents an interesting problem in terms of the hypothesis that endothelial cell apoptosis is the primary mechanism controlling tumor response to therapy. Since the endothelial apoptotic response was shown to peak only a few hours after treatment[195,205], this theory cannot easily explain the protective effect of HIF-1, which is upregulated well after the period of maximal apoptotic response. Furthermore, earlier studies had shown that tumor-wide vascular destruction typically does not begin until 48 hours post irradiation[206]. Thus, another mode of endothelial cell death with more profound consequences for global vascular integrity may follow the initial radiation response. Geng's study also highlights another important aspect of vascular radiation-sensitivity: they observed that vascular depletion occurred at different doses depending upon which tumor line was grown in the host mouse. If vascular radiation response were strictly determined by the innate sensitivity of the host endothelium, one would expect to observe identical dose response characteristics (since the host endothelial cells are genetically normal). Clearly tumor signaling aspects play a significant role in modulating the host vasculature's response to radiation damage.

Regardless of the exact mechanism of action, mounting evidence indicates that classical models of radiation-induced tumor lethality fail to adequately incorporate the significant effect of vascular disruption in determining treatment outcome. Resultant changes in oxygen transport capacity will likely have a profound influence on tumor progression, as hypoxic induction has been clearly linked with tumor proliferation, survival, invasiveness, and metastasis, primarily effected through the HIF-1 signaling pathway[17]. The interplay among HIF-1 and vascular radiosensitivity is a complex dynamic that cannot be thoroughly understood without a method to serially observe these parameters *in vivo*. Thus the stage is set for a thorough analysis of vascular radiation sensitivity and its implications in post treatment oxygenation fluctuations, HIF-1 induction, and tumor invasion—**this is the major objective to the research presented here, which will be achieved through the development and implementation of optical methods.**

1.4 Optical Methods of Biological Investigation

1.4.1 The Dorsal Skin-Fold Window Chamber Model

The dorsal window chamber (Figure 11) is one of the staples of pre-clinical *in vivo* studies and provides invaluable insight into the fundamental aspects of cancer biology. It is uniquely capable of offering high-resolution images of living tumors and associated vasculature at optical wavelengths. Furthermore, it facilitates serial

measurements of the unperturbed tumor microenvironment, allowing for the observation of temporally evolving aspects of tumor growth and treatment response.
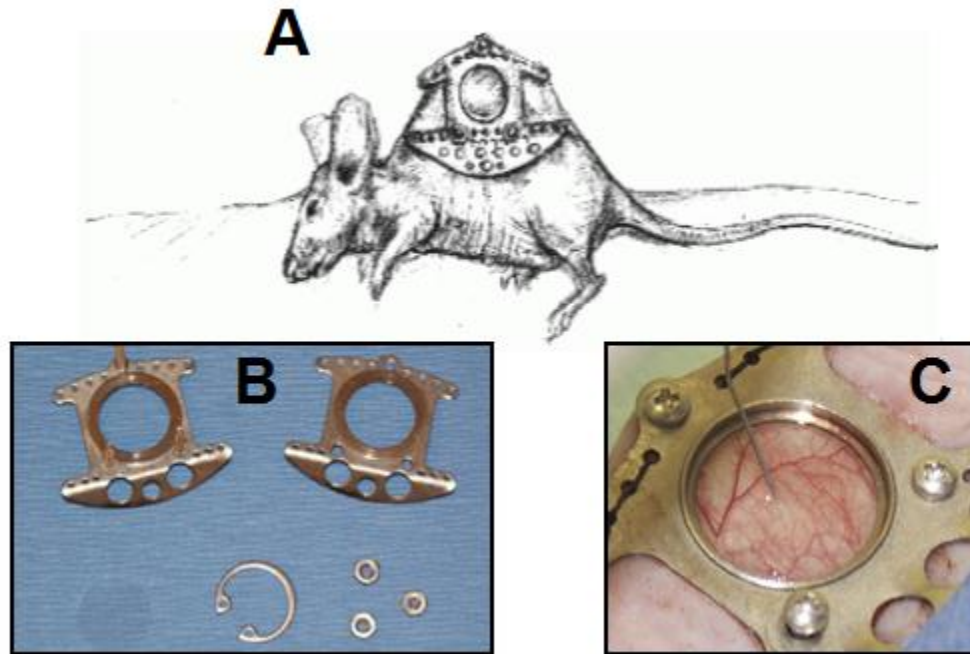
Figure 11: The Dorsal Skin-Fold Window Chamber: In a sterile surgical procedure, the window chamber is attached to the dorsal skin-fold of a mouse (A). The window chamber consists of a custom build titanium frame, nuts, a glass coverslip, and a retaining ring (B). During the surgical procedure, tumor cells may be inoculated into the exposed tissue to allow for serial optical interrogation of the growing tumor and surrounding tissue (C). (From ref. 207: permission from pub.)

These characteristics render the dorsal window chamber ideal for the study of radiation-induced effects upon the tumor and surrounding microenvironment. In particular, vascular depletion/angiogenesis and the regulation of fluorescent protein reporters can be tracked over an extended time course to elucidate post-treatment response. This is particularly important for a thorough understanding of micro-

physiological radiation effects, as no other *in vivo* model effectively facilitates the

tracking of temporal changes at the level of single microvessels. These vessels in

particular play a dominant role in regulating tumor oxygen delivery, and their structural

and functional alterations indirectly contribute to hypoxia-induced changes in tumor

phenotype. Tumor-associated microvessels are also sensitive to radiation damage,

leading to vascular disruption and resultant alterations in tumor oxygen supply after

therapy. Since tumor hypoxia is associated with a poor clinical outcome, the

observation of microvascular perturbation may provide critically important insight into

the relationship between post-treatment oxygen delivery and associated tumor

response.

A thorough explanation of the dorsal window chamber surgical procedure is

provided in the Appendix[207]. Briefly, nude mice are anesthetized using a

ketamine/xylazine preparation and the surgical area is disinfected using exidine and

ethanol. In each mouse, a circular incision 12mm in diameter is made in the loose skin

of the dorsal surface. The skin and underlying connective tissue are removed

completely. The dorsal skin is pinched up to form a skin fold which exposes the dermal

tissue on the opposite side of the area of excised skin. The incision is aligned with a hole

cut into a specially constructed titanium frame, which is then sutured onto the animal to

form a stable window into the underlying tissue.

Approximately 2×10^4 cells (variable, depending on tumorigenicity of the cell line) suspended in 20μL of serum-free media are injected beneath the exposed fascial plane. A sterile glass coverslip is then inserted into the titanium frame to form an air-tight, optically-accessible window into the inoculated tumor and surrounding tissue.

After the completion of the surgical procedure, antibiotic ointment is applied to any exposed wounds, and the animal is allowed to recover on an isothermal water circulation pad before returning it to its cage. After all surgeries are complete, the animals are returned to their housing facility and monitored daily for signs of surgical complication. After one week, most implanted cells will have grown to form viable tumors 1-2mm in diameter.

1.4.2 The 4T1-GFP-RFP Reporter Cell Line

A modified 4T1 murine mammary carcinoma cell line was previously developed by our lab; this cell line is commonly used in conjunction with the window chamber model[49]. The line was stably transfected with a retroviral gene vector encoding a green fluorescent protein (GFP) reporter, and expression of GFP in the cell is driven by a HIF-1-modulated hypoxia responsive element. Thus HIF-1 expression within a tumor grown from this line can be indirectly visualized and quantified through the intensity of the GFP signal. This line was also stably transfected with a red fluorescent protein (RFP) gene under a CMV promoter. Expression of RFP is constitutive and is used to visualize the spatial location and extent of the tumor.

1.4.3 Hyperspectral Imaging

Hyperspectral imaging is acquisition of images of the same field, but at a number of separate, discrete wavelength bands. Whereas standard color imaging techniques typically employ filters to separately acquire red, green, and blue channels, hyperspectral images may be acquired at many more color bands. Techniques employed here, for example, typically acquire images at 10nm wavelength bands over a range of approximately 100nm. Thus, a dozen or so spectral channels are collected.

The hyperspectral system created by our lab for use in biological studies consists of a standard scientific microscope, on which a liquid-crystal tunable filter is mounted to the microscope's optical port forward of a high-speed CCD camera. The tunable filter is software controlled to pass light within a selected 10nm wavelength bandwidth.

This system was designed and implemented by Brian Sorg to measure hemoglobin oxygen-saturation within the dorsal window chamber[208]. (A detailed mathematical model of this technique is provided in 2.1.1.) Since deoxy-hemoglobin's absorption spectrum changes dramatically over the 500-600nm range as it binds oxygen (Figure 12), these distinct spectra can be used to reconstruct oxy/deoxy-hemoglobin ratios in images of window chamber tumor/tissue. The percent of the total hemoglobin that is oxygen bound is the "hemoglobin saturation" at that particular location.
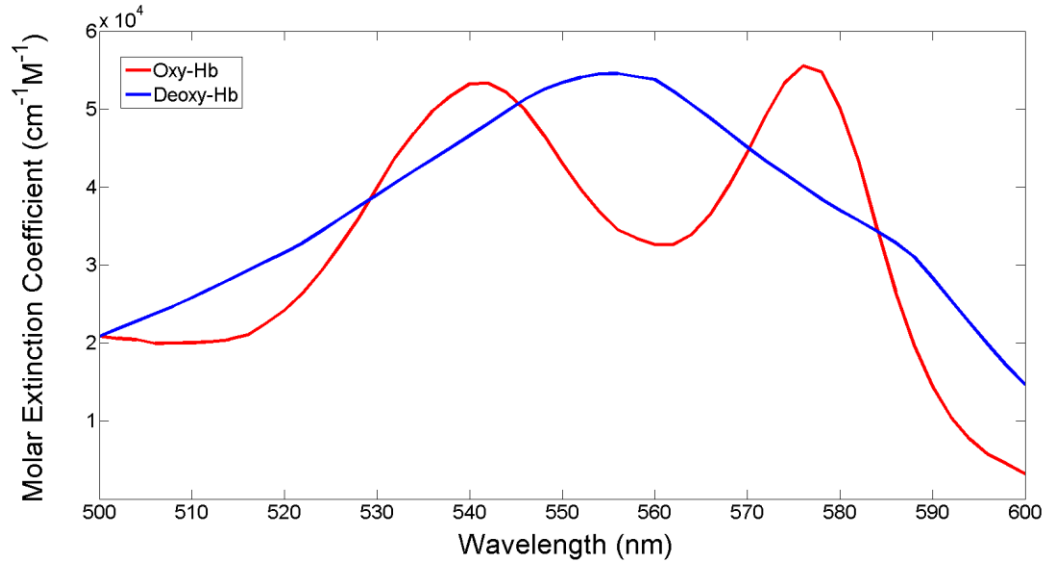
Figure 12: Optical Absorption Spectra of Oxy/Deoxy-Hemoglobin: For a given concentration and optical path length, hemoglobin will produce differing levels of optical absorption depending on its oxygenation status and the wavelength of the incident beam. Oxy-hemoglobin displays a characteristic dip in optical absorption spectrum between 540nm and 580nm. Using spectral processing techniques, these differing absorption spectra can be used to determine the concentrations of either absorber in a mixed sample.

2. Aim 1: Optical Data Processing Techniques for the Analysis of Microenvironmental Parameters in the Dorsal Window Chamber

Studies of the complex interrelationship among radiation damage, vascular remodeling, and HIF-1 expression can only be thoroughly achieved through the observations of relevant spatial and temporal factors. Thus, the dorsal window chamber presents itself as the ideal model system in which highly-resolved, non-invasive, serial measurement may be performed in a living animal. Despite these advantages, however, investigation of tumor vascular parameters through image analysis has remained primarily qualitative in nature, lacking an efficient, unbiased, quantitative method of extracting data. This is largely due to the lack of automated algorithms which can rapidly and accurately process images without the need for human interaction. The first aim of the research presented here encompasses the generation of such methods.

2.1 Structural Analysis

One of the most significant challenges to the automatic quantification of vascular structural parameters is the identification of the vessels themselves. A number of approaches towards automated or semi-automated vessel segmentation have been explored in the literature[209-215]. These methods tend to produce good results for their intended imaging modality (most often retinal imaging or MRI). However, when the publicly available algorithms were applied to dorsal window chamber images, the smaller, tortuous vessels associated with an angiogenic response were often missed.

Generally, these algorithms are optimized for the analysis of images in which vessels

can be largely considered morphologically "normal" (i.e. smooth, regularly branching,

homogenously dense, and conforming to a cylindrical model). A tubular vessel structure

is often implicitly assumed, as many of these methods rely on the detection of large

differences in the image intensity gradient along orthogonal vectors (i.e. vessels are

constant in intensity along vessel centerlines, and intensity changes abruptly in the

transverse direction). This leads to problems when attempting to identify

characteristically "angiogenic" vessels (Figure 13). Therefore, we have developed a

unique algorithm for the automatic identification of tumor-associated vasculature,

which is tuned towards the detection of small, densely packed, tortuous vessels. This

algorithm is described below.

Our method tends to successfully identify tumor-associated vasculature at the

expense of larger, more "normal" vessels. However, for the purposes of modeling

tumor-associated vascular morphology, these vessels should be excluded anyway;

fluorescence-based identification of the tumor area allows us to spatially isolate and

quantify only parameters of the tumor-associated vessels.
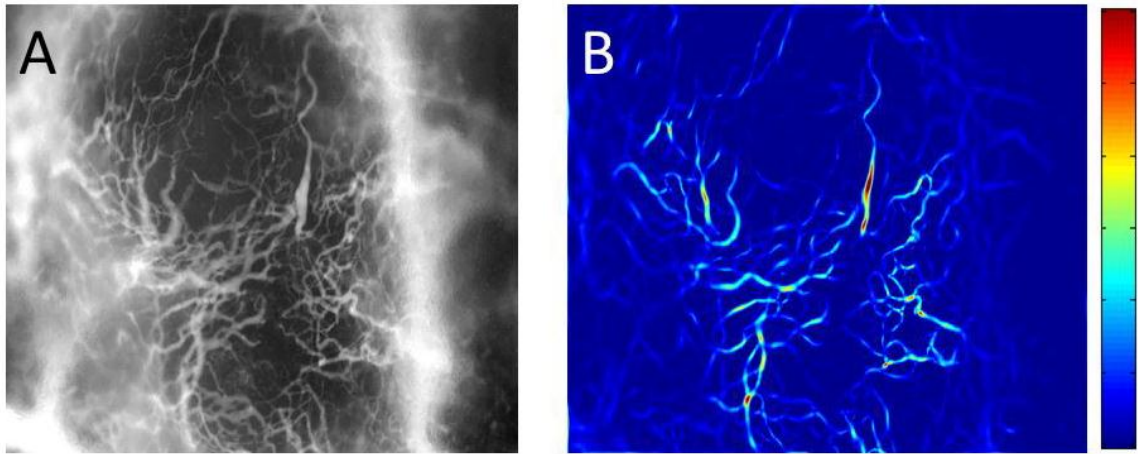
Figure 13: Vessel Identification Using a Publicly Available Algorithm: Vascular hemoglobin concentration images (A) were used as input to an algorithm based off of *Frangi, et al*. The algorithm produced a map representing arbitrary units of vessel confidence (B). The algorithm positively identified vessels with a more normal shape, but tended to miss vessels with typical angiogenic morphologies.

2.1.1 Hyperspectral Acquisition of Hemoglobin and Fluorescent Reporter Spectral Data

Mice implanted with a dorsal window chamber were anesthetized using 1.5% vaporized isofluroane in medical air. The window chamber frame was then mounted to a custom-built block and attached to a standard scientific microscope (Zeiss Axio Observer.D1). The window was imaged at 2.5x and 1.25x magnification using a hyperspectral imaging system.

For the purposes of measuring vascular hemoglobin saturation and total hemoglobin content, the window was trans-illuminated by a broad spectrum halogen source, and a series of 11 images were acquired at 10nm increments between 500nm and

600nm. Hemoglobin optical absorption in this band has distinct spectral profiles depending on whether or not it is bound to oxygen. Applying a modification of the Beer-Lambert Law to account for scattering, the wavelength-dependent optical absorption in tissue can be modeled as

$$-log_{10}\left[\frac{I(\lambda)}{I_0(\lambda)}\right] = c_1\varepsilon_{O_2 \cdot Hb}(\lambda) + c_2\varepsilon_{R \cdot Hb}(\lambda) + c_3\mu_{eff}(\lambda) + c_4$$

where I and I_0 are the input and output optical intensities. The ε and μ_{eff} terms represent hemoglobin molar extinction coefficients and tissue scattering parameters, respectively, and the c terms represent their corresponding absorber concentrations. c_4 accounts for constant changes in the spectral signal due to the input source, spectral reflection, etc.

Prior to analysis, a system calibration was done to correct for the non-uniform spectral density of the light source, system transfer functions, and detector response. These calibration data were acquired from hyperspectral images that were collected with the same source intensity and wavelength-dependent exposure times, but without a sample in the system. Neutral density filters were used to limit light throughput so that detector saturation would not occur. The observed spectrum (after adjustement to compensate for the neutral density filters) is represented by the $I_0(\lambda)$ term. This is the "input" spectrum that is modulated by the sample to produce the "output" spectrum, $I(\lambda)$. The negative logarithm of the ratio of these two parameters is the wavelength-dependent sample absorbance.

The absorbance quantity represents our observed data. The terms to the right represent the contribution of assumed attenuation components to the observed spectrum. The disparate shapes of the component spectra allow for the reconstruction of constituent absorber/scatterer concentrations based off the shape of the combined signal. Since the system of equations is overdetermined when we consider the discrete spectral steps separately, we were able to achieve reconstruction of the attenuation parameters using a non-negative least-squares linear regression algorithm implemented in MATLAB (using published hemoglobin and tissue absorption spectra as inputs). Pixel-by-pixel calculations were performed to extract these concentration parameters at every spatial coordinate, producing quantitative images of hemoglobin saturation and total concentration at every resolvable location.

A similar procedure was used to quantify GFP and RFP expression in the window chamber, since tissue autofluorescence can be an obstacle to accurate quantification of reporter signals. In this case, the window was epi-illuminated at the relevant reporter's excitation peak. The fluorescent reporter and the autofluorescence emission spectra were then empirically calculated from hyperspectral image series. These were then used as inputs to the linear regression algorithm to generate an isolated reporter image (Figure 14).
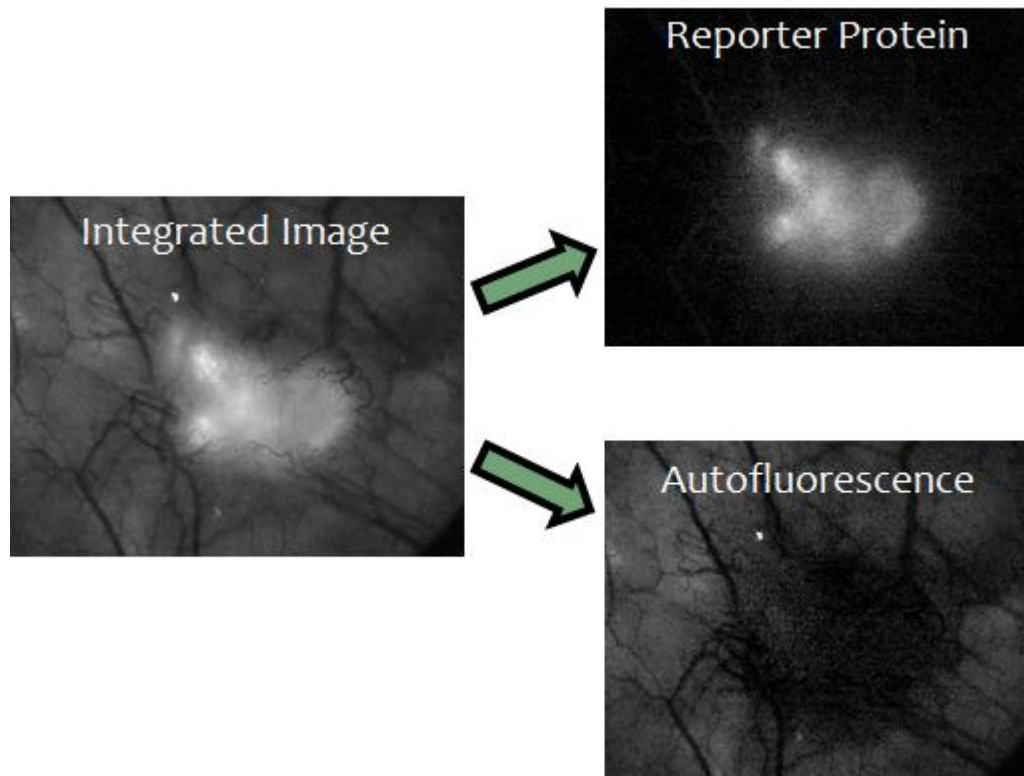
Figure 14: Separation of Spectral Components Using Hyperspectral Techniques: Reporter proteins can be spectrally separated from autofluorscence using hyperspectral techniques. After empirically measuring the spectral profile of both components, their individual contributions to the measured signal can be extracted using linear least-squares regression models.

2.1.2 Tumor Regional Demarcation

In order to more thoroughly model radiation response, the tumor and surrounding normal tissue were segmented into distinct physiological regions within the captured images. This was achieved using the fluorescent reporters expressed in this particular cell line. Fluorescence signal was computationally separated from the background autofluorescence using the hyperspectral technique described above.

Regions of the image where the signal component from the fluorescent reporter exceeded the autofluorescence component by some constant factor (empirically determined) defined the tumor area. The boundary between these two regions was either dilated outward to form the tumor-associated normal tissue region, or was eroded inward to form the tumor rim region. Areas of the tumor inwards of the tumor rim were defined the tumor core.

For the purposes of this study, areas up to 500μm outwards from the tumor-normal tissue boundary were classified as tumor-associated normal tissue. Within this region, vessels were observed to take on the more chaotic physical characteristics of vasculature under the influence of angiogenic signaling factors. Regions of the tumor up to 300μm inward from the boundary were classified as the tumor rim. Within this region, vessels were relatively denser than within the tumor core, and tended to show the highest gradients in oxygenated hemoglobin content. Areas greater than 300μm inward from the tumor boundary were classified as tumor core.

2.1.3 Vessel Identification

2.1.3.1 Generating the Vessel Mask

Within MATLAB, structural parameters of the vascular network were extracted from the total hemoglobin image (the sum of the oxy- and deoxy-hemoglobin images obtained through hyperspectral imaging, as described above). This digital image was represented as a two-dimensional matrix, **H**, of size $r \times c$. **H** was used to generate a

binary mask matrix, **B**, in which "on" (or "1") pixels identify vessels, and "off" (or "0")

pixels mask out non-vascular regions. (In the notation used here, matrices are

represented by bolded letters, and superscripts are used to denote the step in masking

procedure. Generalized elements of a matrix are represented as a non-bolded letter with

index variables in the subscript. Elements within brackets (e.g. $\{x_i\}$) will take on binary

values, which when interpreted as logic statements, may be operated on by the "and"

($\wedge$) or "or" ($\vee$) operators.)

In the first step of mask generation, elements more than two standard deviations

above the mean of **H** were assigned an "on" value.

$$B_{i,j}^{(1)} = \begin{cases} 1, & H_{i,j} > \bar{H} + 2 \times \sqrt{\dfrac{1}{r \cdot c} \sum_{i',j'} \left(H_{i',j'} - \bar{H} \right)^2} \\ \\ 0, & otherwise \end{cases}$$

where

$$\bar{H} \equiv \frac{1}{r \cdot c} \sum_{i',j'} H_{i',j'}$$

This simple threshold identified larger vessels that would not be picked up in later

stages of the masking algorithm.

For every element in the image matrix **H**, the algorithm analyzed the hemoglobin

values along a series of line segments radiating from that pixel. These line segments

consisted of the vertical, horizontal, and the 45° and 135° diagonals, extending a given

number of pixels, z, (typically 25 for 2.5x magnification, or until the image boundary

was reached) away from the selected pixel, H_{i_0,j_0}. The row vectors representing these

line segments were

$$a_1 = \left[H_{(i_0+\langle 0\rangle -z, j_0)} \quad H_{(i_0+\langle 1\rangle -z, j_0)} \quad H_{(i_0+\langle 2\rangle -z, j_0)} \quad \cdots \quad H_{(i_0+\langle 2z\rangle -z, j_0)}\right]$$

$$a_2 = \left[H_{(i_0, j_0+\langle 0\rangle -z)} \quad H_{(i_0, j_0+\langle 1\rangle -z)} \quad H_{(i_0, j_0+\langle 2\rangle -z)} \quad \cdots \quad H_{(i_0, j_0+\langle 2z\rangle -z)}\right]$$

$$a_3 = \left[H_{(i_0+\langle 0\rangle -z, j_0+\langle 0\rangle -z)} \quad H_{(i_0+\langle 1\rangle -z, j_0+\langle 1\rangle -z)} \quad H_{(i_0+\langle 2\rangle -z, j_0+\langle 2\rangle -z)} \quad \cdots \quad H_{(i_0+\langle 2z\rangle -z, j_0+\langle 2z\rangle -z)}\right]$$

$$a_4 = \left[H_{(i_0+\langle 0\rangle -z, j_0-\langle 0\rangle -z)} \quad H_{(i_0+\langle 1\rangle -z, j_0-\langle 1\rangle -z)} \quad H_{(i_0+\langle 2\rangle -z, j_0-\langle 2\rangle -z)} \quad \cdots \quad H_{(i_0+\langle 2z\rangle -z, j_0-\langle 2z\rangle -z)}\right]$$

These vectors were individually smoothed using a 5-span "moving average" method to

reduce image noise. The location of the local maxima and minima along each vector

were calculated, and the four local maximum/minimum pairs that straddled the center

pixel were used for comparison ($a_{1(min)}$, $a_{1(max)}$, etc.). If the center pixel had a

hemoglobin value closer to the value of the maximum than to the minimum for a

particular vector, that vector calculated the center pixel as a "vessel" pixel. If the

hemoglobin value was closer to the value of the minimum than the maximum, the

vector calculated the center pixel as a "non-vessel" pixel. If at least three vectors

calculated the center pixel as a "vessel" pixel, the corresponding pixel in the vessel mask

was assigned an "on" value:

$$c_n = \begin{cases} 1, & (a_{n(max)} - a_{n(0)}) < (a_{n(0)} - a_{n(min)}) \\ 0, & (a_{n(max)} - a_{n(0)}) \geq (a_{n(0)} - a_{n(min)}) \end{cases}$$

and

$$B_{i_0,j_0}^{(2)} = \begin{cases} 1, & \sum_{n=1}^{4} c_n \geq 3 \\ \\ 0, & otherwise \end{cases}$$

2.1.3.2 Filtering the Vessel Mask

In order to filter out the speckle noise and rough edges that would otherwise generate artifacts in later steps, the mask image (as generated above) was subjected to additional filtering using a series of neighborhood operations. In applying these operations, the state of each element in the output matrix was calculated according to the values of the 3x3 region its corresponding element in the input matrix was bounded within. The 3x3 neighborhood was passed to a function that returned a value of "on" if and only if the defined neighborhood condition was true (Table 1).

Table 1: Vessel Masking and Skeletonization Neighborhood Operations

Neighborhood Operation	Condition $\begin{pmatrix} \boxed{p_1}\ \boxed{p_2}\ \boxed{p_3} \\ \boxed{p_8}\ \boxed{p_0}\ \boxed{p_4} \\ \boxed{p_7}\ \boxed{p_6}\ \boxed{p_5} \end{pmatrix}$	Binary Output Variable
"Identity"	$\{p_0 = 1\}$	q_I
"Erode"	$\{p_0 = 1\} \wedge \left\{ \left(\sum_{n=1}^{8} p_n \right) \leq 8 \right\}$	q_E
"Fill"	$\{p_0 = 0\} \wedge \left\{ \left(\sum_{n=1}^{8} p_n \right) \geq 5 \right\}$	q_F
"Remove"	$\{p_0 = 1\} \wedge \left\{ \left(\sum_{n=1}^{4} p_{2n} \right) \leq 1 \right\}$	q_R

"Connector"	$\{p_0 = 1\} \wedge \left\{\left(abs(p_8 - p_1) + \sum_{n=1}^{7} abs(p_n - p_{n+1})\right) \geq 4\right\}$	q_C
"Outer Boundary"	$\{p_0 = 0\} \wedge \left\{\left(\sum_{n=1}^{8} p_n\right) \geq 1\right\}$	q_{OB}
"Inner Boundary"	$\{p_0 = 1\} \wedge \left\{\left(\sum_{n=1}^{4} p_{2n}\right) \leq 4\right\}$	q_{IB}
"Square Joiner"	$\{p_0 + p_1 + p_2 + p_8 = 4\} \vee \{p_0 + p_2 + p_3 + p_4 = 4\} \vee$ $\{p_0 + p_4 + p_5 + p_6 = 4\} \vee \{p_0 + p_6 + p_7 + p_8 = 4\}$	q_S
"End Point"	$\{p_0 = 1\} \wedge \left\{\left(\sum_{n=1}^{8} p_n\right) = 1\right\}$	q_{EP}
"Reconnector"	$\{p_0 = 0\} \wedge \left\{\left(abs(p_8 - p_1) + \sum_{n=1}^{7} abs(p_n - p_{n+1})\right) \geq 4\right\} \wedge$ $\left\{\frac{abs\big((p_1 + p_2 + p_3) - (p_5 + p_6 + p_7)\big)}{\sum_{n=1}^{8} p_n} \leq \frac{1}{2}\right\} \wedge$ $\left\{\frac{abs\big((p_1 + p_7 + p_8) - (p_3 + p_4 + p_5)\big)}{\sum_{n=1}^{8} p_n} \leq \frac{1}{2}\right\} \wedge$ $\neg\{\{p_1 + p_2 + p_3 = 2\} \wedge \{p_4 + p_8 = 1\} \wedge \{p_5 + p_6 + p_7 = 1\}\} \wedge$ $\neg\{\{p_1 + p_2 + p_3 = 1\} \wedge \{p_4 + p_8 = 1\} \wedge \{p_5 + p_6 + p_7 = 2\}\} \wedge$ $\neg\{\{p_1 + p_7 + p_8 = 2\} \wedge \{p_2 + p_6 = 1\} \wedge \{p_3 + p_4 + p_5 = 1\}\} \wedge$ $\neg\{\{p_1 + p_7 + p_8 = 1\} \wedge \{p_2 + p_6 = 1\} \wedge \{p_3 + p_4 + p_5 = 2\}\} \wedge$ $\neg\{\{p_1 + p_2 + p_3 = 3\} \wedge \{p_4 + p_8 = 0\}\} \wedge$ $\neg\{\{p_5 + p_6 + p_7 = 3\} \wedge \{p_4 + p_8 = 0\}\} \wedge$ $\neg\{\{p_1 + p_7 + p_8 = 3\} \wedge \{p_2 + p_6 = 0\}\} \wedge$ $\neg\{\{p_3 + p_4 + p_5 = 3\} \wedge \{p_2 + p_6 = 0\}\}$	q_{RC}
"Not-Empty Structure"	$\left\{\left(\sum_{n=1}^{8} p_n\right) > 0\right\}$	q_{NS}
"Box Structure"	$\{p_0 = 0\} \wedge \left\{\left(\sum_{n=1}^{8} p_n\right) \geq 7\right\}$	q_{BS}

"One-Corner Structure"	$\left\{\left(\sum_{n=1}^{8} p_n\right) = 1\right\} \wedge \{p_1 + p_3 + p_5 + p_7 = 1\}$	q_{1S}
"Two-Corner Structure"	$\{p_0 = 0\} \wedge \{p_1 + p_3 + p_5 + p_7 = 2\}$	q_{2S}
"Branch Point"	$\{p_0 = 1\} \wedge \left\{\left(abs(p_8 - p_1) + \sum_{n=1}^{7} abs(p_n - p_{n+1})\right) \geq 6\right\}$	q_{BP}
"Length 1"	$\{p_0 = 1\} \wedge \left\{\left(\sum_{n=1}^{4} p_{2n}\right) = 1\right\} \wedge \left\{\left(\sum_{n=1}^{4} p_{2n-1}\right) = 0\right\}$	q_{L1}
"Length $\sqrt{2}$"	$\{p_0 = 1\} \wedge \left\{\left(\sum_{n=1}^{4} p_{2n}\right) = 0\right\} \wedge \left\{\left(\sum_{n=1}^{4} p_{2n-1}\right) = 1\right\}$	q_{LSq2}
"Length 2"	$\{p_0 = 1\} \wedge \left\{\left(\sum_{n=1}^{4} p_{2n}\right) = 2\right\} \wedge \left\{\left(\sum_{n=1}^{4} p_{2n-1}\right) = 0\right\}$	q_{L2}
"Length $1 + \sqrt{2}$"	$\{p_0 = 1\} \wedge \left\{\left(\sum_{n=1}^{4} p_{2n}\right) = 1\right\} \wedge \left\{\left(\sum_{n=1}^{4} p_{2n-1}\right) = 1\right\}$	q_{L1+Sq2}
"Length $2\sqrt{2}$"	$\{p_0 = 1\} \wedge \left\{\left(\sum_{n=1}^{4} p_{2n}\right) = 0\right\} \wedge \left\{\left(\sum_{n=1}^{4} p_{2n-1}\right) = 2\right\}$	q_{L2Sq2}

First, $\mathbf{B}^{(2)}$ was "eroded" such that all "on" pixels bordering an "off" pixel on one of its four edges were turned off ($\neg q_E$). Groups of interconnected "on" pixels less than a pre-defined limit (25 pixels for 2.5x magnification images) were then turned off. All boundary pixels were then returned to their "on" state, with the exclusion of the boundary pixels associated with areas removed in the area threshold step; the filtered mask matrix $\mathbf{B}^{(3)}$ was thus produced. This process helped eliminate troublesome "spur" artifacts that projected from the true vessel mask, giving it a rough edge.

In the fourth step, an iterative filtering process (Figure 15) was applied to the mask to close artificial gaps and remove false positives while preserving vessel connectivity. In the first iteration of the newly generated mask, $\mathbf{B}^{(4)}$, the value of any particular element was assigned a value equivalent to the value of the proposition

$$\{q_I \lor q_F\} \land \{\neg q_R \lor q_C\}$$

for the associated neighborhood in $\mathbf{B}^{(3)}$. For all following iterations, the output of the previous iteration ($\mathbf{B}^{(4)}$) was used as the new input ($\mathbf{B}^{(4)'}$), while applying the same neighborhood logic. This process continued until the operations produced no change in state between $\mathbf{B}^{(4)}$ and $\mathbf{B}^{(4)'}$.
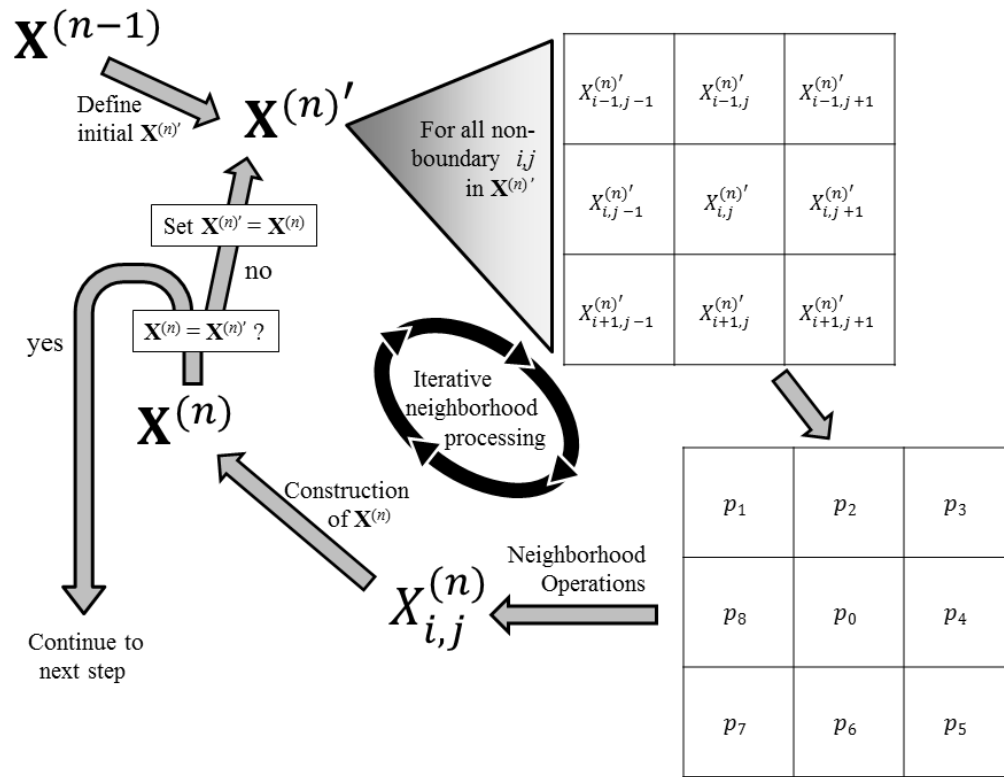
Figure 15: Iterative Neighborhood Processing: The final product of the prior step, $\mathbf{X^{(n-1)}}$, becomes the initial matrix in the iterative process, $\mathbf{X^{(n)'}}$. Neighborhood operations are applied to each element of $\mathbf{X^{(n)'}}$in a series of steps, producing the transformed matrix $\mathbf{X^{(n)}}$. If $\mathbf{X^{(n)}}$ and $\mathbf{X^{(n)'}}$ are not equivalent matrices, the procedure continues, with $\mathbf{X^{(n)}}$ becoming the next $\mathbf{X^{(n)'}}$. Otherwise, the process is complete.

2.1.3.3 Removing Artifacts from the Vessel Mask

After the final $\mathbf{B^{(4)}}$ was calculated, holes (bounded, connected areas of "off"

pixels) in the mask were identified. For each hole, a binary matrix $\mathbf{A}$ was created from

$\mathbf{B^{(4)}}$ in which only connected elements associated with the given hole had values of

"on". The average hemoglobin content of the pixels in $\mathbf{H}$ associated with the hole

boundary, $\mathbf{A_B}$, were calculated (where $\mathbf{A_B}$ was generated by the "boundary" neighborhood operation). If greater than 90% of the pixels in $\mathbf{H}$ associated with the hole had a value within 10% of the average value in the boundary, the hole was identified as an artifact and filled in:

$$\left\{\left(\sum_{i,j}\{H_{i,j} \cdot A_{i,j} \geq 0.9 \times \bar{\mathbf{H}}_{\mathrm{B}}\}\right) > \left(0.9 \times \sum_{i,j}\{A_{i,j}\}\right)\right\} \to Artifact$$

where

$$\bar{\mathbf{H}}_{\mathrm{B}} \equiv \frac{\sum_{i,j}\left(H_{i,j} \cdot A_{B(i,j)}\right)}{\sum_{i,j}\{A_{B(i,j)}\}}$$

Conversely, connected positive artifacts were identified by the ratio of the number of boundary edges to the total number of connected pixels. Since artifacts were observed to have a large perimeter relative to its total size, connected pixels were removed if the calculated ratio was greater than ½:

$$\left\{\left(\frac{\sum_{i,j}\{A_{B(i,j)}\} \times c_{i,j}}{\sum_{i,j}\{A_{(i,j)}\}}\right) > \frac{1}{2}\right\} \to Artifact$$

where $c_{i,j}$ represents the number of boundary edges at the coordinate. This process generated the final vessel mask, $\mathbf{B}$.

2.1.3.4 Skeletonization of the Vessel Mask

In order to calculate various structural parameters of the vessel network, $\mathbf{B}$ was used to produce a skeletonized binary image matrix, $\mathbf{S}$. This process used a number of neighborhood operations in an iterative refining process, as in the generation of $\mathbf{B}^{(4)}$. $\mathbf{B}$

was used as the initial input, from which the values of each element of $\mathbf{S}^{(1)}$ were

determined by the values of a number of neighborhood operations applied to

intermediate matrices. Each element of the intermediate matrices was calculated from a

logical proposition, whose elements (q_I, q_E, etc.) were derived from neighborhood

operations applied to corresponding 3x3 regions in the input:

$$\mathbf{M}_0 \rightarrow \{q_I \wedge \neg q_{OB}\} \vee \{q_C\} \rightarrow \mathbf{M}_1$$

$$\mathbf{M}_0 \rightarrow \{q_C \vee q_{OB}\} \rightarrow \mathbf{M}_{2'}$$

$$\mathbf{M}_0 \rightarrow \{q_{OB}\} \rightarrow \mathbf{M}_{3'}$$

$$\mathbf{M}_{2'} \rightarrow \{q_S\} \rightarrow \mathbf{M}_2$$

$$\mathbf{M}_{3'} \rightarrow \{q_E\} \rightarrow \mathbf{M}_3$$

The elements of these intermediate matrices then determined the corresponding

elements in $\mathbf{M}_4$ through element-wise operations on their binary values:

$$\mathbf{M}_4 = \mathbf{M}_1 \vee \mathbf{M}_2 \vee \mathbf{M}_3$$

Applying the "reconnector" neighborhood operation to $\mathbf{M}_4$ restores vessel connections:

$$\mathbf{M}_4 \rightarrow \{q_I \vee q_{RC}\} \rightarrow \mathbf{S}^{(1)}$$

In the first iteration of this process, $\mathbf{M}_0 = \mathbf{B}$. For future iterations, $\mathbf{M}_0 = \mathbf{S}^{(1)'}$,

where $\mathbf{S}^{(1)'}$ is the output matrix from the previous iteration. The process continues until

the transition from $\mathbf{S}^{(1)'}$ to $\mathbf{S}^{(1)}$ produces no change in state.

After the final iteration, the complement of the binary matrix $\mathbf{S}^{(1)}$ was calculated,

and each one of its edge-connected components was processed separately. $\mathbf{A}$ was the

binary matrix representing the particular connected component. If the sum of all the

elements with an "on" value in the element-wise binary product of **A** and **B** was greater than 95% of the total number of the "on" elements in **A**, then an artifact was identified in the image:

$$\left\{\sum_{i,j}\{B_{i,j} \wedge A_{i,j}\} > 0.95 \times \sum_{i,j}\{A_{i,j}\}\right\} \rightarrow Artifact$$

In the case of an artifact, each element of the mask matrix, $B_{i,j}$, was redefined as $B_{i,j} \vee A_{i,j}$. The entire skeletonization procedure was then repeated from the beginning with the new **B**. This continued until no artifacts were identified, producing $\mathbf{S}^{(2)}$.

This procedure generated a number of vessel centerlines of double-width, rather than single pixel width. The next step pared these double-width skeletonization lines down to single-width, while preserving edge/corner connectivity at the end caps. This was followed by a correction procedure in which troublesome "box" neighborhood structures were specifically identified and modified through neighborhood operations:

$$\mathbf{S}^{(2)} \rightarrow \{q_{BS}\} \rightarrow \mathbf{N}_1$$

$$\mathbf{N}_1 \rightarrow \{\neg q_{NS}\} \rightarrow \mathbf{N}_2$$

$$\mathbf{N}_1 \rightarrow \{q_I \vee q_{1S} \vee q_{2S}\} \rightarrow \mathbf{N}_3$$

Finally, element-wise operations on these binary matrices produced the skeletonization matrix:

$$\mathbf{S} = \left(\mathbf{S}^{(2)} \wedge \mathbf{N}_2\right) \vee \mathbf{N}_3$$

2.1.4 Derivation of Structural Parameters

2.1.4.1 Vessel Diameter

Vessel diameters were calculated from **B** and **S** by applying a disc structure to the elements of **S** in a series of iterations. For the nth iteration, the elements of the disc structure were determined according to

$$D_{n(i,j)} = \begin{cases} 1, & (i^2 + j^2) \leq n^2 \\ 0, & (i^2 + j^2) > n^2 \end{cases}$$

(for simplicity, here we define the indices at the center of the disc as (0,0), whereas in practice, an offset constant was used to avoid non-positive indices). For every "on" element in **S**, the algorithm calculated the element-wise product of **B** and $\mathbf{D}_n$, with $\mathbf{D}_n$ centered upon the element in **B** with the same coordinates as those given for **S**. The vessel diameter at this location was determined by this product. For the element in **S** with coordinates (i_0, j_0),

$$\left\{ \sum_{i,j \in Q} \{B_{i,j} \cdot D_{n(i+i_0 j, +j_0)}\} < \sum_{i,j} \{D_{n(i,j)}\} \right\} \rightarrow Diameter\ at\ (i_0, j_0) = 2 \times (n-1)$$

$$\left\{ \sum_{i,j \in Q} \{B_{i,j} \cdot D_{n(i+i_0 j, +j_0)}\} = \sum_{i,j} \{D_{n(i,j)}\} \right\} \rightarrow Increment\ n\ and\ repeat$$

where

$$Q \equiv \mathbf{B} \cap \mathbf{D}_{n(+i_0, +j_0)}$$

Thus the vessel diameter map, $\mathbf{S}_D$, was constructed, where the binary "on"
values in $\mathbf{S}$ that represented vessel centerlines were reassigned integer values
representing the vessel diameter at that point.

In order to eliminate residual artifacts where the skeletonized image
incorporated previously missed "spurs", the algorithm then identified line segments in
the image which projected strictly vertically or horizontally over the distance of at least
five pixels. Artifacts were identified from the average change in diameter over this
segment:

$$\left\{ abs\left(\frac{1}{z-1}\sum_{k=1}^{z-1}(l_{k+1} - l_k) \right) > \frac{1}{2} \right\} \rightarrow Artifact$$

where l represents the particular line segment with positional index k, and z is the
length of the line segment. Elements of segments identified as artifacts were removed
from $\mathbf{S}$ and $\mathbf{S}_D$. The average vessel diameter in a particular region was calculated as

$$P_D = \left(\sum_{i,j \in R} S_{D(i,j)} \right) \Big/ \left(\sum_{i,j \in R} S_{(i,j)} \right)$$

where R defines the region of interest.

2.1.4.2 Branch Points

Branch points were identified by applying neighborhood operations to the
skeletonization image, $\mathbf{S}$:

$$\mathbf{S} \rightarrow \{q_{BP}\} \rightarrow \mathbf{S}_{BP}$$

The number of branch points, P_{BP}, were calculating as the sum of all "on" elements in $\mathbf{S}_{BP}$. We then calculate a skeletonized image matrix with all branch points removed:

$$\mathbf{S} \to \{q_I \wedge \neg q_{BP}\} \to \mathbf{S}_{BP-}$$

2.1.4.3 Vascular Length Density

The vascular length density within a particular region was calculated from $\mathbf{S}_{BP-}$, where all elements outside the region of interest were set to "off". Neighborhood operations were then applied to this regionally masked matrix, $\mathbf{S}_{BP-}'$:

$$\mathbf{S}_{BP-}' \to \{q_{L1}\} \to \mathbf{L}_1$$

$$\mathbf{S}_{BP-}' \to \{q_{LSq2}\} \to \mathbf{L}_{Sq2}$$

$$\mathbf{S}_{BP-}' \to \{q_{L2}\} \to \mathbf{L}_2$$

$$\mathbf{S}_{BP-}' \to \{q_{L1+Sq2}\} \to \mathbf{L}_{1+Sq2}$$

$$\mathbf{S}_{BP-}' \to \{q_{L2Sq2}\} \to \mathbf{L}_{2Sq2}$$

The total vascular length within the given region of interest was then calculated:

$$P_{VL} = \frac{1}{2}\left(\sum_{i,j}\{L_{1(i,j)}\} + \sqrt{2}\sum_{i,j}\{L_{Sq2(i,j)}\} + 2\sum_{i,j}\{L_{2(i,j)}\} + (1+\sqrt{2})\sum_{i,j}\{L_{1+Sq2(i,j)}\} \right.$$

$$\left. + 2\sqrt{2}\sum_{i,j}\{L_{2Sq2(i,j)}\} \right)$$

(The preceding ½ accounts for the fact that each pixel connection is counted twice in the neighborhood operations.) The vascular length density parameter, P_{VLD}, is then calculated as P_{VL} divided by the total number of elements within the region of interest.

81

2.1.5 Validation of Structural Parameters

In order to validate the accuracy of the structural algorithm, comparisons were made between code skeletonized images and manual centerline traces in a blinded analysis. Four different data sets were used (example shown in Figure 16). Code-based vascular length calculations were consistently less than manual-based measurements by a mean value of 25%, with a standard deviation of 8.5%. Relatively large discrepancies in calculation were expected however, since manual traces and computer calculations relied on different interpretations of what constitutes a vessel. However, the relative difference between methods was largely consistent, suggesting that the same categories of vessels were consistently differently identified. In fact, when images of line traces were compared, broad features tended to overlap well (Figure 17). The differences in vessel identification tended to consist of indistinct, questionable vessels segments that the code excluded. Due to the human tendency to assume connects between disjoined vessel segments, we speculate that this algorithm was less biased in its interpretations. In any case, the results of this comparison were consistent enough to assume that estimations of vascular parameters are accurate in comparison to human calculations, factoring in variations in human-computer selection criteria.
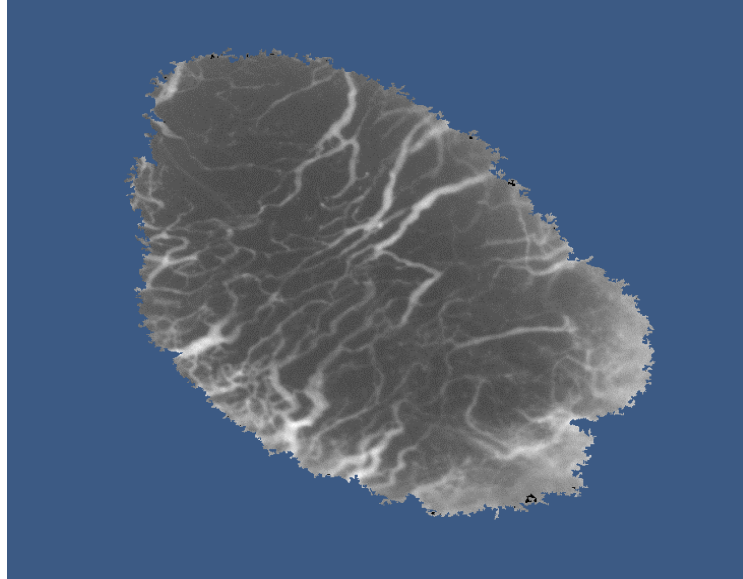
Figure 16: A Sample Image Used for Comparisons of Manual and Code-Based Vessel Identification: These images were derived from hyperspectral calculations of vascular hemoglobin concentration. Higher concentrations appear brighter. Areas outside the tumor were masked.
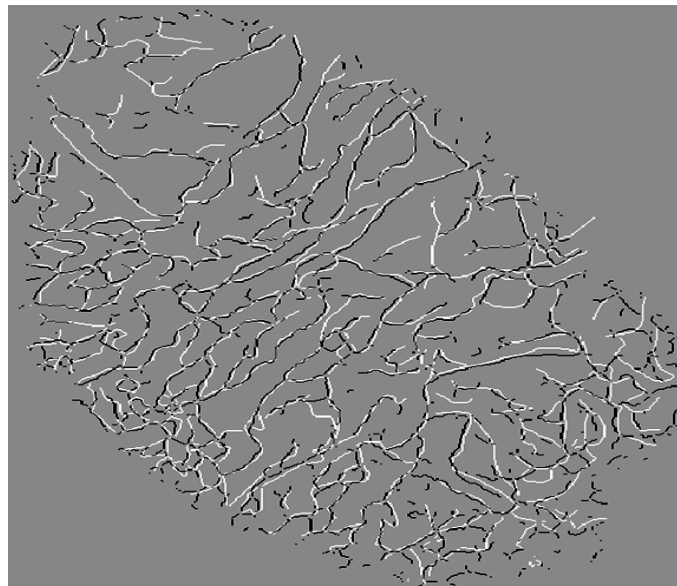
Figure 17: A Visual Comparison of the Manual and Code-Based Vessel Traces: Human and computer identifications of vessel centerlines are shown superimposed upon one another. The black lines represent computer calculations while the white represent human traces.

2.2 Functional Analysis

Vascular functionality is a key component in the study of many physiological systems wherein vascular flow characteristics are modulated by and/or indicative of oxygen availability, paracrine signaling, or metabolic demand. Investigation of such systems from a hemodynamic perspective provides insight into tissue function, as in studies of developmental vasculogenesis[216], cortical brain function[217], tumor hypoxia/angiogenesis dynamics[24], wound healing characteristics[218,219], etc. Blood flow analysis may also aid in the detection of a number of vascular pathologies wherein deficient oxygen/nutrient transport leads to tissue injury or accelerated malignant progression. For example, the eye particularly lends itself to such assessment due to the optical accessibility of its vasculature, and the incorporation of these data in clinical diagnoses is already commonplace[220]. In the early stages of disease, these pathological conditions may be most easily detected through the observation of aberrant hemodynamics. However, the ability to generate dynamic, highly-resolved blood velocity maps in a technically simple and automated manner has been an elusive goal, and the lack of such methods has restricted the widespread analysis of hemodynamic data in both laboratory and clinical applications.

Optical methods of measuring microvascular blood velocity have a long history due to their ability to non-invasively resolve dynamics at the level of single microvessels[221,222]. For decades, the dual-slit technique was the standard method for

measuring blood velocity in pre-clinical models, and its application continues today due to its versatility, simplicity, and inexpensiveness. This method uses dual acquisition windows to capture fluctuating optical signals at two points along a vessel. The peak of the cross-correlation between these two signals identifies the temporal delay between them from which velocity may be calculated. A magnified, video-rate recording of blood movement within the sample is all that is required in the data-collection phase. However, a drawback of this approach is the need for user-guided placement of signal acquisition windows for every vessel segment of interest in the data-processing phase. Thus, a complete observation of hemodynamic characteristics within the observable vascular network would require the manual placement of numerous window pairs on vessels within the region of interest—a laborious process that is prone to selection bias.

These drawbacks have prompted the development of a number of other approaches to the analysis of video-based data[223]. Techniques that implement continuous velocity measurements along vessel centerlines can capture subtle variations in hemodynamic patterns, at the cost of time-consuming manual vessel traces[224,225]. These techniques are insensitive to variations in velocity across vessel profiles. The development of a semi-automated method, that tracks individual red blood cells through capillaries while simultaneously measuring the oxygen saturation of these cells represented a major advance in the observation of microvascular oxygen transport[226]. This method requires user guidance, though, and may be limited to the analysis of

85

capillary flow, where single cells can be tracked from frame to frame. Recently, an algorithm based on a cross-correlation analysis was demonstrated in a glioma model, providing impressive blood velocity maps[227]. However, this method processes temporal delays equivalent to only a single frame offset. When tested in our approach and compared to the results of processing multiple sequential frames, this led to less accurate results, a more limited range of measurable velocity magnitudes, and incomplete determination of direction.

Thus it seems that video-based techniques, although technically straightforward, have inherent limitations, and are not ideal for the study of complex networks with large numbers of vessel segments. When investigating time-dependent changes in velocity patterns, these limitations restrict the ability to obtain and analyze spatial and temporal information in vascular networks due to the sheer quantity of manual interactions required.

As an alternative to video-based methods, a number of spectroscopic techniques have recently emerged as a result of improvements in optical technology, computational efficiency, and digital signal acquisition/processing. Laser Doppler velocimetry is commonly used to extract volumetric blood velocity data in optical settings where individual vessels cannot be resolved[228]. Within optically accessible tissues, optical coherence tomography (OCT) is perhaps the most widely used spectroscopic technology, and its incorporation in the clinic as an ocular imaging technique has proven

a valuable diagnostic resource. Even with the incorporation of Doppler-based calculations of velocity, however, the acquisition times needed to overcome confounding noise may limit its ability to detect and quantify rapidly changing or unstable dynamics. Due to insensitivity to movement perpendicular to the beam direction, Doppler calculations may also be missing or inaccurate for a number of vessels, especially in samples where the vascular network is largely planar[229]. Laser speckle imaging may partially alleviate these drawbacks with faster acquisition times and less directional sensitivity, but like OCT, this method cannot easily extract complete directional information[230]. Furthermore, these methods require expensive and technically challenging optical setups.

To address these challenges, we set out to create an inexpensive, easily implementable and fully automated method for analyzing functional dynamics of vascular networks. This "mapping algorithm" extracts hemodynamic data from video images without the need for complex optical technology. It generates easily interpretable and accurate speed and direction maps, and eliminates the need for human guidance, thus avoiding user bias in data analysis. This efficient method of processing video sequences facilitates the investigation of large (both spatially and temporally) data sets.

One limitation of the method is its inability to analyze data in three spatial dimensions. In a number of systems, however, vascular networks can be reasonably approximated in two spatial dimensions, or two-dimensional samples of a three-

dimensional network supply representative hemodynamic characteristics. Several such examples are presented below. Prior studies have also demonstrated the ability of video-based techniques to observe and quantify microcirculatory function in a number of organs under both normal and pathological conditions[231]. Neither does this two-dimensional limitation represent a major disadvantage in the depth of vessel detection, since even the most advanced optical imaging systems are fundamentally limited to operation within a few hundred microns from the surface due to rapid photo-attenuation in tissue.

Fundamentally, the presented mapping algorithm represents a substantial advance in the processing of two-dimensional image sequences, which is a widely used method of acquiring microcirculatory hemodynamic data. Furthermore, it's simplicity (from a hardware perspective) allows for it to be easily and cheaply integrated into existing optical systems, making it a valuable tool in certain biological studies where the incorporation of advanced optical hardware is not practical.

2.2.1 Video Capture and Registration

Videos of blood movement were collected and quantified in the dorsal window chamber using the same optical setup as described in 2.1. The window was trans-illuminated with the broad spectrum halogen source. To enhance hemoglobin contrast, the liquid crystal tunable filter was set to 520 nm, a wavelength at which both oxy- and deoxy-hemoglobin display a high degree of optical absorption. A 5x objective was used

to resolve discrete red blood cells as they moved through the vasculature. In its video

capture mode, the CCD camera recorded 128 frames at 24 frames per second. The

resultant video was saved as a multipage image file.

Small linear shifts between consecutive frames were often a result of the animal's

respiratory and cardiac movements. In order to negate these effects, the video was

processed frame-by-frame in MATLAB to find the relative horizontal and vertical pixel

shifts that produced the smallest composite intensity differences between frames,

$min_{(m,n)}(\mathbf{R})$, where

$$R_{m,n} = \sum_{i,j \in Q} \left(F_{1(i,j)} - F_{2(i+m,j+n)} \right)^2$$

and

$$Q \equiv \mathbf{F_1} \cap \mathbf{F_{2(+m,+n)}}$$

(where $\mathbf{F_{2(+m,+n)}}$ denotes indices in $\mathbf{F_2}$ offset by m rows and n columns relative to $\mathbf{F_1}$).

For consecutive frames $\mathbf{F_1}$ and $\mathbf{F_2}$, $\mathbf{F_2}$ was shifted by $-m_0$ and $-n_0$, where m_0 and n_0 are

the indices where $\mathbf{R}$ has its minimum value. Continuing this process throughout

generated a registered image sequence. This sequence was represented as a three

dimensional matrix, $\mathbf{A}$, of size $M \times N \times P$. Where M and N are the number of rows and

columns of pixels in each frame, and P is the total number of captured frames. In order

to simplify future calculations, $\mathbf{A}$ was transformed into $\mathbf{A'}$, where the DC component

along the temporal dimension was removed:

$$A'_{i,j,k} = A_{i,j,k} - \frac{1}{P} \sum_{k'=1}^{P} A_{i,j,k'}$$

2.2.2 Preliminary Masking of Video Data

In the initial stages of analysis, a map was generated which indicated the degree to which pixels fluctuated coherently with their surrounding pixels. For a given spatial coordinate, (i_0, j_0), the DC-subtracted temporal signal at that coordinate $(\vec{S}_0)$ was compared to that of each of the eight surrounding coordinates $(\vec{S}_1 ... \vec{S}_8)$. Inner products were calculated, and the total number of positive elements (representing signals increasing or decreasing together at a particular time) was assigned as a value for that particular coordinate:

$$R_{i_0, j_0} = \sum_{n=1}^{8} \sum_{k=1}^{P} \{\vec{S}_{0(k)} \cdot \vec{S}_{n(k)} > 0\}$$

The derived coherence map, **R**, was used to enhance efficiency by excluding the processing of pixels that did not fluctuate in synch with surrounding pixels (indicating they did not constitute an area of blood flow), based off of some threshold value for R_{i_0, j_0}. This map was also used as a color-intensity weighting factor for various visualization schemes.

2.2.3 Calculation of Speed and Direction

For a given coordinate, (i_0, j_0), the associated temporal signal was compared to the signals in the surrounding area using a cross-correlation approach. Maximum values of the cross-correlation vector represented the temporal offset between the two signals which produced the best alignment. For the given coordinate, $\mathbf{C}$ thus represented a local map of temporal offsets relative to the signal at (i_0, j_0):

$$C_{i',j'} = max_{(\tau)}\left(\vec{S}_{i_0,j_0} \star \vec{S}_{i',j'}\right)$$

where $C_{i',j'}$ takes on the value of the frame shift (τ) that maximizes the cross-correlation term. In order to limit the number of calculations, the ranges of i' and j' are typically limited to a few hundred pixels centered upon (i_0, j_0). (Figure 18 shows an example image of $\mathbf{C}$ taken from real data.)
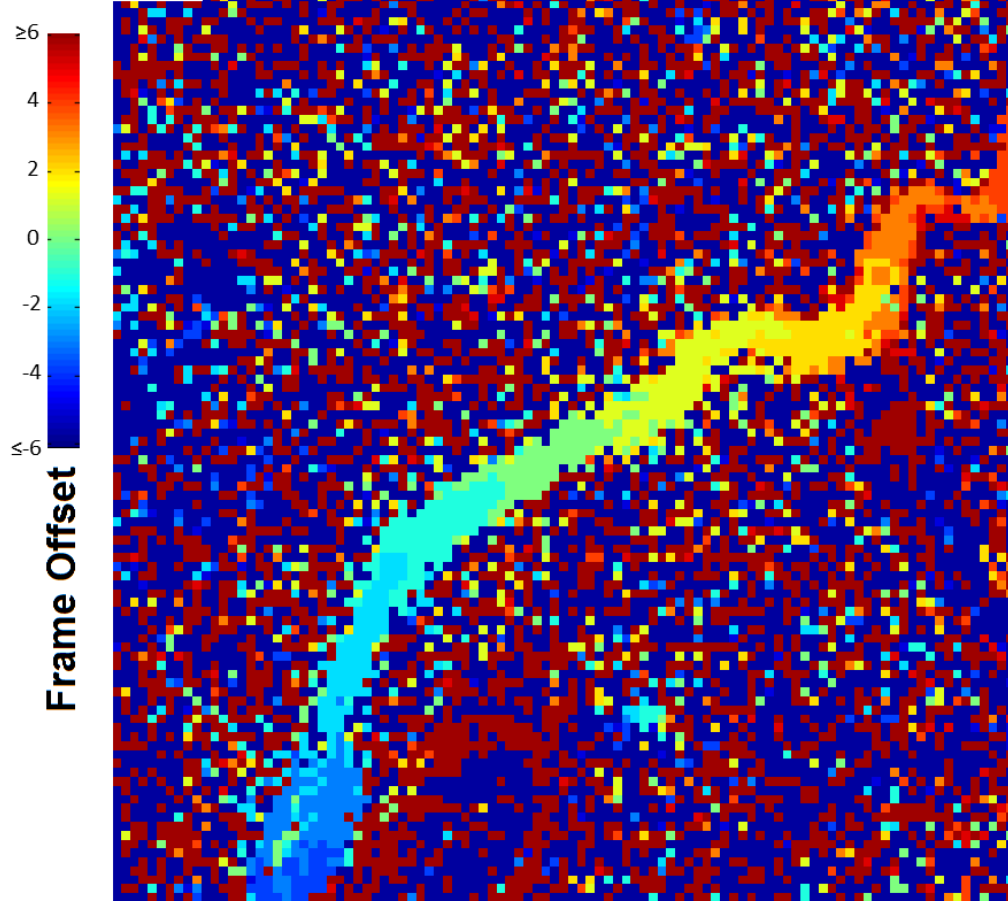
Figure 18: A Map of Frame Offsets: This image shows a map of frame offsets derived from hemodynamic data. The temporal signal at each coordinate was compared to the signal of interest (center coordinate), and the frame offset that produced the best signal correlation (i.e. maximized the cross-correlation) was mapped. The speed at this particular coordinate was calculated to be 0.656 mm/s. The algorithm will produce a local correlation matrix (from which to calculate velocity) for every spatial coordinate, in turn.

For computational efficiency, the cross-correlation operations were performed in the Fourier domain by employing the convolution theorem, which states that the Fourier transform of two convolved signals is equivalent to the product of their individual transforms. Therefore,

$$\vec{S}_{i_0,j_0} \star \vec{S}_{i',j'} = \mathcal{F}^{-1}\left[\mathcal{F}(\vec{S}_{i_0,j_0}) \cdot \mathcal{F}(\vec{S}_{i',j'})^*\right]$$

(Since we wished to calculate the cross-correlation of the signals rather than their convolution, one signal was reversed in time by taking the complex conjugate of its Fourier transform.)

After **C** was calculated, the algorithm identified large, spatially contiguous regions of common offset values within the matrix. Isolated values, or contiguous regions that contained less than the specified minimum number of elements, were ignored. For each offset value, the largest retained region was used for calculations of velocity. The Euclidian distance from centroid to centroid of incrementing regions represented the distance a given cluster of blood cells traveled from frame to frame. By measuring the direction and distance between these centroids, direction and speed could be calculated for the coordinate of interest. Pixels that failed to produce a given number of incremental offset regions were identified as non-flowing. This process was repeated for every pixel, generating complete speed (Figure 19) and direction (Figure 20) maps.
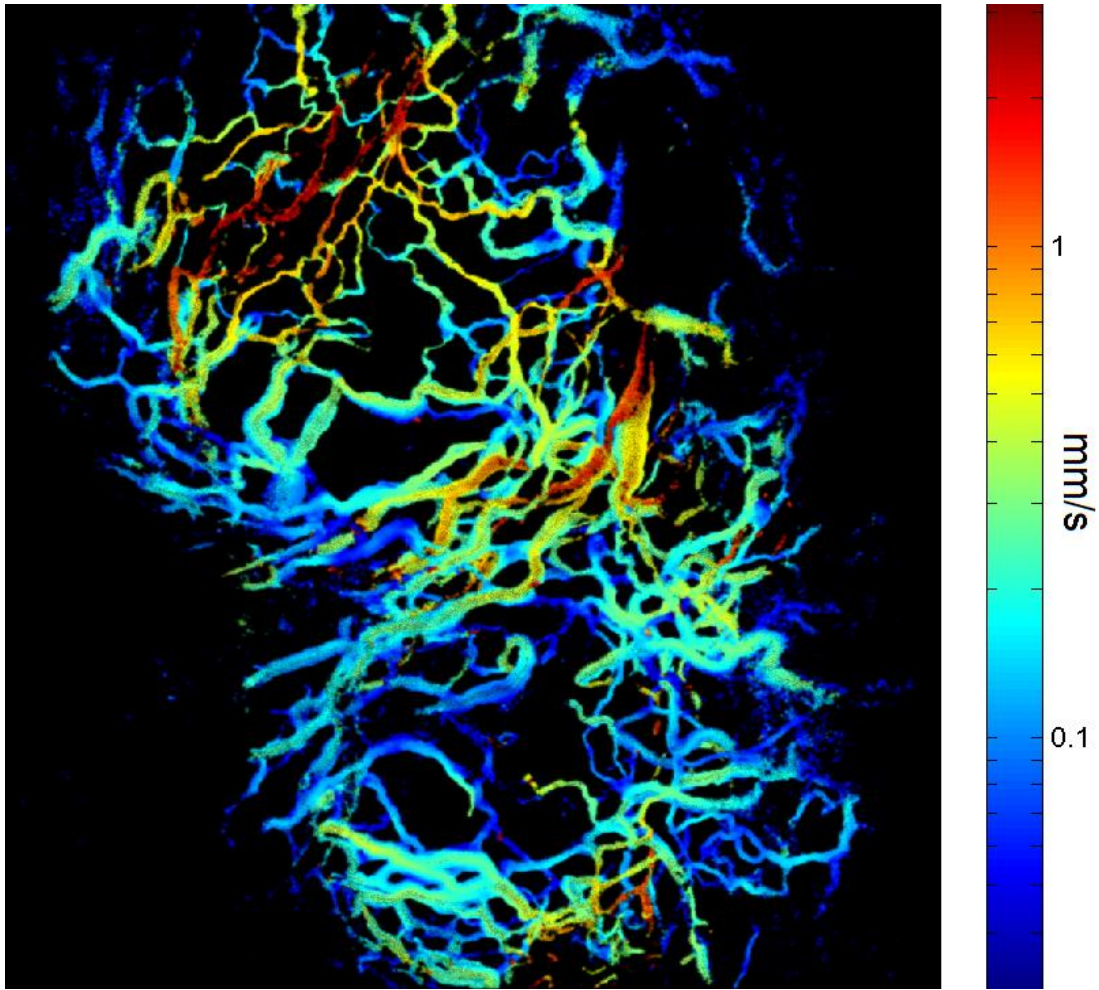
Figure 19: Tumor Blood Speed: Speed (in mm/s) in a dorsal window chamber-grown tumor is represented on a logarithmic color scale. The image represents an area 3.25mm x 3.5mm in the horizontal and vertical directions, respectively.
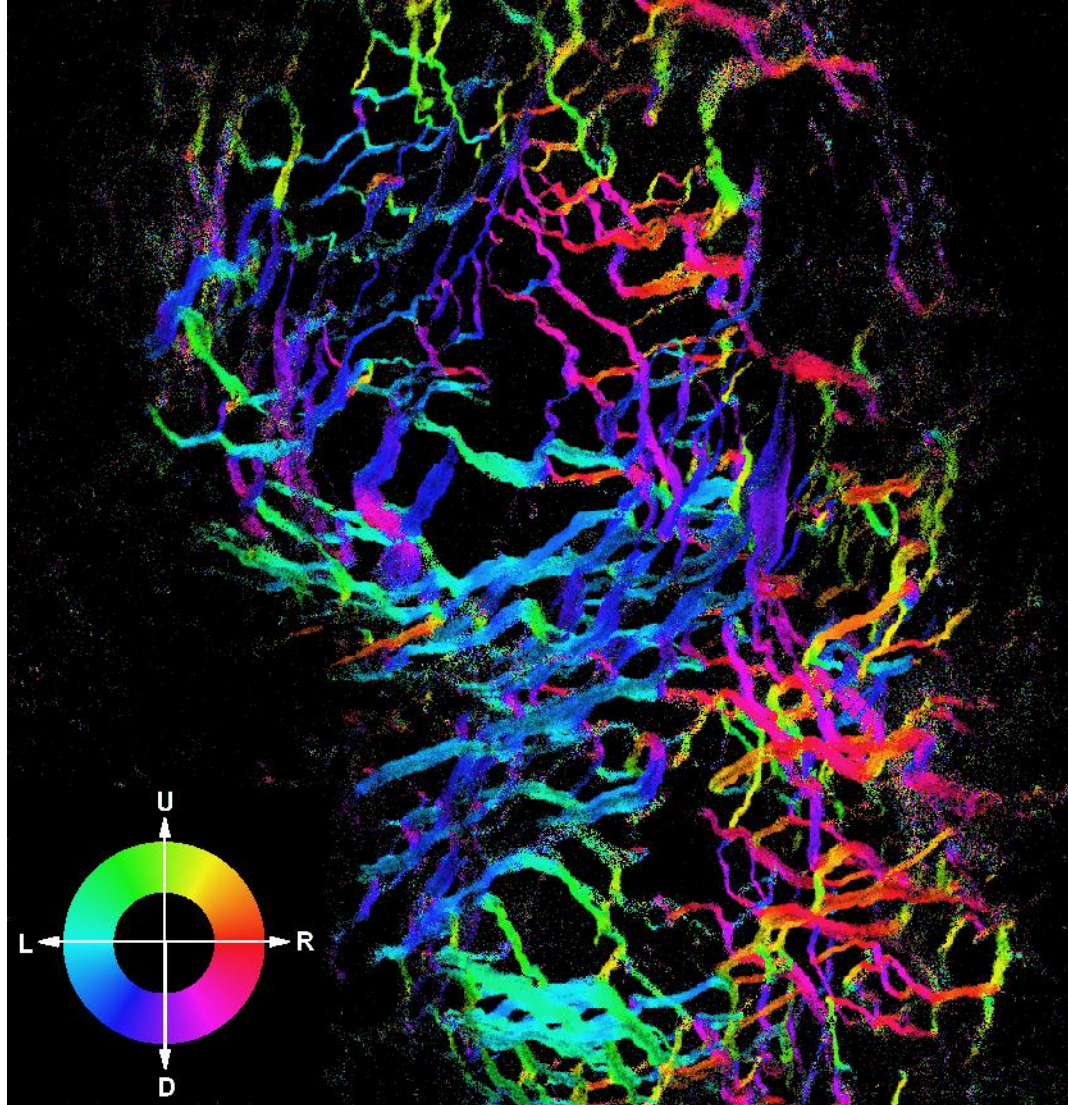
Figure 20: Tumor Blood Direction: Direction (in the same tumor as shown in Figure 19) is indicated by the color wheel (movement to the left appears as cyan, right as red, etc.)

2.2.4 Validation of Velocity Measurements

In order to validate this technique, the algorithm was compared to the dual-slit method. 2×2 binning was used to generate 44 Hz, 64-frame video sequences. Each frame was 696×520 pixels. A total of 37 vessel segments were analyzed between two animals.

The dual-slit technique involves the placement of pairs of windows at upstream and downstream locations on a vessel segment. The intensity values of the pixels within the window are averaged at each time point to obtain a pair of temporal signals. These signals are cross-correlated to find the temporal offset at which the two signals are best correlated. Dual-slit results were constrained to take on frame offsets representing realistic velocity values by limiting the range of temporal offsets to 1-18. By dividing the spatial distance between the two slits by this time delay, velocity values were obtained. The final velocity value for each segment represented the average velocity obtained from twelve independently placed window-pairs. This velocity was compared to twelve algorithm-derived velocity values calculated by averaging the individual values within the region spanning the area between the slit pairs.

The line representing the relationship between mapping algorithm and dual-slit values within common vessel segments was calculated using linear regression analysis. This comparison showed close agreement between the two methods for speeds up to 2 mm/s (Figure 21). The linear model for these data was $y = 1.03x - 0.015$, with $R^2 = 0.96$.

As velocities increased, measurements began to diverge due to increasing imprecision of the dual-slit method (Figure 22). To statistically demonstrate this, we measured the mean and standard deviation of repeated measurements for both techniques. From these, the coefficient of variation was derived. Coefficient of variation values over the 37 analyzed vessel segments were grouped according to method and compared. The mean coefficient of variation value for the mapping algorithm was 0.025, compared to the dual-slit method, which had a mean value of 0.10. The standard errors were 0.0040 and 0.0097 for the mapping algorithm and the dual-slit method, respectively. Statistical analysis of these data using the Wilcoxon rank-sum test demonstrated significantly smaller mean coefficient of variation values for the mapping algorithm ($p < 10^{-10}$).
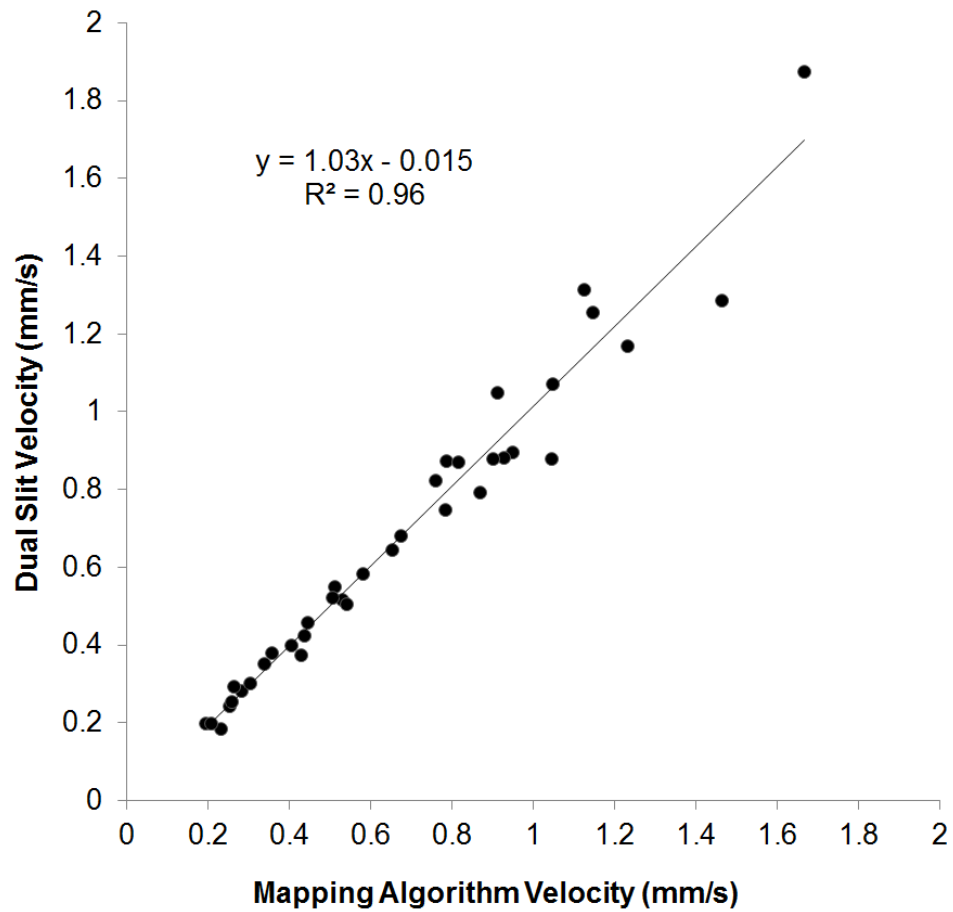
Figure 21: Comparisons of Dual-Slit and Mapping Algorithm Speed Values in Common Vessel Segments: Within common vessel segments, dual-slit calculated velocities were plotted against mapping algorithm derived velocities. Data points represent the mean value of 12 repeated measurements. A total of 37 segments were analyzed. A linear trend was calculated with a slope of 1.03 and a y-intercept of 0.015, indicating good agreement between the two methods. The R^2 value for these data was 0.96.
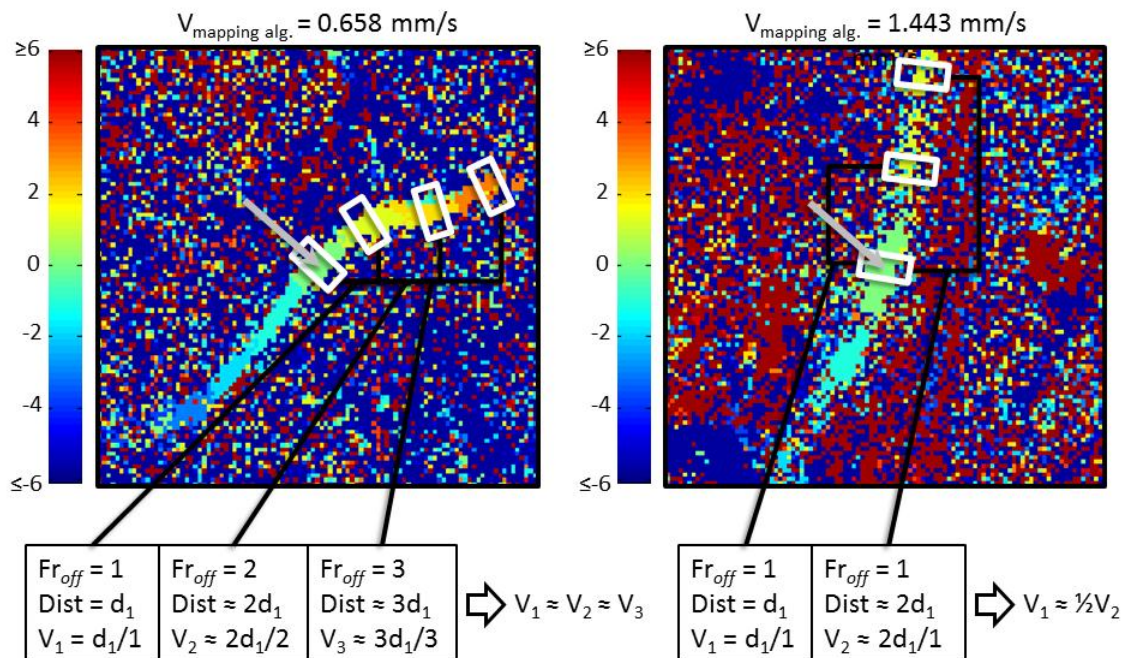
Figure 22: An Illustration of how Inaccuracies Arise in Dual-Slit Estimations of High Velocities: These real-data frame offset maps (as in Figure 18) were derived from two vessels with relatively high and low velocities. The coordinates of interest are indicated by the gray arrow. In the vessel carrying slower moving blood (left), the regions of constant frame offset are small, so dual-slit analysis would produce similar velocity values regardless of the specific window placement (hypothetical examples presented as white boxes). For vessels carrying faster moving blood (right), the regions of constant frame offset become relatively large. Depending on dual-slit window placement, the velocity values can differ greatly due to windows at varying distances measuring the same frame offset. Since the mapping algorithm calculates frame offsets at every pixel in the local region and finds offset centroids, velocity values are not dependent upon arbitrary window placement, thus avoiding this significant source of variability.

2.2.5 Applications of the Mapping Algorithm

The hemodynamic mapping algorithm immediately found broad applicability

due to its automated nature and its ability to produce beautifully detailed, quantitative

maps of blood velocity. A number of our collaborators were eager to apply it to their

research. In every case, the algorithm succeeded in producing quantifiable data,

demonstrating its versatility and utility in a number of model systems. Although its use

is ongoing, a few prominent examples of its application are presented here.

2.2.5.1 Multimodal Imaging Techniques for the Modeling of Vascular Reorganization

Due to the optical simplicity of this technique, we were able to integrate it into

the hyperspectral system without the need for hardware modification; video sequences

were acquired with the same CCD camera that was used to acquire hyperspectral data.

This ability to simultaneously acquire quantitative information from different imaging

modalities may provide insight into how various aspects of the tissue/tumor

microenvironment influence vascular reorganization.

Using methods described in 2.1, total hemoglobin concentration, hemoglobin

oxygen saturation, and vessel diameter data were acquired. Blood flow movies were

concurrently acquired, and speed and direction maps were generated. Knowing

diameters and centerline velocity values allowed for the calculation of shear stress using

standard equations:

$$Shear\ Stress = \frac{4}{\pi} \epsilon \cdot Q \cdot r^{-3}$$

where Q is the mean blood velocity, r is the vessel radius, and

$$\epsilon = 3.2 + 220e^{-1.3D} - 2.44e^{-0.06D^{0.645}}$$

which is an empirically derived term representing the viscosity relative to the plasma

viscosity (where D is the vessel diameter in microns)[232]. The center-line velocity was

assumed to be approximately 1.6 times the mean velocity[233].

The combination of this technique with hyperspectral imaging highlights the

potential applicability of this method within a suite of imaging modalities. Combined

with hemoglobin saturation images, velocity maps may provide useful data regarding

the development of vascular networks and their adaptation to inhomogeneous tissue

oxygenation. Furthermore, the ability to accurately measure blood velocity concurrently

with structural data facilitates the mapping of shear stress, which has been proposed as

a major driver of angio-adaptation[234]. A comprehensive time course of this and other

parameters was collected daily over three days (Figure 23). Data derived from this study

will be used to generate detailed models of vascular remodeling.
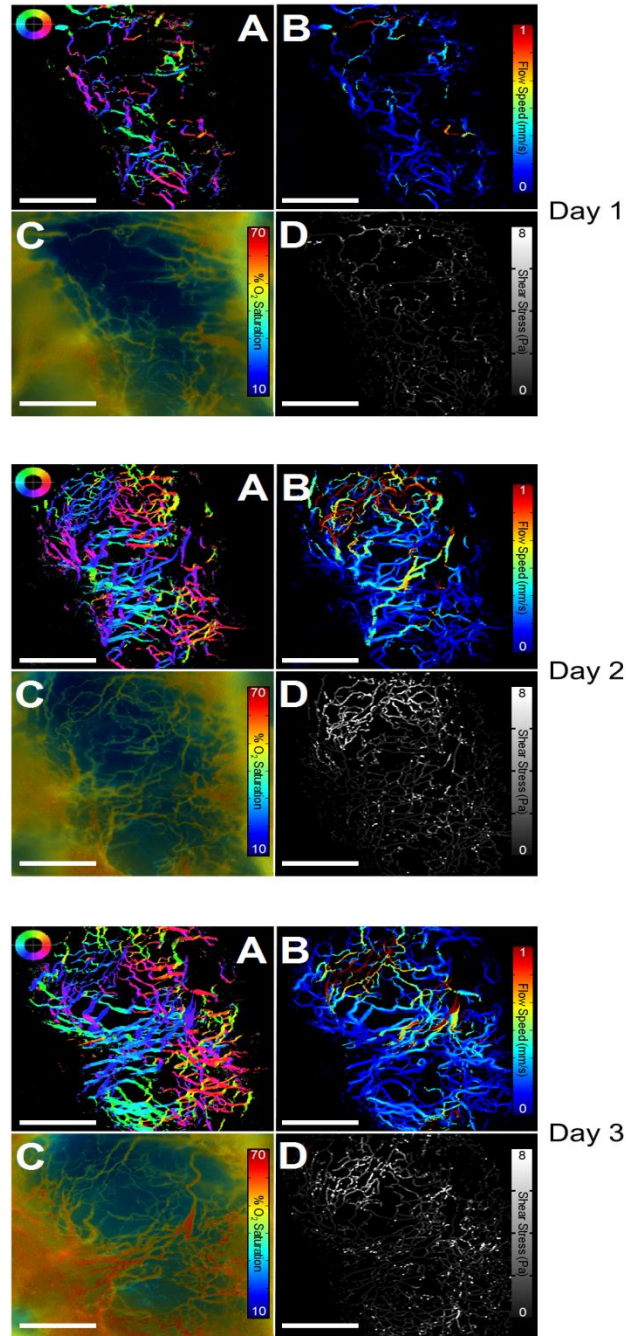
Figure 23: Maps of Hemodynamic Parameters over Three Days: Blood direction (A), speed (B), hemoglobin oxygen saturation (C), and shear stress were calculated from a 4T1 tumor grown in a dorsal skin-fold window chamber. The scale bars are 500μm.

2.2.5.2 Mapping Blood Velocity in the Pulmonary Window Model

To test the mapping algorithm under different conditions, we calculated blood speed and direction in a newly developed pulmonary window chamber model. The surgical procedure for window placement involves the exposure of the rat lung for optical observation[235]. Using fluorescently labeled blood cells excited under epi-illumination, flow within the lung was captured in fluorescence emission video sequences, and the frames were spatially registered as described above.

As opposed to the dorsal window chamber model (which employs transmitted light and uses the optical absorption of hemoglobin as the source of contrast), the pulmonary window chamber technique measures the fluorescence excitation of a small fraction of fluorescently labeled red blood cells in order to track blood movement. Despite these differences in technique, the mapping algorithm produced magnitude and direction maps that correlated well with visually observed velocity features (Figure 24). The ability to visualize flow patterns provided complementary information on the functional physiology of the interrogated vasculature. This is perhaps the first time pulmonary circulation has been directly observed and quantified at the level of single capillaries.
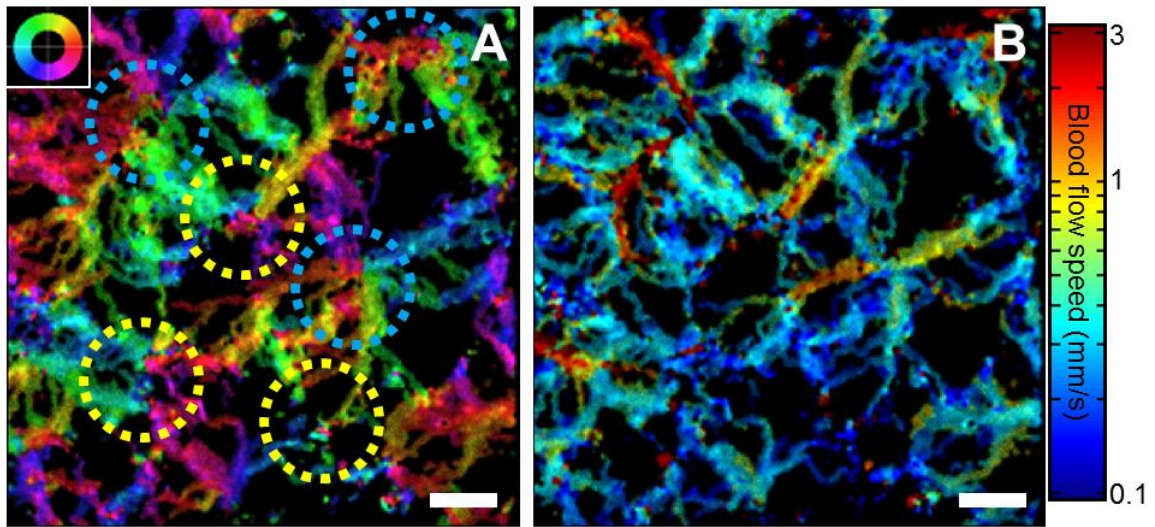
Figure 24: Blood Direction and Speed in the Pulmonary Vasculature: The direction map (A) shows that blood emerges from pulmonary arterioles (yellow circles), traverses the lung surface, and is collected by the pulmonary venules (blue circles). Direction of movement is indicated by the color wheel. Speed (B) is shown on a logarithmic scale to better highlight subtle variations in speed at lower values. The scale bars are 100μm.

2.2.5.3 Observations of Hemodynamics after Cortical Electro-Stimulation

A further test of this algorithm involved the mapping of velocity parameters in the pial vessels of the non-human primate brain. Since these vessels feed directly into and out of the cortex and have been observed to modulate blood flow in response to neural stimulation, they provided an easily accessible indicator of local changes in brain activity.

A small window was surgically established to facilitate optical observation of the outermost layers of intracranial tissues[236]. The vascular network associated with the pia mater was clearly visible under epi-illumination, and movement of blood through these

vessels was captured with a high frame rate camera. When electrodes were used to electrically stimulate the underlying cortex, the alterations in flow in the associated pial vessels were visually apparent.

The processing of these video data was complicated by the presence of significant cardiac and respiratory-associated movement in the video images. Relatively small frame sizes meant a registration algorithm that employed sub-pixel shifts was needed for accurate alignment across frames. This was achieved through the interpolation-based up-sampling of images. Frame registration was performed using the linear-shifting method described in 2.2.1. The image sequence was then down-sampled back to the original resolution. The mapping algorithm processed the registered sequence in 64 frame clusters, each cluster separated by 4 frames. The full sequence of images spanned 8600 frames over 56 seconds, and each frame was 204×49 pixels.

Based on concurrent EEG measurements, the observed sequence was subdivided into periods representing baseline activity, stimulation, after-discharge, and recovery. Using the mapping algorithm, a dynamic blood velocity movie was generated which illustrates the vascular effects of electro-stimulation. Maps at select time points show a profound alteration in blood velocity beginning in the after-discharge period and rising during vasodilation of the major supplying arteriole (Figure 25).

Spatially averaged speed in a downstream venule was also plotted as a function of time using values derived from both the mapping algorithm and the dual-slit method. The dual-slit method used 64 frame clusters, each cluster separated by 100 frames. The velocity values represent the average of 10 calculations using slit pairs which remained constant throughout the time course. Results from these two methods were each interpolated to produce 8600 velocity values.

The sequence of velocity calculations that were derived from the mapping algorithm were statistically tested for correlation with dual-slit values. Correlations coefficients (ρ) and p -values were calculated using the Pearson product-moment method for linear relationships. These tests showed a statistically significant correlation between dual-slit and mapping algorithm values ($\rho = 0.98 / p < 10^{-10}$). Velocity changes estimated by both the mapping algorithm and the dual-slit method correlated also correlated with changes in the diameter of the supplying arteriole ($\rho = 0.89 / p < 10^{-10}$ and $\rho = 0.86 / p < 10^{-10}$, respectively, as calculated from Spearman's method for non-linear relationships).

Speed in the venule maintained a mean value more than twice the baseline average during the recovery period ($\bar{v}_{baseline} = 0.44 \frac{mm}{s}$, $\bar{v}_{recovery} = 1.0 \frac{mm}{s}$, and $p < 10^{-10}$, from a two-sample t-test). These results suggest that pial blood velocity is sensitive to neural activity.

Taken together, these data demonstrate the mapping algorithms utility in measuring temporal changes in velocity. It allows for the analysis of systems in which changing blood flow patterns indicate functional or physiological changes that cannot be directly observed. In this case, we were able to quantify significant changes in venule blood velocity after neural stimulation that correlated well with changes in the diameter of a feeding arteriole. High temporal resolution velocity sequences allowed us to identify the episodes of after-discharge and subsequent recovery as the periods of initiation of vasodilation and largest increases in speed, respectively. These effects are mapped and quantified here for the first time in the primate brain. Due to the sheer quantity of data to analyze, these results would not have been achievable if not for the automated aspect of this technique.
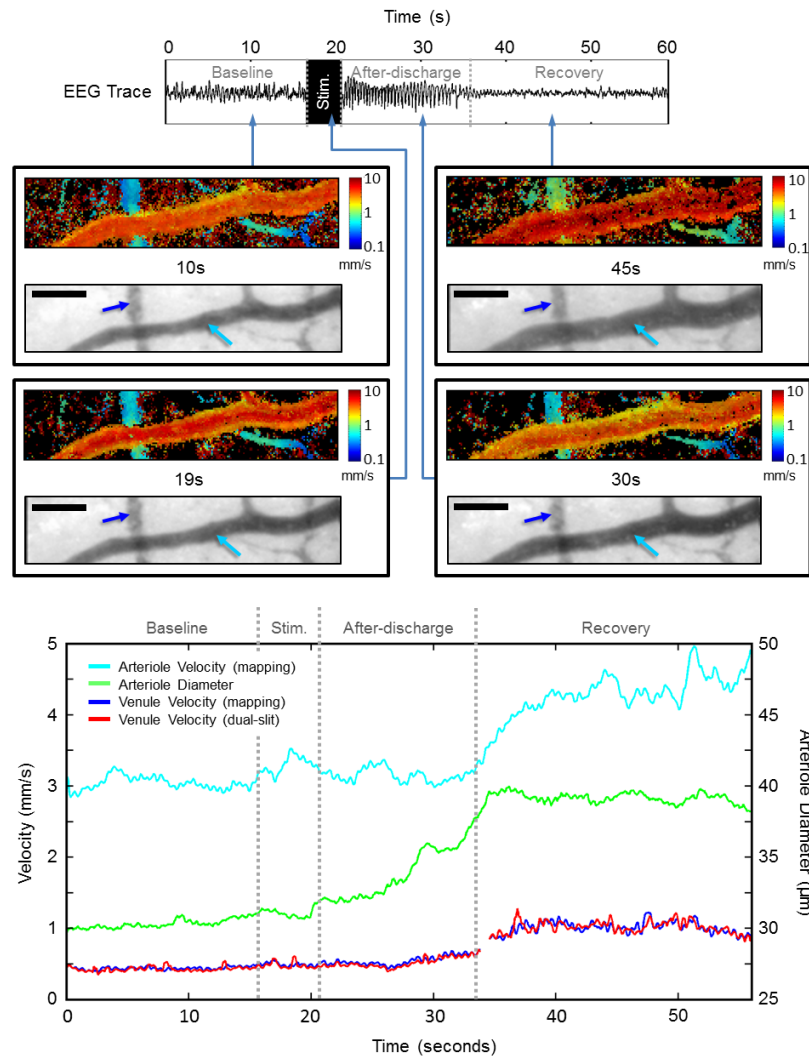
Figure 25: Response to Brain Electro-Stimulation in Pial Venules and Arterioles:
Velocity is mapped (on a log scale) for a portion of the electro-stimulated pial network at
a number of time points (top). At 10 and 19 seconds (representing the network prior to
and during stimulation) the feeding arteriole maintains a fairly constant velocity and
vessel diameter. By 30 seconds (the after-discharge period), the arteriole begins to dilate.
At 45 seconds the arteriole has increased in diameter by nearly 33%, and velocities in the
mapped network have correspondingly increased. Diameter and blood velocity are
plotted for the supplying arteriole (light blue arrow), along with dual-list and mapping
algorithm velocities in a down-stream venule (dark blue arrow) (bottom). The gap at
approximately 34 seconds corresponds to a brief period of motion artifacts. Venule
velocity (as calculated by both methods) and arteriole diameter all showed statistical
correlation with one another. Scale bars are 100 μm.

3. Aim 2: Investigation of Tumor Radiation Response Using Optical Methods

3.1 Clinical Relevance

Spatial fractionation of radiation dose is currently being explored in pre-clinical and clinical studies (see 1.3.2). These treatment modalities are motivated by a reported tumor specific toxicity: clinically high doses are delivered to the tumor, while normal tissue complications are relatively diminished compared to what might be expected from a homogenously distributed dose. The theory behind this effect involves a greater capacity for normal tissue vasculature to repair small volume radiation damage as opposed to tumor-associated vessels.

This theory has yet to be tested in a manner of serial observation, however. Temporally evolving aspects of vascular disruption and subsequent recovery form a critical component of this hypothesis, but cannot be directly measured from *ex vivo* analysis. The vascular contribution to tumor radiation response after spatial fractionation also likely plays a major role in conventional therapies; with a greater capacity for conformal dose distributions, the potential for a marginal tumor miss increases due to a number of factors. These include patient movement, tumor growth and movement, and uncertain tumor margins. The effects of this unintentional sparing of tumor margins (effectively a local spatially fractionated dose distribution) are likewise poorly understood, and may be largely determined by the vascular component.

Thus, a thorough investigation into vascular radiation effects and differential spatial fractionation response would have immediate clinical relevance. Tumor-associated vessels regulate oxygen delivery, and their structural and functional alterations through radiation damage may directly contribute to tumor hypoxia. Since tumor hypoxia has been associated with a poor outcome in a number of clinical studies, the observation of microvascular perturbation may provide critically important insight into the relationship between post-treatment oxygen delivery and associated tumor response. Effects after irradiation may be partially facilitated through the differential expression of HIF-1, as this transcription factor has been shown to be associated with increased angiogenesis, invasiveness, metastasis, and proliferation. HIF-1 is thus a major aspect of detrimental post-treatment alterations in tumor phenotype.

3.2 Study Design

The dorsal skinfold window chamber model was used to serially monitor the vascular effects of radiotherapy. The window chamber model is uniquely capable of offering serial, non-invasive, high-resolution images of the tumor and associated vasculature at optical wavelengths, enabling the observation of temporally evolving aspects of tumor growth and treatment response (including vascular depletion, angiogenesis, and the regulation of HIF-1 expression via fluorescent protein reporters). This is particularly important for a thorough understanding of micro-physiological

radiation effects, as no other *in vivo* model effectively facilitates the tracking of temporal changes at the level of single microvessels.

Through collaboration with a physics group at UNC, a microbeam irradiator was used to treat window chamber-grown tumors. Whole tumor irradiation and mock treatment were used for comparison. The windows were imaged over a week-long time course, and the previously described algorithms were used to extract microenvironmental parameters.

3.2.1 Irradiation of Tumors Grown in the Dorsal Window Chamber

In order to achieve spatially modulated dose distributions, a novel micro-beam system was used to irradiate window chambers tumors in a controlled pattern. Anesthetized mice were placed in the system with their titanium frames immobilized on a heated stage. Animals treated in the microbeam tumor irradiation group were exposed to 160 keV photons passed through a collimator to produce a FWHM 300μm wide beam through the middle of the tumor (Figure 26**Error! Reference source not found.**). Radiation intensity fell off sharply, with areas greater than 300μm from the beam centerline receiving less than 2% of the maximum dose. This beam spanned the width of the window along its centerline, and its track was visualized using a radiation sensitive film glued to the front of the glass coverslip (Figure 27). For the whole tumor irradiation group, radiation was applied without the collimator in place, and the entire window received a homogenous dose while sparing the rest of the animal's body. In

111

both irradiation procedures, the delivered dose was 50Gy. Mock irradiation was also

used as a treatment control.
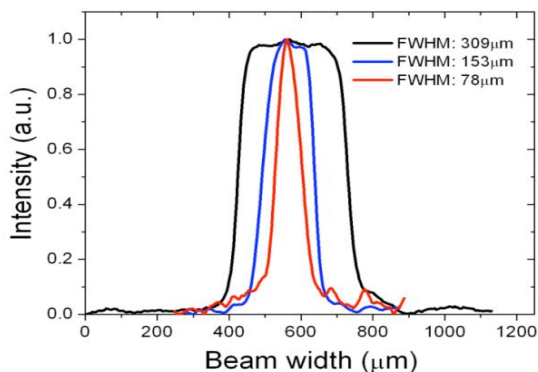
Figure 26: The Microbeam Radiation Profile: The configuration used for this study generated a beam with a profile similar to that shown by the black line. The full-width half-max (FWHM) of the beam was approximately 300μm, and distances greater than 300μm from the beam center received less than 2% of the centerline dose (50Gy).
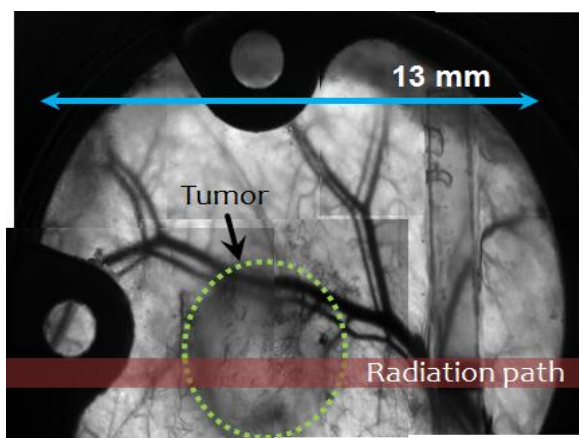
Figure 27: Radiation Deposition in Microbeam-Treated Window Chamber Tumors: A mosaic tiling of 2.5x window chamber images shows the dorsal window chamber-grown tumor and its surrounding normal tissue. These images were collected approximately two hours post treatment using white light trans-illumination. The tumor is outlined in green while the radiation path (estimated from the radiation-sensitive film glued to the coverslip on the right) is highlighted in red.

3.2.2 Window Chamber Imaging Schedules

The methods outlined in Aim 1 were used to optically observe and quantify changes in HIF-1 and vascular response after irradiation. Animals were imaged approximately two hours prior to irradiation, two hours after irradiation, and each day following through seven days post-treatment. For each time point, the windows were imaged using the hyperspectral system described above, with illumination, filtering, and exposure parameters adjusted to capture total hemoglobin/saturation, GFP fluorescence emission, and RFP fluorescence emission. The tumor and surrounding area were imaged at 2.5x magnification for these optical components, and it was from these images that the regions of tumor core, rim, and tumor-associated normal tissue were identified (Figure 28**Error! Reference source not found.**). Video images were also collected in a 24 Hz, 128 frame series at 5x magnification in order to capture the movement of discrete red blood cells as they moved through the vasculature. Finally, after the initial observation of unexpected phenomena highlighted in 3.4.6, images of the entire window were captured in 1.25x image mosaics.
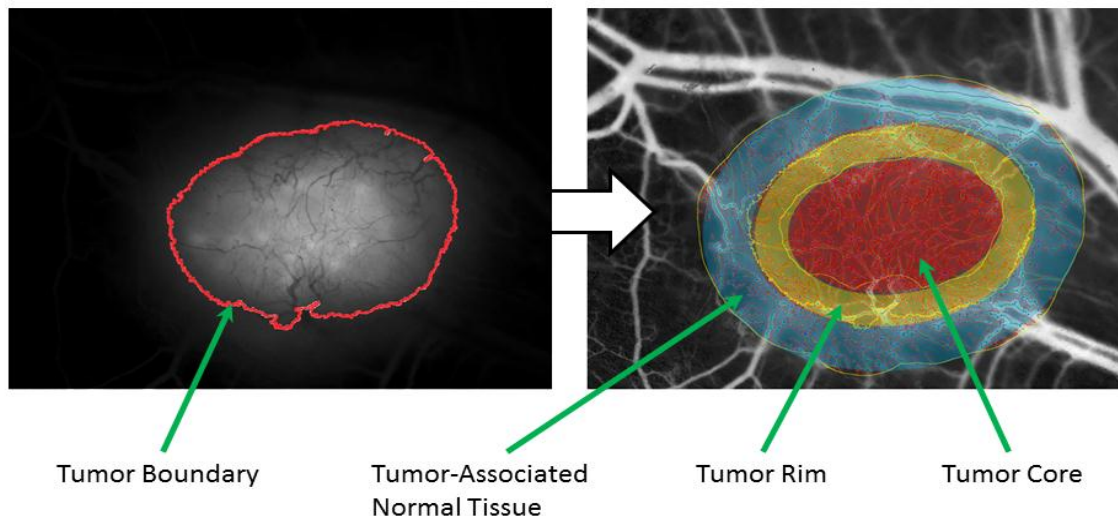
Figure 28: Tumor Regional Demarcation: Processed images of fluorescent reporters (autofluorescence removed) were used to identify tumor boundaries (left). This boundary was then used to segment the tumor into three regions: the tumor-associated normal tissue extends 500μm outward from the tumor boundary, while the tumor rim extends 300μm inwards. The tumor core covers the area inward of the rim. The tumor as a whole consists of the tumor rim plus the tumor core.

3.2.3 Statistical Analysis of Optically Derived Parameters

After processing the acquired data for the extraction of micro-environmental parameters, median values were calculated within each spatial region, at each time point, and for each animal. We then calculated the linear fit of these values over time. The slope of this line represented the rate of change of any particular parameter over the treatment time course. Within each region, slopes were grouped according to treatment type (i.e. microbeam, whole, or mock irradiation, with N=6, 6, and 5, respectively), and statistical analysis using one-way ANOVA was used to detect significant treatment effects. The Tukey-Kramer method was then applied to these results to detect pair-wise

statistical significance between treatment groups. We also calculated the time-averaged

GFP expression in the tumor rim as a percentage of overall expression, and applied the

same statistical tests for significant differences between treatment groups.

3.3 Hypotheses

We hypothesized that spatial fractionation of dose through microbeam

irradiation would elicit distinct effects upon the tumor microvasculature through unique

patterns of disruption. Furthermore, we proposed that HIF-1 signaling in the non-

irradiated tumor would play a primary role in dictating this response. Specifically, we

expected to observe changes in microenvironmental parameters outlined in Table 2.

These anticipated results were based off of our expectation of initial vascular depletion

after radiation treatment (which would persist through the treatment time course in the

whole-tumor irradiation group), followed by vascular recovery in the microbeam group.

Radiation would preferentially deplete the immature, angiogenic vessels, since the

endothelial cells of these vessels proliferate more rapidly and are more prone to short-

term mitotic death. The selective elimination of immature vessels would lead to a

normalization effect, concurrently with post-irradiation reoxygenation, producing a

transient increase in hemoglobin saturation. Vascular length density and vessel

tortuosity would decrease. Median vessel diameter would increase due to the

elimination of the smaller vessels. The drop in flow resistance from the smaller diameter

vessels would result in an increase in blood velocity. Finally, HIF-1 expression would be

upregulated by radiation induced effects (as described in 1.2.1.1). These radiation effects would produce persistent results in the whole-tumor treated group (except for reoxygenation). Conversely, as the normal tissue vasculature recovered after microbeam treatment and repopulated the tumor, the microbeam group would return to the pattern of the control.

Table 2: Anticipated Results of Radiation Treamtments

Anticipated Results:	Whole-Tumor Irradiation	Microbeam Irradiation	Mock Irradiation
Median Hb. Saturation	⬈⬊	⬈⬊	⬊
Vascular Length Density	⬊	⬊⬈	⬈
Tortuosity	⬊	⬊⬈	⬈
Median Vessel Diameter	⬈	⬈⬊	⬊
Median Blood Speed	⬈	⬈⬊	⬊
GFP (HIF-1) Expression	⬈	⬈⬊	⬈

3.4 Results

3.4.1Vascular Structure

None of the treatment groups showed a significant effect in terms of vascular length density or percent vascular coverage (% image area covered by vessels) within the tumor itself (Figure 29A&C). However, the widefield group displayed a significant decrease in both parameters (compared to mock treatment) within the tumor-associated normal tissue (Figure 29B&D).
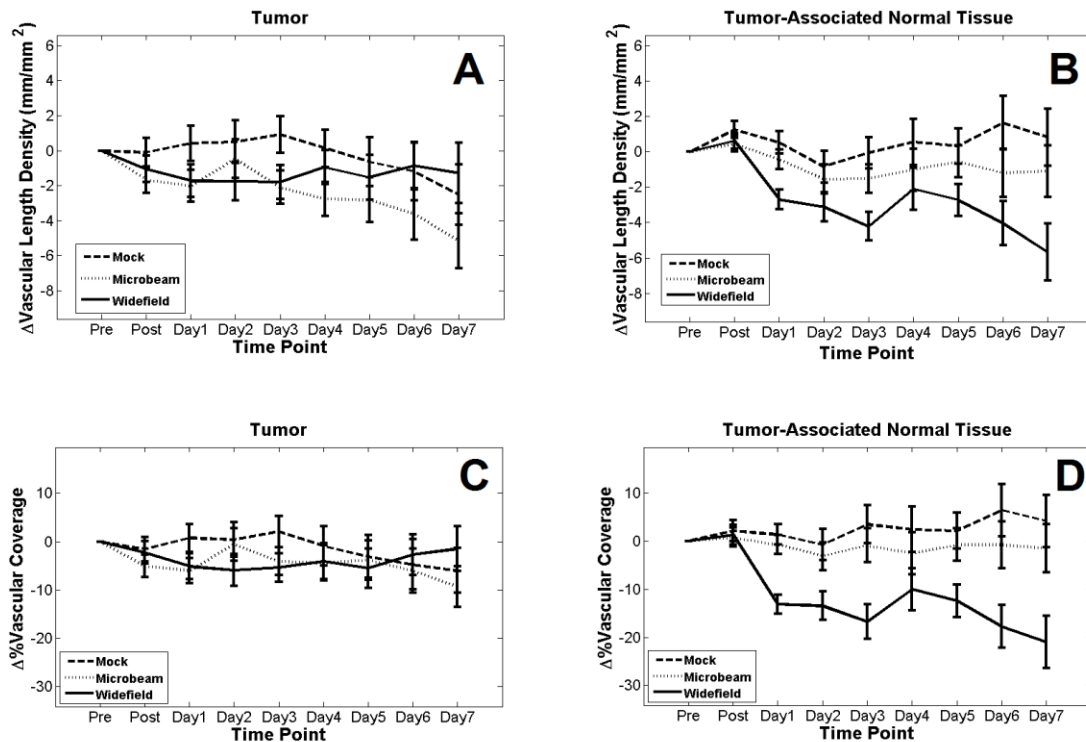
Figure 29: Changes in Vascular Length Density and Vascular Coverage after Treatment: The change in vascular length density compared to pre-treatment baseline is shown for both the tumor (A) and for the tumor-associated normal tissue (B). Similarly, plots of change in percent vascular coverage are shown for the tumor (C) and tumor-associated normal tissue (D).

Upon examination of hemoglobin images, the microbeam group showed very interesting patterns of vascular proliferation. It appeared as though angiogenic vessels were preferentially directed into the post-irradiation beam path (Figure 30). In comparison, neither the widefield nor the mock treated tumors showed a similar effect; in these cases, angiogenesis did occur, but it was generally less profound and showed no particular directional preference (Figure 31).
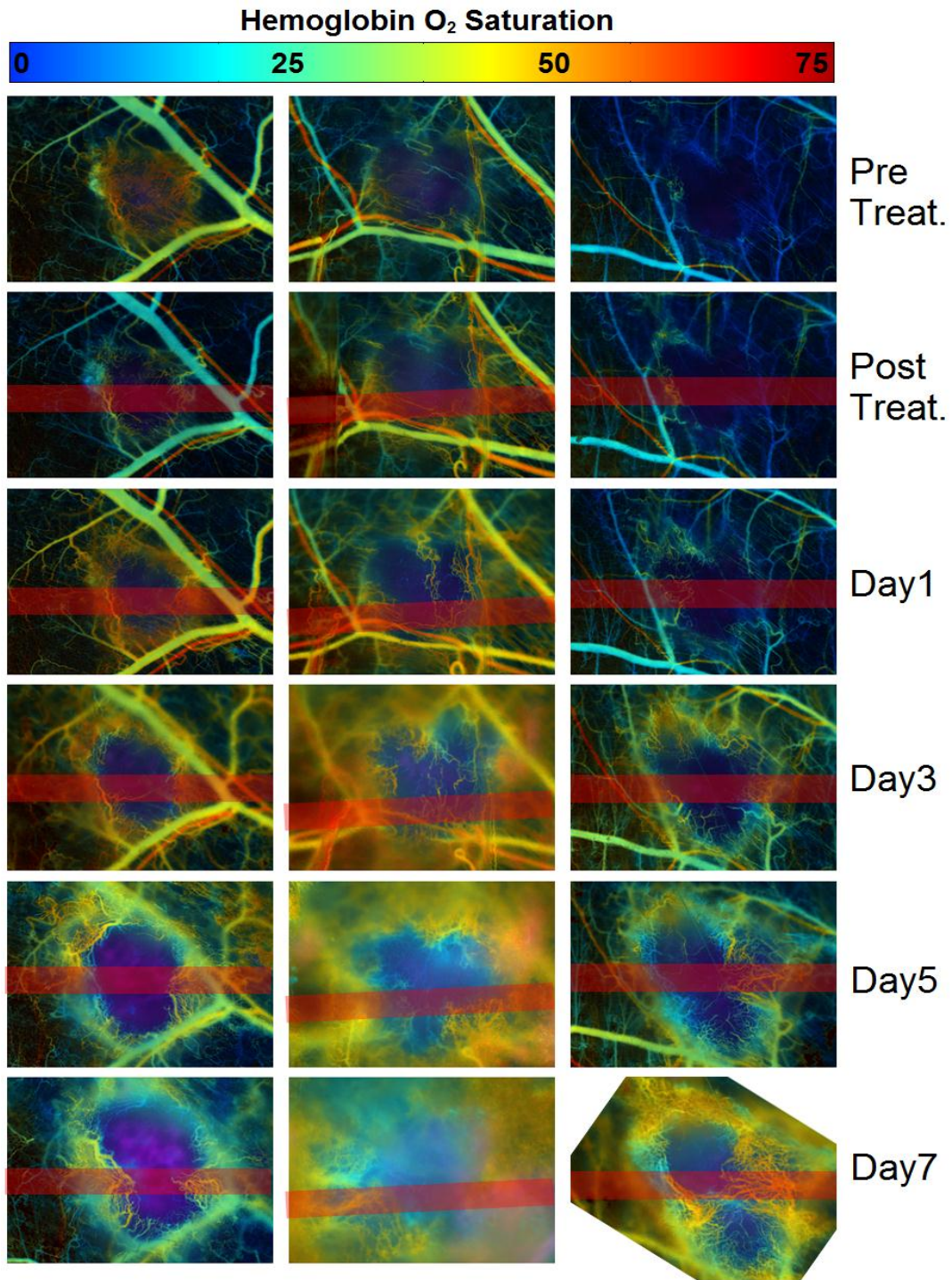
Figure 30: Changes in Hemoglobin Oxygen Saturation and Vascular Structure after Microbeam Treatment: Images of three different microbeam treated tumors showed notable vascular proliferation converging into the radiation beam path (red bar).
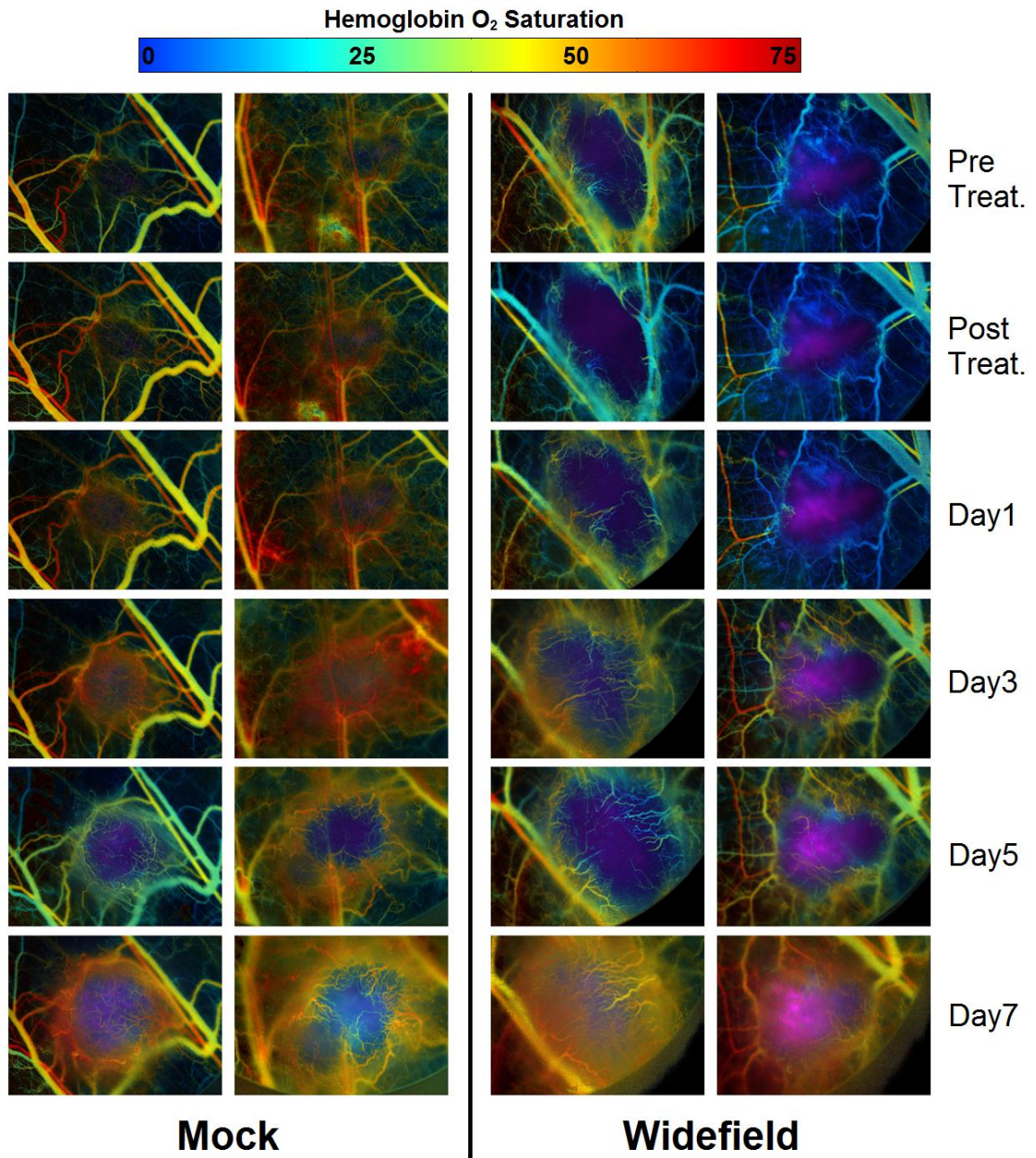
Figure 31: Changes in Hemoglobin Oxygen Saturation and Vascular Structure after Mock and Widefield Treatments: Images of two mock and two widefield irradiated tumors showed no discernible pattern of preferentially directed angiogenesis.

3.4.2 Vascular Function

We next analyzed the window chamber blood flow videos using the mapping algorithm. The derived data indicated no apparent radiation-induced loss of vascular function. We did observe unique patterns of vascular reorganization within the microbeam group, however. Consistent with structural data presented above, vessels tended to proliferate into the region of radiation exposure. This was particularly notable in one tumor, where vessels initially running largely parallel to the beam path on the day of treatment changed their orientation to a more perpendicular orientation in just a few days (Figure 32).
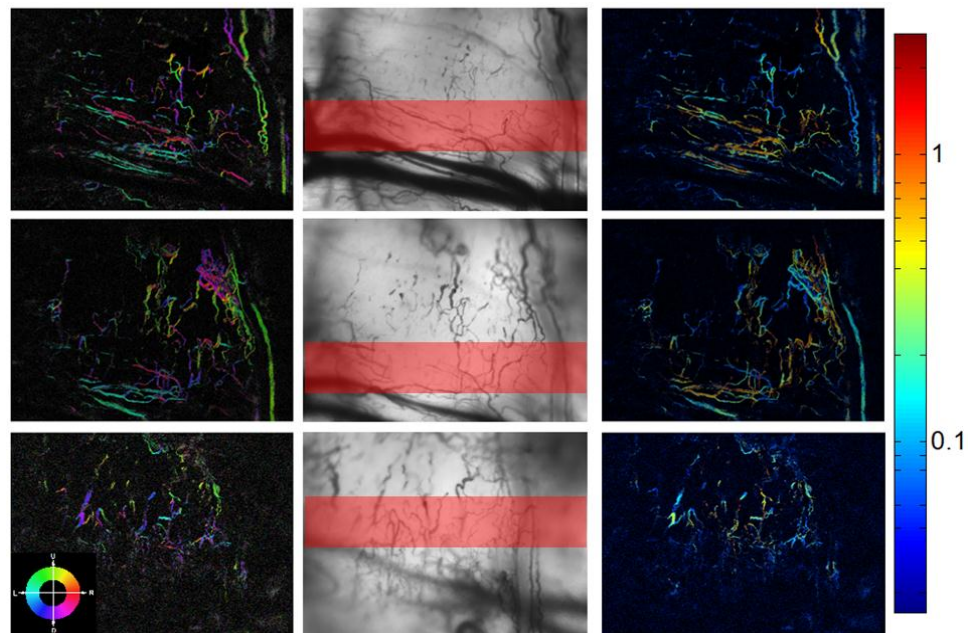
Figure 32: Vascular Changes in Orientation after Microbeam Treatment: Consistent with structural observations, functional velocity maps indicated that after microbeam irradiation, blood flow was redirected perpendicularly and into the path of irradiation. The middle column shows brightfield images with the beam path (Post, Day1, Day2). Also shown are direction maps (left) and velocity maps (right).

3.4.3 Spatial and Temporal Patterns of HIF-1 Expression

Our hypothesis that HIF-1 would play a prominent role in vascular recovery was partially validated. Lacking evidence of any profound vascular disruption, it would be inaccurate to say that this hypothesis was strictly correct. However, patterns of HIF-1 expression after radiation treatment indicated a role in post-treatment vascular remodeling, among other factors discussed in 3.4.5.

Plots of HIF-1 reporting GFP expression (Figure 33A) showed that the fluorescent reporter signal consistently rose throughout the time course in the mock and microbeam treatment groups. On the other hand, this initial rise was followed by signal decay within the widefield group. To determine whether this effect were strictly due to changes in HIF-1 expression, we also measured changes in RFP expression (Figure 33B). Since RFP serves as a constitutive reporter, the expression of this protein should serve as a concurrent indicator of the number of viable cells in the tumor. When cell viability was controlled for by taking the ratio of median GFP:RFP expression, we observed that the microbeam treated group was the only one to display a notable increase in relative GFP expression over the post-treatment time course (Figure 33C). Taking into account the spatial distribution of GFP expression, we were able to show that GFP was expressed in the tumor rim at a higher rate in the microbeam treated group, compared to either mock or widefield irradiation (Figure 33D).
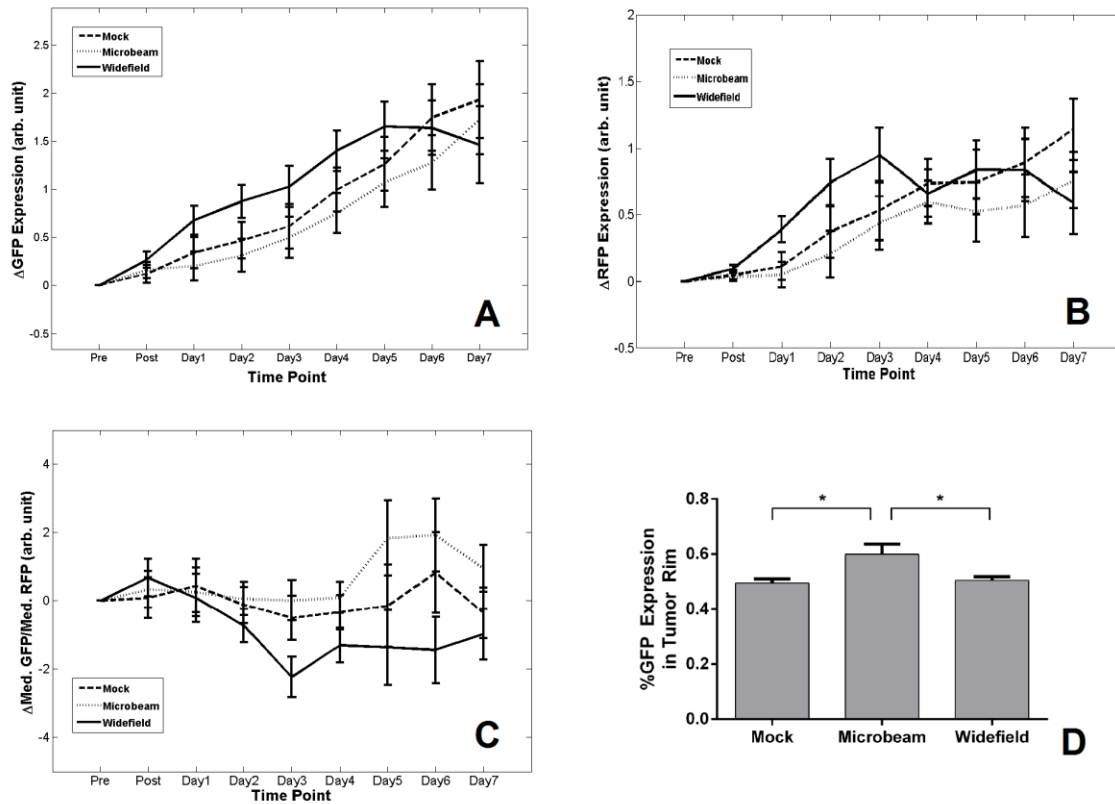
Figure 33: Spatial/Temporal Patterns of HIF-1 Expression: The overall change in GFP expression for the three treatment groups (A) is plotted along with RFP expression (B). The ratio of median GFP:RFP expression is also shown (C). Spatial patterns of expression were analyzed, and it was observed that GFP was expressed at a significantly higher rate in the microbeam tumor rim than in the rim of either the mock or widefield treated tumors (D).

3.4.4 Alterations in Vascular Hemoglobin Concentration

Plots of median vascular hemoglobin concentration showed a notable increase in

the hemoglobin concentration rate of change within the microbeam treated group

(Figure 34). This began on the third day post-treatment. Although the effect was not

noted in the tumor-associated normal tissue, it was prominent in the tumor itself (both within the rim and core)
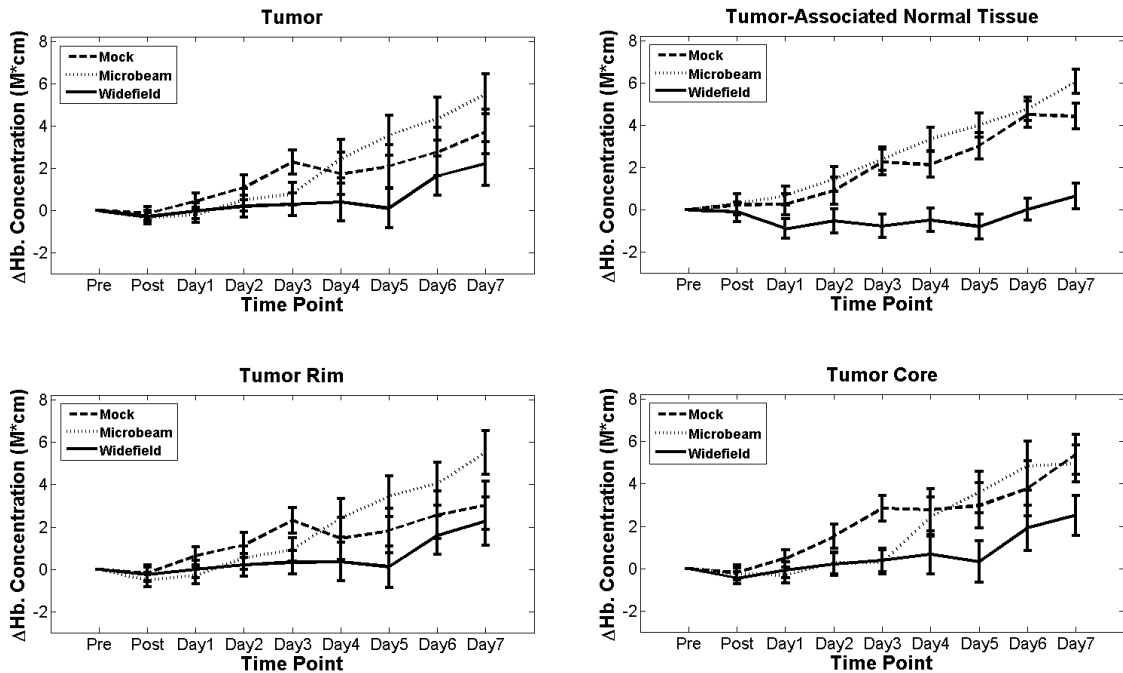
Figure 34: Temporal Changes in Median Vascular Hemoglobin Concentration: Plots of change in vascular hemoglobin concentration (compared to pre-treatment baseline) are shown for the tumor as a whole (top-left), the tumor-associated normal tissue (top-right), and the subdivision of the tumor rim (lower-left) and tumor core (lower-right).

Statistical analysis showed that overall, the rate of change in hemoglobin saturation was only significantly different within the widefield group (compared to either mock or microbeam) (Figure 35A). When the time course was split into two segments (Pretreatment - Day 3 & Day 3 - Day 7), the rate of change in hemoglobin concentration was not significantly different among any groups within the first timeframe (Figure 35B). Within the second time frame, however, the rate of change

within the microbeam group was significantly different from either mock or widefield.

When comparing the change in rate between the two timeframes within each group,

only the microbeam group showed a significant difference.
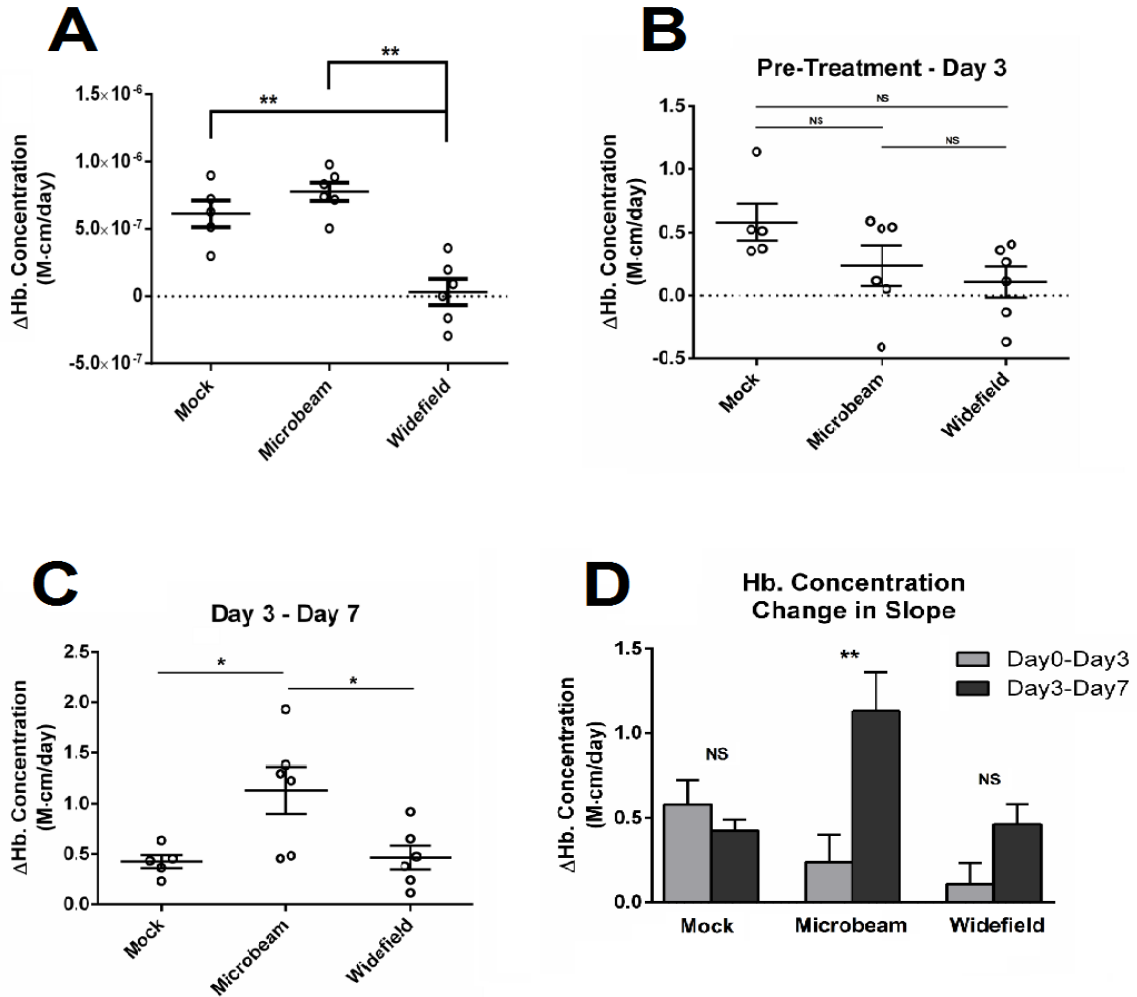
Figure 35: Temporal Changes Median Vascular Hemoglobin Concentration in Split Timeframes: Overall rates of changes in hemoglobin concentration show significant differences only for the widefield group (A). No rates were significantly different between pre-treatment and day 3 (B). This changed over the second half of the time course, where the microbeam group showed a significant effect (C). The change in rate between these two split timeframes was significant only for the microbeam group (D).

3.4.5 Evidence of Tumor Cell Death (Whole Tumor Irradiation)

Concurrent with the drop in fluorescent reporter expression after widefield treatment, we observed a significant increase in hemoglobin oxygen saturation (Figure 36). These combined effects lend support to our conclusion that widefield radiation induced widespread cell death. As cells begin to die off, overall oxygen consumption within the tumor drops, leading to longer longitudinal oxygen gradients as cells take up less oxygen within the blood (see section 1.2.1). This results in an increase in median hemoglobin oxygen saturation, as observed here.
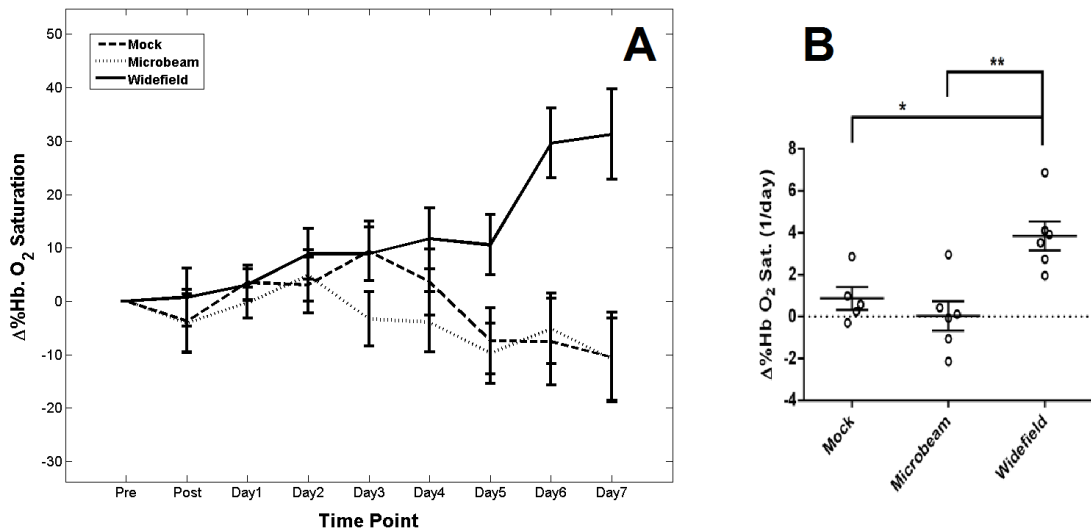
Figure 36: Changes in Hemoglobin O₂ Saturation After Treatment: Widefield irradiated tumors showed a dramatic increase in hemoglobin oxygen saturation by the sixth day post irradiation. The difference in overall rate of change between widefield and the other two treatment groups was significant.

3.4.6 Evidence of Tumor Cell Migration (Microbeam Treatment)

One of the unanticipated effects of microbeam treatment was the formation of secondary clusters of tumor cell growth away from the primary tumor (Figure 37). This was observed as early as three days post-treatment. Areas of notable angiogenesis would begin to form at locations within the window remote from the primary tumor. RFP images showed that this angiogenic effect was associated with the presence of a tumor cells at this location. This effect was not observed in the mock treatment group (Figure 38). Neither was it observed in the widefield group, but since the widefield treatments were completed prior to the first observation of this effect (due to the time and complexity of installing the beam collimator and recalibrating the system), whole window images were not collected.

Hb. Saturation   **RFP**
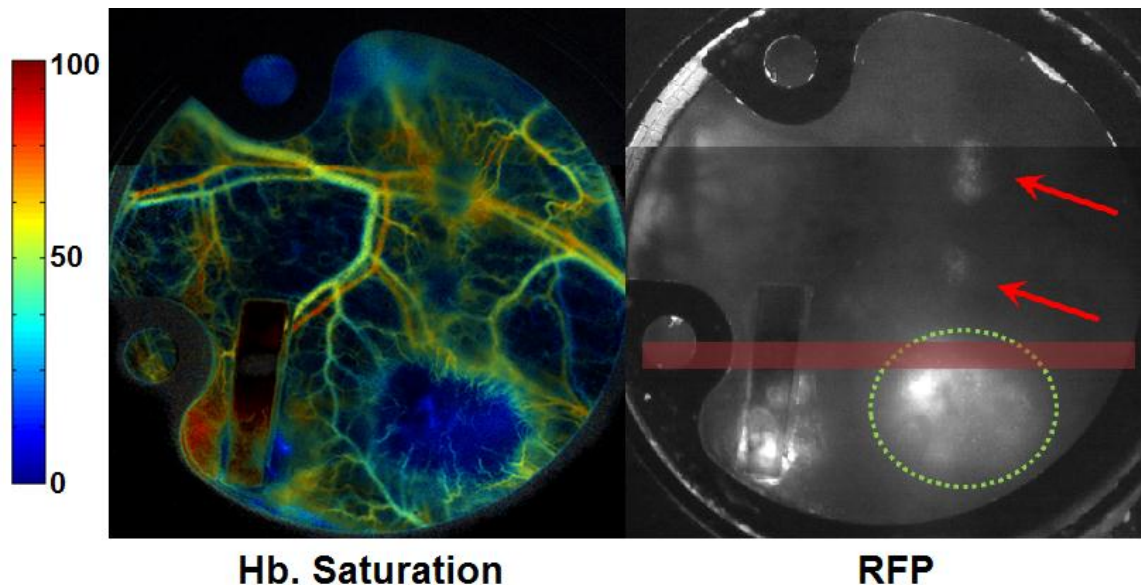
Figure 37: The Formation of Secondary Tumor Cell Clusters after Microbeam Treatment: A whole-window hemoglobin saturation image appears to the left, showing areas of angiogenesis upwards of the primary tumor (at approximately the five o'clock position). The RFP image of the same field of view (right) clearly show the growth of secondary clusters of tumor cells at these areas of angiogenesis (red arrows). The primary tumor is indicated by the green circle, and the microbeam path running through it visualized as the red translucent band. This path was determined from the radiation sensitive film glued to the window's coverslip (to the left of the tumor).

Despite the frequent use of the 4T1 reporter cell line within our lab, this phenomenon was not noted in prior studies, leading us to speculate that the formation of these clusters was a microbeam-induced effect. In order to demonstrate that these clusters were the result of tumor migration (rather than the accidental seeding of cells at these locations during surgery), we imaged the tumor at high resolution using confocal microscopy. At 10x maginification, we observed bridges of tumor cells that spanned the gap between these two clusters (Figure 39). Furthermore, during a 90 minute imaging

session, these bridge cells displayed coordinated mobility. These data imply that

microbeam therapy had the effect of activating cellular motility mechanics—an effect we

speculate is the result of radiation-induced epithelial to mesenchymal transition.
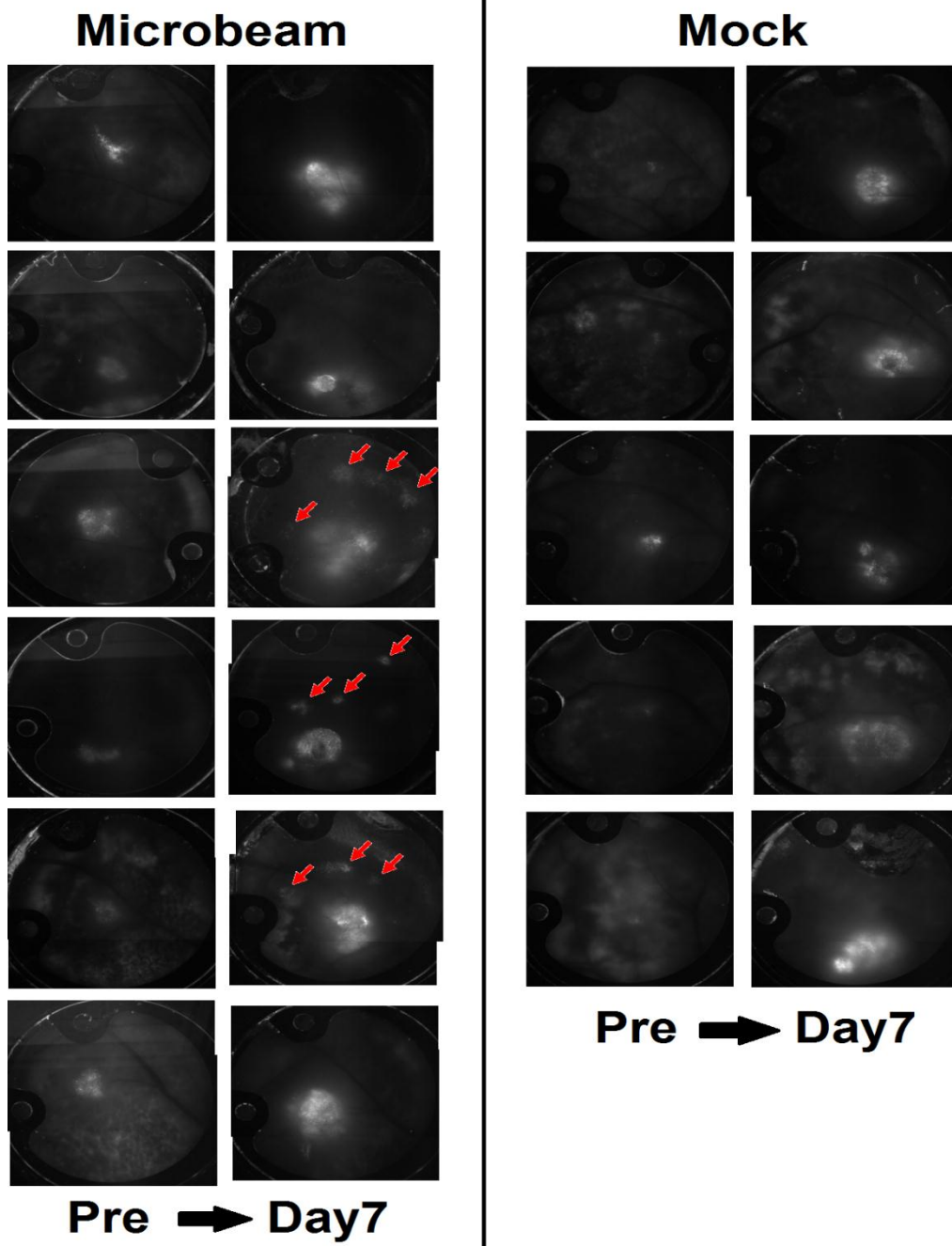
Figure 38: Secondary cluster formation was observed in the microbeam group, but not in the mock treated group: Whole-window pretreatment and day 7 images are shown for each animal. The red arrows indicate areas of secondary cluster formation.
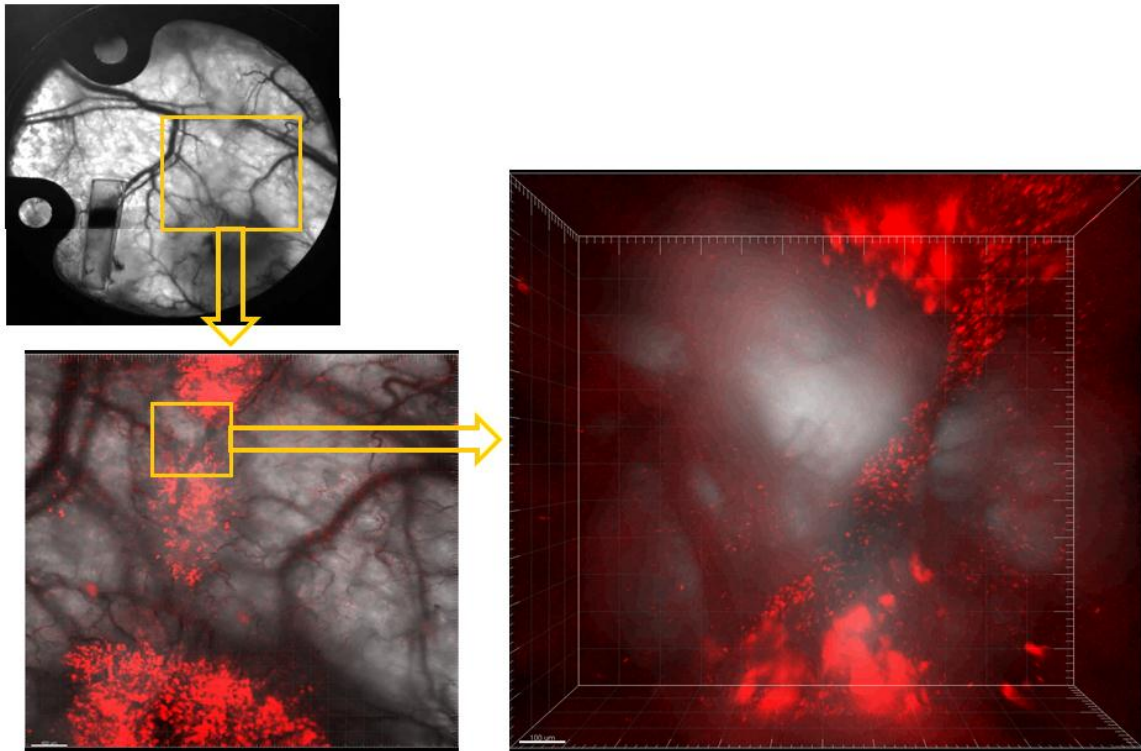
Figure 39: Tumor Cells Form a Bridge Between Areas of Secondary Growth: A whole-window image of a microbeam-treated tumor and surrounding tissue appears in the upper left. When this image is magnified and RFP expression is overlaid, areas of angiogenesis and secondary tumor growth can be observed in the two nodules upwards of the primary tumor. The high resolution detection of RFP expressing tumor cells using confocal microscopy showed that within the region spanning the gap between these two secondary clusters, a bridge of semi-motile tumor cells could be observed.

3.5 Discussion of Findings

The results presented here do not support our hypothesis that high dose

microbeam radiation produces widespread vascular disruption. No direct evidence of

vessel depletion or loss of functionality was observed. Rather, proliferation of the

vasculature within the tumor-associated normal tissue along the radiation path

suggested a robust angiogenic response to radiation in the microbeam treatment group. Widefield treatment, on the other hand, did show a drop in vascular length density and percent vascular coverage and after treatment.

Vascular functionality likewise remained unaltered in the microbeam group, as assessed through maps of blood velocity. Furthermore, we observed no significant alteration in hemoglobin oxygen saturation after treatment, suggesting that tumor oxygenation remained stable throughout the time course. Unique patterns of vascular remodeling were highlighted in the direction maps, however. Here we observed that blood flow was redirected into the irradiated beam area. Thus, both functional and structural analyses of the vasculature indicate that microbeam therapy increases the blood supply to irradiated tissue.

This vascular adaptation to localized radiation may be facilitated through HIF-1 expression, as we proposed. Notably, spatial analysis showed that the primary area of HIF-1 expression was not within the directly irradiated tumor, however. A relatively high amount of HIF-1 activity was shown to occur in the tumor rim, which would have received relatively less radiation exposure than the tumor core. We speculate that this response may have been due to radiation bystander signaling.

The radiation bystander process is thought to be at least partially mediated through the radiation-induced production of free radicals[237,238]. Damage to mitochondria may further potentiate this oxidative stress[239]. The production of the diffusible and long-

lived radicals hydrogen peroxide and nitric oxide have been prominently implicated in the bystander response[240]. Bystander-affected cells have been shown to increase the production of both of these radicals. As discussed in 1.2.1.1, both hydrogen peroxide and nitric oxide have been shown to stabilize HIF-1 in the presence of oxygen[49,53]. Thus, the observation of increased HIF-1 expression in the rim, despite a lack of any direct stimulation, suggests bystander singling is active here. This is likely one of the causes of vascular stimulation after treatment.

The sharp increase in hemoglobin concentration beginning on the third day post treatment further implicates bystander-induced HIF-1 upregulation in the post-microbeam irradiation response. HIF-1 controlled expression of VEGF most obviously causes angiogenesis (as clearly seen here), but a secondary effect of VEGF secretion is an increase in vascular permeability. With an increase vascular permeability, plasma leakage will cause hematocrit to rise, possibly explaining the post-irradiation rise in hemoglobin concentration within the tumor.

These observations of post-treatment HIF-1 induction (likely initiated through bystander mechanisms) may explain the observation of tumor cell migration after therapy. Radiation is known to potentiate EMT. However, it is not clear how indirect effects through bystander signaling may modulate this process. Data presented here indicate that bystander effects may *not only* be capable of transferring radiation-lethality

(as is commonly reported), but may also transfer radiation-induced alterations in phenotype.

3.6 A Proposed Model of Microbeam Radiation Response

The disparity in response between microbeam and widefield irradiation may be due to more complete cell death in the widefield group. Evidence for this is seen in the rise in hemoglobin oxygen saturation in the last days of the study, suggesting oxygen consumption had decreased. This is consistent with the known post-treatment reoxygenation effect, where oxygenated cells are preferentially killed by radiation, freeing up oxygen for diffusion into formerly hypoxic tumor regions[24]. With increased dose, however, even hypoxic cells may be directly killed, leading to even more profound increases in tumor oxygen content.

The reoxygenation effect has also been shown to be been spatially and temporally linked with post-treatment HIF-1 induction[49]. We observed a dissimilar trend here, however. As tumor oxygenation increased, HIF-1 decayed. We speculated that this is, once again, due to the very high dose the tumor received, and the lack of viable cells to induce GFP production. The concurrent drop in RFP expression confirmed this. When GFP expression was normalized to RFP expression, only the microbeam group showed any relative increase in GFP. This suggests that for the other groups, changes in GFP were primarily a product of tumor growth (followed by cellular death in the widefield group).

133

The data presented here challenge the model of endothelial cell death as the major determinant of radiation response. Rather, our results suggest that in terms of vascular function, immediate endothelial cell death may be less relevant than post treatment tumor signaling. Within the microbeam group, whatever degree of endothelial cell death was induced did not seem to disrupt the structural or functional characteristics of the vasculature as a whole. Post treatment initiation of a HIF-1 response in the tumor rim may have protected the tumor against vascular depletion through the recruitment of blood vessels from the tumor-associated normal tissue.

The vascular radio-protective effect of HIF-1 presents further problems for the hypothesis that endothelial cell apoptosis is the primary mechanism controlling tumor response to therapy. Since endothelial cell apoptosis is known to peak only a few hours after treatment[195,205], this theory cannot easily explain the protective effect of HIF-1, which is maximally upregulated well after the period of apoptotic response. Rather, the data presented here provide evidence that tumor-mediated vascular protection through intercellular signaling (likely through bystander mechanisms) is the primary determinant of treatment outcome. Furthermore, we have shown that the induction of HIF-1 may also play a lasting role in diminishing the efficacy of radiation treatment by driving invasion and metastasis, possibly through EMT.

These observations provide evidence of possible detrimental effects after inhomogeneous tumor irradiation through microbeam treatment. However, this

vascular contribution to tumor radiation response may also play a major role in

conventional therapies, such as IMRT, where a marginal miss (effectively a local

spatially fractionated dose distribution) may produce similar effects. The unintentional

sparing of tumor margins is poorly understood, and may be largely determined by the

vascular component, as seen here.

It is important to note, however, that the spatial modulation of dose in this study

is simplistic compared to those typically employed in most spatial fractionation

techniques. Intercellular signaling factors may produce variable effects dependent upon

geometry/dose-sensitive diffusion gradients. Thus, evidence presented here may not

necessarily be applicable to spatial fractionation techniques in general. However, these

data are cause for concern regarding the long-term implications of unknown (as in the

case of marginal misses) or poorly investigated spatial heterogeneities in radiation dose.

4. Future Directions

The research presented here has produced efficient and accurate algorithms for the quantification of vascular parameters (Aim 1) and fascinating insight into the biological effects of radiation (Aim 2). As such, we believe that these two aspects of the presented research will provide fertile ground for continuing studies. We envision a number of possible future directions in which to expand this work.

4.1 Aim 1: Optical Data Processing Techniques

4.1.1 Structural analysis

The algorithm we have developed for the analysis of vascular structure in window chamber studies has yielded accurate results compared to the current standard. This is a significant achievement, as prior approaches to quantification of vascular parameters in tumors relied on manual traces of vessel centerlines—a time-consuming process highly prone to selection bias. Furthermore, the presented algorithm overcomes many of the limitations of prior automated techniques which rely on detection geometries associated with morphologically normal vessels. This renders these techniques poor discriminators of tortuous, irregular vessels shapes associated with tumor angiogenesis.

As a test of the versatility of this algorithm, we intend to apply the method to clinical images. In collaboration with Dr. Victoria Seewaldt, we will examine human breast cancer MRI data. The ultimate goal of this application is the identification of

areas of irregular vascular structure. Since the distinction between nascent tumors and areas of natural tissue heterogeneity can be difficult to distinguish by eye, we hope that this computational technique might serve as useful aid for early clinical diagnosis.

We also propose to apply this method to a newly developed system for imaging blood supply to tumor nodules using a novel liposomal contrast agent[241]. This method was developed at Duke, and allows for the generation of high contrast 3-D vessel maps using computed tomography. The ability to generate high resolution structural volumes in small animal studies using micro-CT systems will provide for a better understanding of changes in 3-D structural morphology as tumors grow and in response to treatment. Furthermore, the liposomal nature of this agent may one day facilitate serial imaging of drug delivery dynamics through the encapsulation of chemotherapies.

4.1.2 Functional Analysis

The mapping algorithm has already proven a useful tool in other biological imaging systems. In addition to the studies outlined in 2.2.5, the mapping algorithm is currently being applied in a number of additional rodent studies. The rat pulmonary window has been used to image blood flow to pulmonary metastases, while cremaster muscle images have been used to examine the hemodynamic alterations produced by various drugs. Within murine models, blood velocity mapping has been applied to the liver, brain tumors, and various studies which apply perturbations to dorsal window chamber tumors.

137

In addition to studies of adult normal or tumor vasculature, it would be fascinating to apply this technique to studies of embryogenesis. Vasculogenesis is already studied regularly in chick egg models. The ability to measure not just structural, but also functional development of the embryonic vasculature would provide invaluable insight into the *de novo* construction of the cardiovascular system.

In addition to expanding the algorithm's application to various other animal models, we hope to improve the efficiency of the code itself and perhaps explore applications within 3-D imaging modalities. As the code is currently run in MATLAB, conversion to a more efficient language, or perhaps even incorporation into a microprocessor, will dramatically increase the speed at which data can be processed. Our ultimate goal is to see the algorithm applied in real time to track dynamic changes in velocity with a high degree of temporal resolution. The incorporation of real-time data output into a turnkey imaging system would be phenomenal accomplishment. Such a system would provide invaluable insight into the hemodynamics of various systems without the need for fragile imaging hardware or complicated post-processing software.

Three-dimensional blood movement patterns can potentially be achieved through analysis of raw data acquired from spectroscopy-based techniques, such as OCT. The primary challenge would be in acquiring volumetric data a high enough rate and sensitivity to be able to distinguish coherent temporal signals. By implementing a

series of acquisitions of small volumes, however, it may be possible to serially acquire voxel blocks to build up a larger volume structure. The ability to analyze microcirculation in three dimensions would provide insight into vascular networks not suited for the present algorithm. Particularly, the ability to measure hemodynamics in tumors more than a few days old is problematic for current techniques, as the vasculature remains largely planar only for a short time; the mapping of velocity patterns at later times through three dimensional optical techniques will provide insight into microcirculatory dynamics in more mature (and possibly more hypoxic) tumors.

Photo-acoustic computed tomography may provide another approach to the acquisition of 3-D data. This is a particularly exciting method, as prior work has shown that photo-acoustic CT is additionally capable of imaging metabolic factors[242]. Since the relationship between oxygen/nutrient transport and metabolic activity is a subject of much investigation in cancer research, a single imaging method for linking these two parameters will provide invaluable insight into pre-clinical models of tumor metabolism-linked treatment strategies.

We also hope to one day expand this technique to clinical applications. OCT is already used as an optical imaging technology in ophthalmology for the detection of diseases of the vasculature. The incorporation of velocity mapping into this system will provide further insight into microcirculatory dynamics for the rapid diagnosis of vascular pathologies. Investigation of human brain activity is also a potential clinical

application of this technique. Real-time analysis of blood velocity within the pial vessels

of the cortex may provide information on local brain activity, as shown in 2.2.5.3. This

information would assist neurosurgeons to identify functional brain regions to be

avoided during surgery. Furthermore, such data would provide insight into the basic

details of human brain function. Since patients are sometimes kept conscious during

brain surgeries, changes in blood flow patterns may be correlated with specific sensory

stimulation.

Finally, we believe that the utility of this method is not limited to biological

studies. Any physical systems wherein coherent movement patterns may be observed

are potential applications for the mapping algorithm. These might include satellite

images of regional weather patterns or compilations of automobile traffic data. The

possibilities are vast, and it is our hope that the public presentation of this technique will

enable many more collaborations throughout various disciplines.

4.2 Aim 2: Investigation of Tumor Radiation Response Using Optical Methods

The results of the radiation aspect of this research present a fascinating model of

post radiation response, especially in the case of microbeam treatment. Many of the

underlying mechanisms of these observations remain unknown, however. Future

research will focus on uncovering the mechanistic basis of radiation-induced angiogenic

patterns and tumor migration. Although we have implicated HIF-1 in this response, this

transcription factor influences the expression of a wide number of genes. Therefore,

fundamental work with other *in vitro* and *in vivo* models will help to isolate the primary factors involved.

The observation of tumor cell migration, which we speculate to be facilitated through EMT, provides a very interesting starting point for future studies. Analysis of cellular response to radiation through in vitro experiments will help to establish the bystander aspect of these effects. Although there is a wealth of data highlighting the potential for bystander signaling to induce indirect cell death, there is a startling lack of information on *if* or *how* these same signals may induce a transformation to a more malignant phenotype in the indirectly affected cells. This is an important aspect of understanding the effects that we have observed, where it appears as though tumor radiation response is prominently directed by the non-irradiated cell fraction.

Investigation of radiation-induced EMT will continue in animal models through collaboration with the lab of Mariano Garcia-Blanco. They have assisted in the development of a 4T1 reporter cell line that changes expression between RFP and GFP depending upon the mesenchymal or endothelial state of the cell. The ability to directly visualize EMT and MET in dorsal window chamber models presents an exciting opportunity to firmly correlate EMT with post-treatment response. This will possibly be the first time this has ever been directly and serially observed in a living tumor.

We have also been presented with the opportunity to explore the hypothesized endothelial cell apoptosis model of radiation response. As described in 1.3.3, Fuks and

141

Kolesnick performed tumor radiation studies on acid sphingomyelinase knock-out mice. The vasculature of these mice is rendered deficient in apoptotic radiation response through the elimination of a key element of the alternative pathway endothelial cells employ to induce programmed cell death. We have acquired these genetically altered mice from the Fuks and Kolesnick lab, and are currently maintaining a colony at Duke. The incorporation of these mice into window chamber studies of tumor radiation response will allow us to directly observe the proposed vascular-mediated resistance to treatment.

We have also acquired a transgenic murine model from Blanche Capel's lab, which expressed the fluorescent proteins mCherry and GRP in its endothelial cells and macrophages, respectively. Through the irradiation of tumors grown in these mice, we will be able to observe the extent to which macrophages may drive vascular alterations. Martin Brown has proposed that tumor associated macrophages play an important role in vasculogenic remodeling after radiation through their assistance in breaking down the extracellular matrix[75,243]. Additionally, macrophages have been shown to play a role in radiation-induced HIF-1 expression through generation of nitric oxide[53]. Preliminary studies of a CXCR1-inhibitor (blocking macrophage signaling) investigated the effects macrophages play in nascent tumor angiogenesis. It would be interesting to expand this study to include post-treatment macrophage-mediated vascular remodeling in this response.

142

Reporters of oxidative stress may also provide invaluable insight into the proposed bystander response observed after microbeam treatment. Although the link between radiation-induced free radical production and bystander signaling seems clear, it remains to be seen exactly how these signals propagate within the tumor. The spatial/temporal aspects of bystander response may be elucidated through the direct visualization of free radical production. Furthermore, the role mitochondrial damage plays in the oxidative stress response may be indicated through measurements of the optical redox ratio (the fluorescence intensity ratios of the endogenous fluorophores FAD and NADH).

There are also many unknown variables associated with the specific doses and geometries of various spatial fractionation schemes. While one method of radiation delivery may produce positive effects in terms of tumor control, another may cause more harm. As we have seen, single beam irradiation has the potential to cause detrimental changes in tumor behavior; however, as noted, this scheme is simplistic compared to most spatial fractionation studies. Manipulation of signaling gradients through alternative geometries may cause significant differences in overall effect. However, these fundamental biological mechanisms are presently poorly understood.

Expansion of this study to simulate a marginal miss through partial tumor irradiation would have immediate clinical impact. The effects of marginal miss are unknown, and clinical treatment outcomes are hard to investigate due to the difficulty of

detecting whether a marginal miss actually occurred. Therefore, animal models may play an important role in understanding this clinical phenomenon. Partial tumor irradiation may be achieved in larger tumors through the use of modern imaging and radiation delivery technologies, including micro-CT. Such a system was recently installed at Duke and may be used by our lab in future studies.

The long-term implications of different radiation treatments need to be investigated. Although we saw a profound angiogenic response and evidence of EMT after microbeam irradiation, it is unclear how this would impact overall survival after treatment. The window chamber model is not well suited to such studies, however. A different approach, such as a flank tumor model, would need to be used in order to observe post-treatment responses over the period of weeks to months. A potentially informative study would involve the full or partial irradiation of a flank tumor, surgical resection, and the detection of lung metastases at a later point. Such a study would provide strong evidence of influence on overall survival.

Finally, it would be interesting to investigate whether the observed change in tumor phenotype is a radiation-specific effect, or if it could be produced by other types of treatment. Surgical trauma and/or incomplete tumor resection may produce similar tumor responses. Since studies have shown that resection of the primary tumor may stimulate the growth of metastases through unknown mechanisms, the possibility of a

linked response may prove further clinical relevance for post-treatment potentiation of

malignant characteristics.

Appendix

Dorsal Window Chamber Surgeries

<u>Reagents:</u>
1. Mice (NCI-Frederick Animal Production Program).
   - Critical: Window chamber surgeries can be successfully performed on a variety of mouse strains. However, care must be taken to ensure that the strain is compatible with the cell line of interest. All experiments should be performed in accordance with relevant national and institutional guidelines and regulations.
2. Tumor cell line and appropriate phenol red–free culture medium (American Type Culture Collection).
   - Caution: Care must be taken to avoid human exposure to cells. Human-derived or virus-associated tumor lines pose a particular hazard. Consult institutional guidelines for proper cell handling.
   - Critical: Cell suspensions should be prepared fresh and used on the same day. Cell suspension should be placed on ice (but not frozen) before use.
3. Ketamine anesthetic (Ketaset 100 mg ml^{-1}; Fort Dodge Animal Health, NDC 0856-4403-01;). Ketamine solution can be stored for several months at room temperature (25 °C), and generally has an expiration date listed.
4. Xylazine muscle relaxant (AnaSed Injection; Lloyd Laboratories, cat. no. 4821). Xylazine solution can be stored for several weeks at room temperature, and generally has an expiration date listed.
5. Sterile NaCl solution (0.9%, wt/vol) (Sodium chloride injection, USP; Hospira, NDC 0409-7983-03). Saline solution can be stored at room temperature up to the expiration date.
6. Ophthalmic ointment (Rugby, NDC 0536-6550-91). It can be stored at room temperature for several months.
7. Hair-removal lotion (for removing hair from mice) can be stored at room temperature for several months.
8. Chlorhexidine (2%, wt/wt) (Boehringer Ingelheim Vetmedica, cat. no. 448315). It can be stored at room temperature for several months.
9. Isopropyl Alcohol (70%, vol/vol) (Medline Industries, NDC-10565-002-16). It can be stored at room temperature indefinitely.
10. Antibiotic ointment (E. Fougera, NDC 0168-0012-09). It can be stored at room temperature until expiration.
11. Buprenophine analgesic (Buprenex Injectable, 0.3 mg ml^{-1}; Reckitt Benckiser Healthcare, cat. no. 7571). It can be stored at room temperature until the expiration date.

12. Sporicidin (Sporicidin, cat. no. RE-1284C). It can be stored at room temperature until the expiration date.

Equipment:
1. Window chamber units (including nuts, retaining rings and glass cover slips) (12-mm window chamber unit, Research Instruments)
2. Custom-machined C-holder (C-holder for 12-mm window chamber unit, Research Instruments)
3. Custom-machined Plexiglas viewing stage
4. Leather hole puncher with 1/8-inch hollow punch (or 16G needle; 223 Revolving Leather Hole Punch; C.S. Osborne)
5. Two large metal binder clips (Staples, cat. no. 10669-CC)
6. Retaining ring pliers (Stanley Proto Industrial Tools, cat. no. SEPTLS577398)
7. Glass microsyringe (25–100 µl volume; 702LT 25ul SYR; Hamilton Company, cat. no. 80401)
8. Metal paper clip (no. 1 size; Staples, cat. no 472480)
9. Sterilization wrap (40 inches × 40 inches, regular weight; Medline Industries, cat. no. GEM2140)
10. Sterile pad (18 inches × 26 inches, Polylined sterile field; Busse Hospital Disposables, cat. no. 696)
11. Surgical marker (150 Skin Marker and Ruler; Devon, Tyco Healthcare Group, cat. no. 31145926)
12. Monosof 4-0 or silk suture (Monofilament nylon suture; Syncture, Tyco Healthcare Group, cat. no. SN-1964)
13. Disposable surgical blade (Bard-Parker, Becton Dickinson Acute Care, cat. no. 37120)
14. Syringe (1 ml; Becton Dickinson, cat. no. 309623)
15. Two 30G needles (Becton Dickinson, cat. no. 305106)
16. Mayo scissors (Harvard Apparatus, cat. no. 728461)
17. Iris scissors (Harvard Apparatus, cat. no. 596903)
18. Conjunctival scissors (Harvard Apparatus, cat. no. 522284)
19. Jeweler-type forceps (Medetz Surgical Instruments, cat. no. M11-08360)
20. Mosquito forceps (Medetz Surgical Instruments, cat. no. 22.1752)
21. Needle holder (Medetz Surgical Instruments, cat. no. 21.1713)
22. Nut driver (Wiha Tools, cat. no. 26592)
23. Petri dish (Sigma-Aldrich, cat. no. P5481-500EA)
24. Cotton gauze (Curad Pro-Gauze; Medline Industries, cat. no. CUR20423)
25. Thermostatic blanket (T/Pump; Gaymar Industries, cat. no. TP700)
26. Gooseneck lamp (Lamps Plus, cat no. N6638)

27. Hot plate (Fisher Scientific, cat. no. 11-510-49SHQ)
28. Glass-bead sterilizer (Germinator 500; Roboz)
29. Custom-machined Plexiglas surgical platform
30. Phase-change wax heating pad (Braintree Scientific, Model 39 DP)
31. Vortexer (Vortex Genie 2; Scientific Industries, Model G560)
32. Surgical tray (Harvard Apparatus, cat. no. 610215)
33. Lab coat (Fisher Scientific, cat. no. S47453A)
34. Sterile surgical gloves (Medline Industries, cat. no. MD5104060)
35. Facemask (3M, cat. no. 1818)
36. Electric shaver for hirsute mice (Oster Professional Products, cat. no. 76054-010)

Reagent Setup:

1. Ketamine/xylazine working solution:
   - Dilute the stock reagents to 10 mg ml^{-1} ketamine and 1 mg ml^{-1} xylazine in sterile 0.9% (wt/vol) NaCl solution. A redosing solution should also be prepared with ketamine only (10 mg ml^{-1}).
   - Critical: Xylazine is not metabolized as rapidly as ketamine, so re-dosing is generally performed with ketamine only. This need not be prepared fresh, and can be stored for several weeks at room temperature.
2. Buprenophine solution:
   - Dilute the stock buprenophine solution to 15 mg ml^{-1} in sterile 0.9% (wt/vol) NaCl solution. This need not be prepared fresh, and can be stored for several weeks at room temperature.
3. Tumor cell suspension:
   - Suspend the cultured cells in appropriate phenol red–free culture medium at a concentration such that a 20-µl volume contains the desired number of cells for inoculation. The cell suspension should be used on the same day as the preparation.

Equipment Setup:

1. Surgical station:
   - Window chamber surgeries must be performed using aseptic technique to minimize the risk of animal infection. A laminar flow HEPA-filtered hood or other flow-isolated environment with an accessible electrical outlet is an ideal location. Within the station, position the fiber optic lamp such that the lamp output is at the appropriate height and angle to illuminate the viewing stage. Place the hot plate and the glass-bead sterilizer in an accessible location. The viewing stage is an 24 × 19 × 3 cm Plexiglas box

with an open bottom and back—the crucial design characteristics are that it is sufficiently large to hold the wax heating pad, and that it provides a sturdy platform for the surgery.

2. Sterilization wrap squares:
   - Cut a piece of 40-inch × 40-inch sterilization wrap into ~6-inch squares. Fold the squares diagonally and make a 3–4 cm slit along the diagonal.
3. Surgical kit preparation:
   - The following items must be sterilized before surgery: window chamber units, C-holder, glass microsyringe, mayo scissors, iris scissors, conjunctival scissors, jeweler-type forceps, mosquito forceps, needle driver, nut driver, cotton gauze, viewing stage, leather hole puncher, binder clips, ring pliers, nut driver, sterilization wrap squares and Petri dish. Place all items that can be safely steam-sterilized into the surgical tray and wrap it in sterilization wrap. Autoclave the kit for at least 90 min at 121 °C. Separately pack and gas-sterilize any items that can rust or melt.
4. Surgical station preparation:
   - Immediately before surgery, thoroughly wipe down all surfaces within the working station with Sporicidin. Place the surgical kit in the middle of the working area and carefully unwrap it without touching the kit itself or the sterile inner surface of the sterilization wrap. The sterilization wrap should now provide a broad sterile surface on which to work. Reach in beneath the sterilization wrap and position the surgical kit to one side of the sterile working area. Using sterile technique, drop the rest of the gas-sterilized and sterile prepackaged equipment into the surgical tray. Heat the paraffin pad in a microwave for a few minutes on the highest power setting until the wax is partially melted. Place the paraffin pad in the middle of the sterile working area. Thoroughly wipe down the surgical platform with Sporicidin and place it on top of the paraffin pad. (Although the paraffin pad and the surgical platform are not sterile, these will be covered with the sterile field at a later point.) Place the sterile Petri dish on the hot pad without touching the inner surface, and fill it with ~10 ml of sterile saline. Heat the saline to ~37 °C.
5. Animal housing:
   - Mice can be housed under standard conditions, ensuring that there is enough clearance for them to move freely in the cage after the window is implanted. A standard rat cage is often convenient for this purpose. Make sure to add sufficient bedding so that the mice can reach their food and water.

The Dorsal Skin-Fold Window Chamber Surgical Procedure:

1. Anesthetize the mouse by intraperitoneal injection of the ketamine/xylazine working solution, corresponding to doses ranging from 85–100 mg kg⁻¹ ketamine and 8.5–10 mg kg⁻¹ xylazine. Place the mouse on a thermostatic blanket in a sternally recumbent position to maintain a body temperature of ~37 °C.
   - Critical step: The mouse should be monitored carefully throughout the surgery for response to any physical stimuli during the procedure and re-dosed appropriately using 25–33% of the initial dose of ketamine only.
2. Apply artificial tear ointment to the mouse's eyes.
   - Critical step: Failure to keep the eyes adequately hydrated can lead to corneal desiccation and permanent eye injury.
3. For surgeries on hairless mice, proceed directly to Step 4. For surgeries on hirsute mice, shear the dorsal area from nape to tail along the back and to the midline of the limbs on either side using an electric shaver. Apply hair removal lotion to the shorn area and remove hair remnants according to the product instructions, usually after ~5 min.
   - Critical step: Product instructions and veterinary guidance must be followed carefully; if the lotion is left on for too long, it can cause skin irritation or injury.
4. Apply chlorhexidine solution to the dorsal region of the mouse's torso and the entire tail with cotton gauze. After thorough application, immediately remove the chlorhexidine with cotton gauze soaked in 70% (vol/vol) ethanol. Repeat this process two more times.
5. Don surgical gear.
   - Critical step: From this point forward, sterile technique should be followed in order to minimize the risk of infection. Do not allow gloved hands or sterile equipment to come into contact with non-sterile objects, including any portion of the mouse not treated with chlorhexidine.
6. Within the surgical area, attach the Plexiglas viewing stage to the surgical platform with the metal binder clips. Cut a rectangular hole in the sterile field so that the viewing stage is exposed through the hole, but the sterile field completely covers the surgical platform.
7. Mark the mouse along the length of the spine with the surgical marker. At the peak of the back, apply two small dots on either side of the line, ~5 mm apart. This will establish a landmark for proper window chamber placement.
8. Drape one of the sterilization wrap squares over the mouse with the slit aligned with the line drawn along the length of the spine. Roll up and secure the loose corners of the square with a paper clip. Take care to handle only the outer side of the sterilization wrap.

9. Transfer the mouse to the sterile working area.
10. Gently pull the loose dorsal skin through the slit and secure it to the C-holder with four stitches made along the back-line such that the skin fans out with enough working area to accommodate the window chamber. For portions of the surgery that require delicate manipulation, the C-holder can be hung from the viewing stage for better visibility.
11. Hold the flat side of one of the window chamber pieces against the skin fold such that the dot that was drawn on the back is aligned with the top screw hold of the window chamber. Mark the positions of the other screw holes and trace the circumference of the window area with the surgical marker.
12. Punch a hole through both sides of the skin at each of the screw locations using either the hole puncher or a 16G needle.
13. Using the mosquito forceps to hold the skin and cutting along the circumference of the drawn circle with the iris scissors, remove the forward-facing portion of skin, leaving the opposing layer intact.
14. Periodically flush the exposed dermis with warm saline (pre-warmed to 37 °C) throughout the remainder of the surgery to clear away blood and keep the dermis hydrated.
15. Using the jeweler forceps and the conjunctival scissors, remove any remaining loose connective tissue, leaving intact the fine, translucent fascial plane that covers the dermis.
16. Insert the screws on the front window chamber frame through the three smaller holes, cutting away any obstructing connective tissue with the conjunctival scissors.
17. Use the nuts to fasten the rear frame to the front frame, manipulating the skin to keep the exposed dermis centered within the frame.
    - Critical step: To avoid infection, the frame must be secured tightly enough to ensure that the wound is fully sealed by the window chamber frame. Avoid over-tightening the frame, however, as this may inhibit circulation and lead to necrosis.
18. Using the microsyringe, and holding the needle tip at a shallow angle with the bevel up, inject ~20 µl of the vortexed tumor-cell suspension between the exposed fascial plane and the dermis. A small bubble should be visible.
    - Critical step: The cell suspension must be injected beneath the fascia to achieve tumor growth. Avoid injection into or damage to the dermal tissue, as this may cause wound lesions that visually obscure the tumor. If necessary, the fascia can be lightly lifted with the jeweler forceps to better facilitate proper injection.
19. While holding it level, fill the window with warm saline until a meniscus forms.

20. Place the glass cover slip over the window with the jeweler forceps. Push the cover slip down into position, allowing the saline to leak out around the edges. Ensure that no air bubbles remain within the sealed window.
21. Secure the cover slip with a retaining ring.
22. With the skin taut, suture the window chamber to the skin using the small holes along the edge of the frame.
23. Use the surgical blade to remove the sutures attaching the skin to the C-holder.
24. Return the mouse to the thermostatic blanket for recovery, and remove the sterile wrapping. Apply antibiotic ointment to the suture wounds. As the mouse begins to regain mobility, subcutaneously inject 0.05–0.15 mg kg^{-1} of buprenorphine solution for pain management.
25. If you are performing further surgeries, wipe down and re-sterilize the contaminated portions of the surgical tools with the glass-bead sterilizer, and ensure that the paraffin heating pad is still warm.
26. Return the mouse to the animal housing facility after it has fully recovered from anesthesia. Tumor growth should be visually apparent within 5–10 d, although this may vary depending on the cell line and mouse strain. Postoperative monitoring should include checking for excessive weight loss, posture, activity level or facial expression. Humane endpoints should be approved by the appropriate regulatory body and generally should include excessive weight loss (>15%) and unresolved infection or pain.
    - Critical step: Some tumor lines grow best in a warm environment. If tumor growth is not apparent after several surgeries, the animals may be housed in an environmental chamber with an elevated temperature and humidity (34 °C with 50% humidity). This ensures that the window chamber tissue remains warm and moist.
27. Re-administer buprenorphine 8–12 h after surgery, and then as needed for pain alleviation. Generally, the animals should recover fully from surgery and anesthesia and show no signs of distress by the next day.
    - Critical step: Examine the mice daily for signs of distress, adhering to appropriate institutional and governmental guidelines for pain management and humane endpoints.

References

1   Hoyert, D. L. 75 years of mortality in the United States, 1935-2010. *NCHS data brief*, 1-8 (2012).

2   Meropol, N. J. *et al.* American Society of Clinical Oncology guidance statement: the cost of cancer care. *Journal of clinical oncology : official journal of the American Society of Clinical Oncology* **27**, 3868-3874, doi:10.1200/JCO.2009.23.1183 (2009).

3   Siegel, R., Naishadham, D. & Jemal, A. Cancer statistics, 2012. *CA: a cancer journal for clinicians* **62**, 10-29, doi:10.3322/caac.20138 (2012).

4   Thun, M. J. *et al.* 50-year trends in smoking-related mortality in the United States. *The New England journal of medicine* **368**, 351-364, doi:10.1056/NEJMsa1211127 (2013).

5   Greenman, C. *et al.* Patterns of somatic mutation in human cancer genomes. *Nature* **446**, 153-158, doi:10.1038/nature05610 (2007).

6   Tannock, I. F. & Hill, R. P. *The Basic Science of Oncology*. 3 edn, (McGraw-Hill, 1998).

7   Weinberg, R. A. Oncogenes and tumor suppressor genes. *CA: a cancer journal for clinicians* **44**, 160-170 (1994).

8   Hollstein, M., Sidransky, D., Vogelstein, B. & Harris, C. C. p53 mutations in human cancers. *Science* **253**, 49-53 (1991).

9   Hanahan, D. & Weinberg, R. A. The hallmarks of cancer. *Cell* **100**, 57-70 (2000).

10   Hanahan, D. & Weinberg, R. A. Hallmarks of cancer: the next generation. *Cell* **144**, 646-674, doi:10.1016/j.cell.2011.02.013 (2011).

11   Blasco, M. A. Telomeres and human disease: ageing, cancer and beyond. *Nature reviews. Genetics* **6**, 611-622, doi:10.1038/nrg1656 (2005).

12   Warburg, O. On respiratory impairment in cancer cells. *Science* **124**, 269-270 (1956).

13   Warburg, O. On the origin of cancer cells. *Science* **123**, 309-314 (1956).

14   Potter, V. R. The biochemical approach to the cancer problem. *Federation proceedings* **17**, 691-697 (1958).

15   Vander Heiden, M. G., Cantley, L. C. & Thompson, C. B. Understanding the Warburg effect: the metabolic requirements of cell proliferation. *Science* **324**, 1029-1033, doi:10.1126/science.1160809 (2009).

16   Kennedy, K. M. & Dewhirst, M. W. Tumor metabolism of lactate: the influence and therapeutic potential for MCT and CD147 regulation. *Future Oncol* **6**, 127-148, doi:10.2217/fon.09.145 (2010).

17   Semenza, G. L. Targeting HIF-1 for cancer therapy. *Nature reviews. Cancer* **3**, 721-732, doi:10.1038/nrc1187 (2003).

18   Moon, E. J., Brizel, D. M., Chi, J. T. & Dewhirst, M. W. The potential role of intrinsic hypoxia markers as prognostic variables in cancer. *Antioxidants & redox signaling* **9**, 1237-1294, doi:10.1089/ars.2007.1623 (2007).

19   Hockel, M., Vorndran, B., Schlenger, K., Baussmann, E. & Knapstein, P. G. Tumor oxygenation: a new predictive parameter in locally advanced cancer of the uterine cervix. *Gynecologic oncology* **51**, 141-149, doi:10.1006/gyno.1993.1262 (1993).

20   Semenza, G. L. & Wang, G. L. A nuclear factor induced by hypoxia via de novo protein synthesis binds to the human erythropoietin gene enhancer at a site required for transcriptional activation. *Molecular and cellular biology* **12**, 5447-5454 (1992).

21   McCord, J. M. & Fridovich, I. Superoxide dismutase: the first twenty years (1968-1988). *Free radical biology & medicine* **5**, 363-369 (1988).

22   BelAiba, R. S. *et al.* Redox-sensitive regulation of the HIF pathway under non-hypoxic conditions in pulmonary artery smooth muscle cells. *Biological chemistry* **385**, 249-257, doi:10.1515/BC.2004.019 (2004).

23   Guzy, R. D. & Schumacker, P. T. Oxygen sensing by mitochondria at complex III: the paradox of increased reactive oxygen species during hypoxia. *Experimental physiology* **91**, 807-819, doi:10.1113/expphysiol.2006.033506 (2006).

24   Dewhirst, M. W., Cao, Y. & Moeller, B. Cycling hypoxia and free radicals regulate angiogenesis and radiotherapy response. *Nature reviews. Cancer* **8**, 425-437, doi:10.1038/nrc2397 (2008).

25   Talmadge, J. E. & Fidler, I. J. AACR centennial series: the biology of cancer
       metastasis: historical perspective. *Cancer research* **70**, 5649-5669, doi:10.1158/0008-
       5472.CAN-10-1040 (2010).

26   Micalizzi, D. S., Farabaugh, S. M. & Ford, H. L. Epithelial-mesenchymal
       transition in cancer: parallels between normal development and tumor
       progression. *Journal of mammary gland biology and neoplasia* **15**, 117-134,
       doi:10.1007/s10911-010-9178-9 (2010).

27   Cavallaro, U. & Christofori, G. Cell adhesion and signalling by cadherins and Ig-
       CAMs in cancer. *Nature reviews. Cancer* **4**, 118-132, doi:10.1038/nrc1276 (2004).

28   Berx, G. & van Roy, F. Involvement of members of the cadherin superfamily in
       cancer. *Cold Spring Harbor perspectives in biology* **1**, a003129,
       doi:10.1101/cshperspect.a003129 (2009).

29   Sullivan, R. & Graham, C. H. Hypoxia-driven selection of the metastatic
       phenotype. *Cancer metastasis reviews* **26**, 319-331, doi:10.1007/s10555-007-9062-2
       (2007).

30   Hugo, H. *et al.* Epithelial--mesenchymal and mesenchymal--epithelial transitions
       in carcinoma progression. *Journal of cellular physiology* **213**, 374-383,
       doi:10.1002/jcp.21223 (2007).

31   Paget, S. The distribution of secondary growths in cancer of the breast. 1889.
       Cancer metastasis reviews **8**, 98-101 (1989).

32   Huang, X. & Saint-Jeannet, J. P. Induction of the neural crest and the
       opportunities of life on the edge. *Developmental biology* **275**, 1-11,
       doi:10.1016/j.ydbio.2004.07.033 (2004).

33   Karnoub, A. E. *et al.* Mesenchymal stem cells within tumour stroma promote
       breast cancer metastasis. *Nature* **449**, 557-563,
       doi:http://www.nature.com/nature/journal/v449/n7162/suppinfo/nature06188_S1.
       html (2007).

34   Qian, B. Z. & Pollard, J. W. Macrophage diversity enhances tumor progression
       and metastasis. *Cell* **141**, 39-51, doi:10.1016/j.cell.2010.03.014 (2010).

35   Wyckoff, J. B. *et al.* Direct visualization of macrophage-assisted tumor cell
       intravasation in mammary tumors. *Cancer research* **67**, 2649-2656,
       doi:10.1158/0008-5472.CAN-06-1823 (2007).

155

36   Mohamed, M. M. & Sloane, B. F. Cysteine cathepsins: multifunctional enzymes in cancer. *Nature reviews. Cancer* **6**, 764-775, doi:10.1038/nrc1949 (2006).

37   Egeblad, M., Nakasone, E. S. & Werb, Z. Tumors as Organs: Complex Tissues that Interface with the Entire Organism. *Developmental cell* **18**, 884-901, doi:http://dx.doi.org/10.1016/j.devcel.2010.05.012 (2010).

38   Shintani, Y. *et al.* Epithelial to Mesenchymal Transition Is a Determinant of Sensitivity to Chemoradiotherapy in Non-Small Cell Lung Cancer. *The Annals of Thoracic Surgery* **92**, 1794-1804, doi:http://dx.doi.org/10.1016/j.athoracsur.2011.07.032 (2011).

39   Camphausen, K. *et al.* Radiation therapy to a primary tumor accelerates metastatic growth in mice. *Cancer research* **61**, 2207-2211 (2001).

40   Wild-Bode, C., Weller, M., Rimner, A., Dichgans, J. & Wick, W. Sublethal irradiation promotes migration and invasiveness of glioma cells: implications for radiotherapy of human glioblastoma. *Cancer research* **61**, 2744-2750 (2001).

41   Vaupel, P. & Harrison, L. Tumor hypoxia: causative factors, compensatory mechanisms, and cellular response. *The oncologist* **9 Suppl 5**, 4-9, doi:10.1634/theoncologist.9-90005-4 (2004).

42   Gray, L. H., Conger, A. D., Ebert, M., Hornsey, S. & Scott, O. C. The concentration of oxygen dissolved in tissues at the time of irradiation as a factor in radiotherapy. *The British journal of radiology* **26**, 638-648 (1953).

43   Teicher, B. A. Hypoxia and drug resistance. *Cancer metastasis reviews* **13**, 139-168 (1994).

44   Graeber, T. G. *et al.* Hypoxia-mediated selection of cells with diminished apoptotic potential in solid tumours. *Nature* **379**, 88-91, doi:10.1038/379088a0 (1996).

45   Wang, G. L., Jiang, B. H., Rue, E. A. & Semenza, G. L. Hypoxia-inducible factor 1 is a basic-helix-loop-helix-PAS heterodimer regulated by cellular O2 tension. *Proceedings of the National Academy of Sciences of the United States of America* **92**, 5510-5514 (1995).

46   Huang, L. E., Arany, Z., Livingston, D. M. & Bunn, H. F. Activation of hypoxia-inducible transcription factor depends primarily upon redox-sensitive

stabilization of its alpha subunit. *The Journal of biological chemistry* **271**, 32253-32259 (1996).

47   Sutter, C. H., Laughner, E. & Semenza, G. L. Hypoxia-inducible factor 1alpha protein expression is controlled by oxygen-regulated ubiquitination that is disrupted by deletions and missense mutations. *Proceedings of the National Academy of Sciences of the United States of America* **97**, 4748-4753, doi:10.1073/pnas.080072497 (2000).

48   Cockman, M. E. *et al.* Hypoxia inducible factor-alpha binding and ubiquitylation by the von Hippel-Lindau tumor suppressor protein. *The Journal of biological chemistry* **275**, 25733-25741, doi:10.1074/jbc.M002740200 (2000).

49   Moeller, B. J., Cao, Y., Li, C. Y. & Dewhirst, M. W. Radiation activates HIF-1 to regulate vascular radiosensitivity in tumors: role of reoxygenation, free radicals, and stress granules. *Cancer cell* **5**, 429-441 (2004).

50   Bussink, J., Kaanders, J. H., Rijken, P. F., Raleigh, J. A. & Van der Kogel, A. J. Changes in blood perfusion and hypoxia after irradiation of a human squamous cell carcinoma xenograft tumor line. *Radiation research* **153**, 398-404 (2000).

51   Dewhirst, M. W. *et al.* Heterogeneity in tumor microvascular response to radiation. *International journal of radiation oncology, biology, physics* **18**, 559-568 (1990).

52   Chandel, N. S. *et al.* Reactive oxygen species generated at mitochondrial complex III stabilize hypoxia-inducible factor-1alpha during hypoxia: a mechanism of O2 sensing. *The Journal of biological chemistry* **275**, 25130-25138, doi:10.1074/jbc.M001914200 (2000).

53   Li, F. *et al.* Regulation of HIF-1alpha stability through S-nitrosylation. *Molecular cell* **26**, 63-74, doi:10.1016/j.molcel.2007.02.024 (2007).

54   Lanzen, J. *et al.* Direct demonstration of instabilities in oxygen concentrations within the extravascular compartment of an experimental tumor. *Cancer research* **66**, 2219-2223 (2006).

55   Braun, R. D., Lanzen, J. L. & Dewhirst, M. W. Fourier analysis of fluctuations of oxygen tension and blood flow in R3230Ac tumors and muscle in rats. *The American journal of physiology* **277**, H551-568 (1999).

56   Brurberg, K. G., Skogmo, H. K., Graff, B. A., Olsen, D. R. & Rofstad, E. K. Fluctuations in pO2 in poorly and well-oxygenated spontaneous canine tumors before and during fractionated radiation therapy. *Radiotherapy and oncology : journal of the European Society for Therapeutic Radiology and Oncology* **77**, 220-226, doi:10.1016/j.radonc.2005.09.009 (2005).

57   Cardenas-Navia, L. I. *et al.* Tumor-dependent kinetics of partial pressure of oxygen fluctuations during air and oxygen breathing. *Cancer research* **64**, 6010-6017, doi:10.1158/0008-5472.CAN-03-0947 (2004).

58   Pigott, K. H., Hill, S. A., Chaplin, D. J. & Saunders, M. I. Microregional fluctuations in perfusion within human tumours detected using laser Doppler flowmetry. *Radiotherapy and oncology : journal of the European Society for Therapeutic Radiology and Oncology* **40**, 45-50 (1996).

59   Kimura, H. *et al.* Fluctuations in red cell flux in tumor microvessels can lead to transient hypoxia and reoxygenation in tumor parenchyma. *Cancer research* **56**, 5522-5528 (1996).

60   Patan, S., Munn, L. L. & Jain, R. K. Intussusceptive microvascular growth in a human colon adenocarcinoma xenograft: a novel mechanism of tumor angiogenesis. *Microvascular research* **51**, 260-272, doi:10.1006/mvre.1996.0025 (1996).

61   Baudelet, C. *et al.* The role of vessel maturation and vessel functionality in spontaneous fluctuations of T2*-weighted GRE signal within tumors. *NMR in biomedicine* **19**, 69-76, doi:10.1002/nbm.1002 (2006).

62   Dewhirst, M. W. *et al.* Microvascular studies on the origins of perfusion-limited hypoxia. *The British journal of cancer. Supplement* **27**, S247-251 (1996).

63   Kavanagh, B. D., Coffey, B. E., Needham, D., Hochmuth, R. M. & Dewhirst, M. W. The effect of flunarizine on erythrocyte suspension viscosity under conditions of extreme hypoxia, low pH, and lactate treatment. *British journal of cancer* **67**, 734-741 (1993).

64   Kiani, M. F., Pries, A. R., Hsu, L. L., Sarelius, I. H. & Cokelet, G. R. Fluctuations in microvascular blood flow parameters caused by hemodynamic mechanisms. *The American journal of physiology* **266**, H1822-1828 (1994).

65   Pries, A. R., Schonfeld, D., Gaehtgens, P., Kiani, M. F. & Cokelet, G. R. Diameter variability and microvascular flow resistance. *The American journal of physiology* **272**, H2716-2725 (1997).

66   Nehmeh, S. A. *et al.* Reproducibility of intratumor distribution of (18)F-fluoromisonidazole in head and neck cancer. *International journal of radiation oncology, biology, physics* **70**, 235-242, doi:10.1016/j.ijrobp.2007.08.036 (2008).

67   Cao, Y. *et al.* Observation of incipient tumor angiogenesis that is independent of hypoxia and hypoxia inducible factor-1 activation. *Cancer research* **65**, 5498-5505, doi:10.1158/0008-5472.CAN-04-4553 (2005).

68   Peng, Y. J. *et al.* Heterozygous HIF-1alpha deficiency impairs carotid body-mediated systemic responses and reactive oxygen species generation in mice exposed to intermittent hypoxia. *The Journal of physiology* **577**, 705-716, doi:10.1113/jphysiol.2006.114033 (2006).

69   Yuan, G., Nanduri, J., Bhasker, C. R., Semenza, G. L. & Prabhakar, N. R. Ca2+/calmodulin kinase-dependent activation of hypoxia inducible factor 1 transcriptional activity in cells subjected to intermittent hypoxia. *The Journal of biological chemistry* **280**, 4321-4328, doi:10.1074/jbc.M407706200 (2005).

70   Semenza, G. L. & Prabhakar, N. R. HIF-1-dependent respiratory, cardiovascular, and redox responses to chronic intermittent hypoxia. *Antioxidants & redox signaling* **9**, 1391-1396, doi:10.1089/ars.2007.1691 (2007).

71   Toffoli, S., Feron, O., Raes, M. & Michiels, C. Intermittent hypoxia changes HIF-1alpha phosphorylation pattern in endothelial cells: unravelling of a new PKA-dependent regulation of HIF-1alpha. *Biochimica et biophysica acta* **1773**, 1558-1571, doi:10.1016/j.bbamcr.2007.06.002 (2007).

72   Martinive, P. *et al.* Preconditioning of the tumor vasculature and tumor cells by intermittent hypoxia: implications for anticancer therapies. *Cancer research* **66**, 11736-11744, doi:10.1158/0008-5472.CAN-06-2056 (2006).

73   Burri, P. H. & Tarek, M. R. A novel mechanism of capillary growth in the rat pulmonary microcirculation. *The Anatomical record* **228**, 35-45, doi:10.1002/ar.1092280107 (1990).

74   Lyden, D. *et al.* Impaired recruitment of bone-marrow-derived endothelial and hematopoietic precursor cells blocks tumor angiogenesis and growth. *Nature medicine* **7**, 1194-1201, doi:10.1038/nm1101-1194 (2001).

75   Ahn, G. O. & Brown, J. M. Matrix metalloproteinase-9 is required for tumor vasculogenesis but not for angiogenesis: role of bone marrow-derived myelomonocytic cells. *Cancer cell* **13**, 193-205, doi:10.1016/j.ccr.2007.11.032 (2008).

76   Dewhirst, M. W., Richardson, R., Cardenas-Navia, I. & Cao, Y. The relationship between the tumor physiologic microenvironment and angiogenesis. *Hematology/oncology clinics of North America* **18**, 973-990, vii, doi:10.1016/j.hoc.2004.06.006 (2004).

77   Haroon, Z., Peters, K., Greenberg, C. & Dewhirst, M. in *Antiangiogenic agents in cancer therapy* (ed B. A. Teicher) Ch. 1, 3-21 (Humana Press Inc., 1999).

78   Folkman, J. Tumor angiogenesis: therapeutic implications. *The New England journal of medicine* **285**, 1182-1186, doi:10.1056/NEJM197111182852108 (1971).

79   Algire, G. H. *et al.* Vascular reactions of normal and malignant tissues in vivo. III. Vascular reactions' of mice to fibroblasts treated in vitro with methylcholanthrene. *Journal of the National Cancer Institute* **11**, 555-580 (1950).

80   Sandison, J. C. Observations on growth of blood vessels as seen in transparent chamber introduced into rabbit's ear. *Am. J. Anat.* **41**, 475-496 (1928).

81   Algire, G. H. An adaptation of the transparent chamber technique to the mouse. *Journal of the National Cancer Institute* **4**, 1-10 (1943).

82   Greenblatt, M. & Shubi, P. Tumor angiogenesis: transfilter diffusion studies in the hamster by the transparent chamber technique. *Journal of the National Cancer Institute* **41**, 111-124 (1968).

83   Senger, D. R. *et al.* Tumor cells secrete a vascular permeability factor that promotes accumulation of ascites fluid. *Science* **219**, 983-985 (1983).

84   Ferrara, N. & Henzel, W. J. Pituitary follicular cells secrete a novel heparin-binding growth factor specific for vascular endothelial cells. *Biochemical and biophysical research communications* **161**, 851-858 (1989).

85   Leung, D. W., Cachianes, G., Kuang, W. J., Goeddel, D. V. & Ferrara, N. Vascular endothelial growth factor is a secreted angiogenic mitogen. *Science* **246**, 1306-1309 (1989).

86   Keck, P. J. *et al.* Vascular permeability factor, an endothelial cell mitogen related to PDGF. *Science* **246**, 1309-1312 (1989).

87   Folkman, J., Haudenschild, C. C. & Zetter, B. R. Long-term culture of capillary endothelial cells. *Proceedings of the National Academy of Sciences of the United States of America* **76**, 5217-5221 (1979).

88   Folkman, J. & Klagsbrun, M. Angiogenic factors. *Science* **235**, 442-447 (1987).

89   Houck, K. A. *et al.* The vascular endothelial growth factor family: identification of a fourth molecular species and characterization of alternative splicing of RNA. *Molecular endocrinology* **5**, 1806-1814 (1991).

90   Tischer, E. *et al.* The human gene for vascular endothelial growth factor. Multiple protein forms are encoded through alternative exon splicing. *The Journal of biological chemistry* **266**, 11947-11954 (1991).

91   Cohen, T. *et al.* VEGF121, a vascular endothelial growth factor (VEGF) isoform lacking heparin binding ability, requires cell-surface heparan sulfates for efficient binding to the VEGF receptors of human melanoma cells. *The Journal of biological chemistry* **270**, 11322-11326 (1995).

92   Park, J. E., Keller, G. A. & Ferrara, N. The vascular endothelial growth factor (VEGF) isoforms: differential deposition into the subepithelial extracellular matrix and bioactivity of extracellular matrix-bound VEGF. *Molecular biology of the cell* **4**, 1317-1326 (1993).

93   Houck, K. A., Leung, D. W., Rowland, A. M., Winer, J. & Ferrara, N. Dual regulation of vascular endothelial growth factor bioavailability by genetic and proteolytic mechanisms. *The Journal of biological chemistry* **267**, 26031-26037 (1992).

94   Plouet, J. *et al.* Extracellular cleavage of the vascular endothelial growth factor 189-amino acid form by urokinase is required for its mitogenic effect. *The Journal of biological chemistry* **272**, 13390-13396 (1997).

95   Plouet, J., Schilling, J. & Gospodarowicz, D. Isolation and characterization of a newly identified endothelial cell mitogen produced by AtT-20 cells. *The EMBO journal* **8**, 3801-3806 (1989).

96   Gospodarowicz, D., Abraham, J. A. & Schilling, J. Isolation and characterization of a vascular endothelial cell mitogen produced by pituitary-derived folliculo stellate cells. *Proceedings of the National Academy of Sciences of the United States of America* **86**, 7311-7315 (1989).

97   Asahara, T. *et al.* Synergistic effect of vascular endothelial growth factor and basic fibroblast growth factor on angiogenesis in vivo. *Circulation* **92**, II365-371 (1995).

98   Jonca, F., Ortega, N., Gleizes, P. E., Bertrand, N. & Plouet, J. Cell release of bioactive fibroblast growth factor 2 by exon 6-encoded sequence of vascular endothelial growth factor. *The Journal of biological chemistry* **272**, 24203-24209 (1997).

99   Gitay-Goren, H. *et al.* Selective binding of VEGF121 to one of the three vascular endothelial growth factor receptors of vascular endothelial cells. *The Journal of biological chemistry* **271**, 5519-5523 (1996).

100   Gengrinovitch, S. *et al.* Glypican-1 is a VEGF165 binding proteoglycan that acts as an extracellular chaperone for VEGF165. *The Journal of biological chemistry* **274**, 10816-10822 (1999).

101   Grimmond, S. *et al.* Cloning and characterization of a novel human gene related to vascular endothelial growth factor. *Genome research* **6**, 124-131 (1996).

102   Olofsson, B. *et al.* Genomic organization of the mouse and human genes for vascular endothelial growth factor B (VEGF-B) and characterization of a second splice isoform. *The Journal of biological chemistry* **271**, 19310-19317 (1996).

103   Makinen, T. *et al.* Differential binding of vascular endothelial growth factor B splice and proteolytic isoforms to neuropilin-1. *The Journal of biological chemistry* **274**, 21217-21222 (1999).

104   Olofsson, B. *et al.* Vascular endothelial growth factor B (VEGF-B) binds to VEGF receptor-1 and regulates plasminogen activator activity in endothelial cells. *Proceedings of the National Academy of Sciences of the United States of America* **95**, 11709-11714 (1998).

105   Olofsson, B. *et al.* Vascular endothelial growth factor B, a novel growth factor for endothelial cells. *Proceedings of the National Academy of Sciences of the United States of America* **93**, 2576-2581 (1996).

106   Jeltsch, M. *et al.* Hyperplasia of lymphatic vessels in VEGF-C transgenic mice. *Science* **276**, 1423-1425 (1997).

107   Achen, M. G. *et al.* Vascular endothelial growth factor D (VEGF-D) is a ligand for the tyrosine kinases VEGF receptor 2 (Flk1) and VEGF receptor 3 (Flt4).

Proceedings of the National Academy of Sciences of the United States of America **95**, 548-553 (1998).

108   Lee, J. *et al.* Vascular endothelial growth factor-related protein: a ligand and specific activator of the tyrosine kinase receptor Flt4. *Proceedings of the National Academy of Sciences of the United States of America* **93**, 1988-1992 (1996).

109   Karkkainen, M. J., Makinen, T. & Alitalo, K. Lymphatic endothelium: a new frontier of metastasis research. *Nature cell biology* **4**, E2-5 (2002).

110   Joukov, V. *et al.* A novel vascular endothelial growth factor, VEGF-C, is a ligand for the Flt4 (VEGFR-3) and KDR (VEGFR-2) receptor tyrosine kinases. *The EMBO journal* **15**, 290-298 (1996).

111   Kukk, E. *et al.* VEGF-C receptor binding and pattern of expression with VEGFR-3 suggests a role in lymphatic vascular development. *Development (Cambridge, England)* **122**, 3829-3837 (1996).

112   Ogawa, S. *et al.* A novel type of vascular endothelial growth factor, VEGF-E (NZ-7 VEGF), preferentially utilizes KDR/Flk-1 receptor and carries a potent mitotic activity without heparin-binding domain. *The Journal of biological chemistry* **273**, 31273-31282 (1998).

113   Lyttle, D. J., Fraser, K. M., Fleming, S. B., Mercer, A. A. & Robinson, A. J. Homologs of vascular endothelial growth factor are encoded by the poxvirus orf virus. *Journal of virology* **68**, 84-92 (1994).

114   Phillips, H. S., Hains, J., Leung, D. W. & Ferrara, N. Vascular endothelial growth factor is expressed in rat corpus luteum. *Endocrinology* **127**, 965-967 (1990).

115   Jakeman, L. B., Armanini, M., Phillips, H. S. & Ferrara, N. Developmental expression of binding sites and messenger ribonucleic acid for vascular endothelial growth factor suggests a role for this protein in vasculogenesis and angiogenesis. *Endocrinology* **133**, 848-859 (1993).

116   Shweiki, D., Itin, A., Neufeld, G., Gitay-Goren, H. & Keshet, E. Patterns of expression of vascular endothelial growth factor (VEGF) and VEGF receptors in mice suggest a role in hormonally regulated angiogenesis. *The Journal of clinical investigation* **91**, 2235-2243 (1993).

117   Miller, J. W. *et al.* Vascular endothelial growth factor/vascular permeability factor is temporally and spatially correlated with ocular angiogenesis in a primate model. *The American journal of pathology* **145**, 574-584 (1994).

118   Shweiki, D., Itin, A., Soffer, D. & Keshet, E. Vascular endothelial growth factor induced by hypoxia may mediate hypoxia-initiated angiogenesis. *Nature* **359**, 843-845 (1992).

119   Minchenko, A., Bauer, T., Salceda, S. & Caro, J. Hypoxic stimulation of vascular endothelial growth factor expression in vitro and in vivo. *Laboratory investigation; a journal of technical methods and pathology* **71**, 374-379 (1994).

120   Enholm, B. *et al.* Comparison of VEGF, VEGF-B, VEGF-C and Ang-1 mRNA regulation by serum, growth factors, oncoproteins and hypoxia. *Oncogene* **14**, 2475-2483 (1997).

121   Brogi, E., Wu, T., Namiki, A. & Isner, J. M. Indirect angiogenic cytokines upregulate VEGF and bFGF gene expression in vascular smooth muscle cells, whereas hypoxia upregulates VEGF expression only. *Circulation* **90**, 649-652 (1994).

122   Levy, A. P., Levy, N. S., Wegner, S. & Goldberg, M. A. Transcriptional regulation of the rat vascular endothelial growth factor gene by hypoxia. *The Journal of biological chemistry* **270**, 13333-13340 (1995).

123   Liu, Y., Cox, S. R., Morita, T. & Kourembanas, S. Hypoxia regulates vascular endothelial growth factor gene expression in endothelial cells. Identification of a 5' enhancer. *Circulation research* **77**, 638-643 (1995).

124   Carmeliet, P. *et al.* Abnormal blood vessel development and lethality in embryos lacking a single VEGF allele. *Nature* **380**, 435-439 (1996).

125   Ferrara, N. *et al.* Heterozygous embryonic lethality induced by targeted inactivation of the VEGF gene. *Nature* **380**, 439-442 (1996).

126   FONTANELLA, A. N., CAO, Y. & DEWHIRST, M. W. Vascular Epithelial Growth Factor (VEGF) Receptors. *Combining Targeted Biological Agents with Radiotherapy: Current Status and Future Directions*, 33 (2008).

127   Shibuya, M. *et al.* Nucleotide sequence and expression of a novel human receptor-type tyrosine kinase gene (flt) closely related to the fms family. *Oncogene* **5**, 519-524 (1990).

128   Terman, B. I. *et al.* Identification of a new endothelial cell growth factor receptor tyrosine kinase. *Oncogene* **6**, 1677-1683 (1991).

129   Keyt, B. A. *et al.* Identification of vascular endothelial growth factor determinants for binding KDR and FLT-1 receptors. Generation of receptor-selective VEGF variants by site-directed mutagenesis. *The Journal of biological chemistry* **271**, 5638-5646 (1996).

130   Wiesmann, C. *et al.* Crystal structure at 1.7 A resolution of VEGF in complex with domain 2 of the Flt-1 receptor. *Cell* **91**, 695-704 (1997).

131   Barleon, B. *et al.* Mapping of the sites for ligand binding and receptor dimerization at the extracellular domain of the vascular endothelial growth factor receptor FLT-1. *The Journal of biological chemistry* **272**, 10382-10388 (1997).

132   Guo, D., Jia, Q., Song, H. Y., Warren, R. S. & Donner, D. B. Vascular endothelial cell growth factor promotes tyrosine phosphorylation of mediators of signal transduction that contain SH2 domains. Association with endothelial cell proliferation. *The Journal of biological chemistry* **270**, 6729-6733 (1995).

133   Waltenberger, J., Claesson-Welsh, L., Siegbahn, A., Shibuya, M. & Heldin, C. H. Different signal transduction properties of KDR and Flt1, two receptors for vascular endothelial growth factor. *The Journal of biological chemistry* **269**, 26988-26995 (1994).

134   Shalaby, F. *et al.* Failure of blood-island formation and vasculogenesis in Flk-1-deficient mice. *Nature* **376**, 62-66 (1995).

135   Fong, G. H., Rossant, J., Gertsenstein, M. & Breitman, M. L. Role of the Flt-1 receptor tyrosine kinase in regulating the assembly of vascular endothelium. *Nature* **376**, 66-70 (1995).

136   Fong, G. H., Zhang, L., Bryce, D. M. & Peng, J. Increased hemangioblast commitment, not vascular disorganization, is the primary defect in flt-1 knock-out mice. *Development (Cambridge, England)* **126**, 3015-3025 (1999).

137   Park, J. E., Chen, H. H., Winer, J., Houck, K. A. & Ferrara, N. Placenta growth factor. Potentiation of vascular endothelial growth factor bioactivity, in vitro and in vivo, and high affinity binding to Flt-1 but not to Flk-1/KDR. *The Journal of biological chemistry* **269**, 25646-25654 (1994).

138   Hiratsuka, S., Minowa, O., Kuno, J., Noda, T. & Shibuya, M. Flt-1 lacking the tyrosine kinase domain is sufficient for normal development and angiogenesis in mice. *Proceedings of the National Academy of Sciences of the United States of America* **95**, 9349-9354 (1998).

139   Barleon, B. *et al.* Migration of human monocytes in response to vascular endothelial growth factor (VEGF) is mediated via the VEGF receptor flt-1. *Blood* **87**, 3336-3343 (1996).

140   Clauss, M. *et al.* The vascular endothelial growth factor receptor Flt-1 mediates biological activities. Implications for a functional role of placenta growth factor in monocyte activation and chemotaxis. *The Journal of biological chemistry* **271**, 17629-17634 (1996).

141   Kaipainen, A. *et al.* Expression of the fms-like tyrosine kinase 4 gene becomes restricted to lymphatic endothelium during development. *Proceedings of the National Academy of Sciences of the United States of America* **92**, 3566-3570 (1995).

142   Kendall, R. L., Wang, G. & Thomas, K. A. Identification of a natural soluble form of the vascular endothelial growth factor receptor, FLT-1, and its heterodimerization with KDR. *Biochemical and biophysical research communications* **226**, 324-328 (1996).

143   Jones, N., Iljin, K., Dumont, D. J. & Alitalo, K. Tie receptors: new modulators of angiogenic and lymphangiogenic responses. *Nature reviews* **2**, 257-267 (2001).

144   Wood, J. M. *et al.* PTK787/ZK 222584, a novel and potent inhibitor of vascular endothelial growth factor receptor tyrosine kinases, impairs vascular endothelial growth factor-induced responses and tumor growth after oral administration. *Cancer research* **60**, 2178-2189 (2000).

145   Lin, P. *et al.* Inhibition of tumor angiogenesis using a soluble receptor establishes a role for Tie2 in pathologic vascular growth. *The Journal of clinical investigation* **100**, 2072-2078 (1997).

146   Thurston, G. *et al.* Leakage-resistant blood vessels in mice transgenically overexpressing angiopoietin-1. *Science* **286**, 2511-2514 (1999).

147   Davis, S. *et al.* Isolation of angiopoietin-1, a ligand for the TIE2 receptor, by secretion-trap expression cloning. *Cell* **87**, 1161-1169 (1996).

148   Kanda, S., Miyata, Y., Mochizuki, Y., Matsuyama, T. & Kanetake, H. Angiopoietin 1 is mitogenic for cultured endothelial cells. *Cancer research* **65**, 6820-6827 (2005).

149   Suri, C. *et al.* Requisite role of angiopoietin-1, a ligand for the TIE2 receptor, during embryonic angiogenesis. *Cell* **87**, 1171-1180 (1996).

150   Gale, N. W. *et al.* Angiopoietin-2 is required for postnatal angiogenesis and lymphatic patterning, and only the latter role is rescued by Angiopoietin-1. *Developmental cell* **3**, 411-423 (2002).

151   Maisonpierre, P. C. *et al.* Angiopoietin-2, a natural antagonist for Tie2 that disrupts in vivo angiogenesis. *Science* **277**, 55-60 (1997).

152   Hammes, H. P. *et al.* Angiopoietin-2 causes pericyte dropout in the normal retina: evidence for involvement in diabetic retinopathy. *Diabetes* **53**, 1104-1110 (2004).

153   Cao, Y. *et al.* Systemic overexpression of angiopoietin-2 promotes tumor microvessel regression and inhibits angiogenesis and tumor growth. *Cancer research* **67**, 3835-3844 (2007).

154   Oh, H. *et al.* Hypoxia and vascular endothelial growth factor selectively up-regulate angiopoietin-2 in bovine microvascular endothelial cells. *The Journal of biological chemistry* **274**, 15732-15739 (1999).

155   Currie, M. J. *et al.* Expression of the angiopoietins and their receptor Tie2 in human renal clear cell carcinomas; regulation by the von Hippel-Lindau gene and hypoxia. *The Journal of pathology* **198**, 502-510 (2002).

156   Tait, C. R. & Jones, P. F. Angiopoietins in tumours: the angiogenic switch. *The Journal of pathology* **204**, 1-10 (2004).

157   Lobov, I. B., Brooks, P. C. & Lang, R. A. Angiopoietin-2 displays VEGF-dependent modulation of capillary structure and endothelial cell survival in vivo. *Proceedings of the National Academy of Sciences of the United States of America* **99**, 11205-11210 (2002).

158   Bergers, G. & Benjamin, L. E. Tumorigenesis and the angiogenic switch. *Nature reviews. Cancer* **3**, 401-410 (2003).

159   Dor, Y., Porat, R. & Keshet, E. Vascular endothelial growth factor and vascular adjustments to perturbations in oxygen homeostasis. *American journal of physiology* **280**, C1367-1374 (2001).

160   Folkman, J. Angiogenesis in cancer, vascular, rheumatoid and other disease. *Nature medicine* **1**, 27-31 (1995).

161   Hanahan, D. & Folkman, J. Patterns and emerging mechanisms of the angiogenic switch during tumorigenesis. *Cell* **86**, 353-364 (1996).

162   Hobson, B. & Denekamp, J. Endothelial proliferation in tumours and normal tissues: continuous labelling studies. *British journal of cancer* **49**, 405-413 (1984).

163   Dvorak, H. F. Tumors: wounds that do not heal. Similarities between tumor stroma generation and wound healing. *The New England journal of medicine* **315**, 1650-1659 (1986).

164   Li, C. Y. *et al.* Initial stages of tumor cell-induced angiogenesis: evaluation via skin window chambers in rodent models. *Journal of the National Cancer Institute* **92**, 143-147 (2000).

165   Holash, J. *et al.* Vessel cooption, regression, and growth in tumors mediated by angiopoietins and VEGF. *Science* **284**, 1994-1998 (1999).

166   Pezzella, F. *et al.* Angiogenesis in primary lung cancer and lung secondaries. *Eur J Cancer* **32A**, 2494-2500 (1996).

167   Folkman, J. Incipient angiogenesis. *Journal of the National Cancer Institute* **92**, 94-95 (2000).

168   Raleigh, J. A. *et al.* Hypoxia and vascular endothelial growth factor expression in human squamous cell carcinomas using pimonidazole as a hypoxia marker. *Cancer research* **58**, 3765-3768 (1998).

169   Padera, T. P. *et al.* Pathology: cancer cells compress intratumour vessels. *Nature* **427**, 695 (2004).

170   Griffon-Etienne, G., Boucher, Y., Brekken, C., Suit, H. D. & Jain, R. K. Taxane-induced apoptosis decompresses blood vessels and lowers interstitial fluid pressure in solid tumors: clinical implications. *Cancer research* **59**, 3776-3782 (1999).

171   Warburg, O. The metabolism of tumors. *Constable and Co., Ltd., London* (1930).

172   Brizel, D. M. *et al.* Tumor oxygenation predicts for the likelihood of distant metastases in human soft tissue sarcoma. *Cancer research* **56**, 941-943 (1996).

173   Hockel, M. *et al.* Association between tumor hypoxia and malignant progression in advanced cancer of the uterine cervix. *Cancer research* **56**, 4509-4515 (1996).

174   Kerbel, R. & Folkman, J. Clinical translation of angiogenesis inhibitors. *Nature reviews. Cancer* **2**, 727-739 (2002).

175   Yang, J. C. *et al.* A randomized trial of bevacizumab, an anti-vascular endothelial growth factor antibody, for metastatic renal cancer. *The New England journal of medicine* **349**, 427-434 (2003).

176   Mayer, R. J. Two steps forward in the treatment of colorectal cancer. *The New England journal of medicine* **350**, 2406-2408 (2004).

177   Skillings, J. R., Johnson, D. H., Miller, K. & Kabbinavar, F. Arterial thromboembolic events (ATEs) in a pooled analysis of 5 randomized, controlled trials (RCTs) of bevacizumab (BV) with chemotherapy. *Journal of Clinical Oncology* **23** (2005).

178   Teicher, B. A. A systems approach to cancer therapy. (Antioncogenics + standard cytotoxics-->mechanism(s) of interaction). *Cancer metastasis reviews* **15**, 247-272 (1996).

179   Jain, R. K. Normalization of tumor vasculature: an emerging concept in antiangiogenic therapy. *Science* **307**, 58-62 (2005).

180   Tong, R. T. *et al.* Vascular normalization by vascular endothelial growth factor receptor 2 blockade induces a pressure gradient across the vasculature and improves drug penetration in tumors. *Cancer research* **64**, 3731-3736 (2004).

181   Shih, S. C. *et al.* Transforming growth factor beta1 induction of vascular endothelial growth factor receptor 1: mechanism of pericyte-induced vascular survival in vivo. *Proceedings of the National Academy of Sciences of the United States of America* **100**, 15859-15864 (2003).

182   Kimura, H. & Esumi, H. Reciprocal regulation between nitric oxide and vascular endothelial growth factor in angiogenesis. *Acta biochimica Polonica* **50**, 49-59, doi:035001049 (2003).

183   Ku, D. D., Zaleski, J. K., Liu, S. & Brock, T. A. Vascular endothelial growth factor induces EDRF-dependent relaxation in coronary arteries. *The American journal of physiology* **265**, H586-592 (1993).

184   Dewhirst, M. W., Navia, I. C., Brizel, D. M., Willett, C. & Secomb, T. W. Multiple etiologies of tumor hypoxia require multifaceted solutions. *Clin Cancer Res* **13**, 375-377 (2007).

185   Willett, C. G. *et al.* Direct evidence that the VEGF-specific antibody bevacizumab has antivascular effects in human rectal cancer. *Nature medicine* **10**, 145-147 (2004).

186   Batchelor, T. T. *et al.* AZD2171, a pan-VEGF receptor tyrosine kinase inhibitor, normalizes tumor vasculature and alleviates edema in glioblastoma patients. *Cancer cell* **11**, 83-95 (2007).

187   Hall, E. J. & Giaccia, A. J. *Radiobiology for the Radiologist*. (Lippincott Williams & Wilkins, 2005).

188   Castedo, M. *et al.* Cell death by mitotic catastrophe: a molecular definition. *Oncogene* **23**, 2825-2837, doi:10.1038/sj.onc.1207528 (2004).

189   Serduc, R. *et al.* In vivo two-photon microscopy study of short-term effects of microbeam irradiation on normal mouse brain microvasculature. *International Journal of Radiation Oncology*Biology*Physics* **64**, 1519-1527, doi:http://dx.doi.org/10.1016/j.ijrobp.2005.11.047 (2006).

190   Mohiuddin, M. *et al.* High-dose spatially-fractionated radiation (GRID): a new paradigm in the management of advanced cancers. *International Journal of Radiation Oncology*Biology*Physics* **45**, 721-727, doi:http://dx.doi.org/10.1016/S0360-3016(99)00170-4 (1999).

191   Huhn, J. L. *et al.* Spatially fractionated GRID radiation treatment of advanced neck disease associated with head and neck cancer. *Technology in cancer research & treatment* **5**, 607-612 (2006).

192   Penagaricano, J. A., Moros, E. G., Ratanatharathorn, V., Yan, Y. & Corry, P. Evaluation of spatially fractionated radiotherapy (GRID) and definitive chemoradiotherapy with curative intent for locally advanced squamous cell carcinoma of the head and neck: initial response rates and toxicity. *International journal of radiation oncology, biology, physics* **76**, 1369-1375, doi:10.1016/j.ijrobp.2009.03.030 (2010).

193   Somaiah, N. *et al.* High Dose Spatially Fractionated Radiotherapy (SFR) using a Megavoltage GRID in Advanced Lung Tumors: Preliminary Experience in UK. *International Journal of Radiation Oncology*Biology*Physics* **72**, S490, doi:http://dx.doi.org/10.1016/j.ijrobp.2008.06.1439 (2008).

194   Garcia-Barros, M. *et al.* Tumor response to radiotherapy regulated by endothelial cell apoptosis. *Science* **300**, 1155-1159, doi:10.1126/science.1082504 (2003).

195   Paris, F. *et al.* Endothelial apoptosis as the primary lesion initiating intestinal radiation damage in mice. *Science* **293**, 293-297, doi:10.1126/science.1060191 (2001).

196   Brown, M. What causes the radiation gastrointestinal syndrome?: overview. *International journal of radiation oncology, biology, physics* **70**, 799-800 (2008).

197   Potten, C. S. Extreme sensitivity of some intestinal crypt cells to X and [gamma] irradiation. *Nature* **269**, 518-521 (1977).

198   Folkman, J. Editorial: Is Tissue Mass Regulated by Vascular Endothelial Cells? Prostate as the First Evidence. *Endocrinology* **139**, 441-442, doi:10.1210/en.139.2.441 (1998).

199   Haimovitz-Friedman, A. *et al.* Ionizing radiation acts on cellular membranes to generate ceramide and initiate apoptosis. *The Journal of experimental medicine* **180**, 525-535 (1994).

200   Marathe, S. *et al.* Human vascular endothelial cells are a rich and regulatable source of secretory sphingomyelinase. Implications for early atherogenesis and ceramide-mediated cell signaling. *The Journal of biological chemistry* **273**, 4081-4088 (1998).

201   Jarvis, W. D. *et al.* Induction of apoptotic DNA damage and cell death by activation of the sphingomyelin pathway. *Proceedings of the National Academy of Sciences of the United States of America* **91**, 73-77 (1994).

202   Obeid, L. M., Linardic, C. M., Karolak, L. A. & Hannun, Y. A. Programmed cell death induced by ceramide. *Science* **259**, 1769-1771 (1993).

203   Suit, H. D. & Willers, H. Comment on "Tumor response to radiotherapy regulated by endothelial cell apoptosis" (I). *Science* **302**, 1894; author reply 1894, doi:10.1126/science.1089918 (2003).

204   Brown, M. *et al.* Comment on "Tumor response to radiotherapy regulated by endothelial cell apoptosis" (II). *Science* **302**, 1894; author reply 1894, doi:10.1126/science.1089517 (2003).

205   Alavi, A., Hood, J. D., Frausto, R., Stupack, D. G. & Cheresh, D. A. Role of Raf in vascular protection from distinct apoptotic stimuli. *Science* **301**, 94-96, doi:10.1126/science.1082015 (2003).

206   Geng, L. *et al.* Inhibition of vascular endothelial growth factor receptor signaling leads to reversal of tumor resistance to radiotherapy. *Cancer research* **61**, 2413-2419 (2001).

207   Palmer, G. M. *et al.* In vivo optical molecular imaging and analysis in mice using dorsal window chamber models applied to hypoxia, vasculature and fluorescent reporters. *Nature protocols* **6**, 1355-1366, doi:10.1038/nprot.2011.349 (2011).

208   Sorg, B. S., Moeller, B. J., Donovan, O., Cao, Y. & Dewhirst, M. W. Hyperspectral imaging of hemoglobin saturation in tumor microvasculature and tumor hypoxia development. *Journal of biomedical optics* **10**, 44004, doi:10.1117/1.2003369 (2005).

209   Wang, X. *et al.* Statistical tracking of tree-like tubular structures with efficient branching detection in 3D medical image data. *Physics in medicine and biology* **57**, 5325-5342, doi:10.1088/0031-9155/57/16/5325 (2012).

210   Krissian, K., Malandain, G., Ayache, N., Vaillant, R. & Trousset, Y. Model-Based Detection of Tubular Structures in 3D Images. *Computer Vision and Image Understanding* **80**, 130-171, doi:http://dx.doi.org/10.1006/cviu.2000.0866 (2000).

211   Chanwimaluang, T. & Fan, G. in *Circuits and Systems, 2003. ISCAS'03. Proceedings of the 2003 International Symposium on.* V-21-V-24 vol. 25 (IEEE).

212   Estrada, R. *et al.* Exploratory Dijkstra forest based automatic vessel segmentation: applications in video indirect ophthalmoscopy (VIO). *Biomedical optics express* **3**, 327-339, doi:10.1364/BOE.3.000327 (2012).

213   Chaudhuri, S., Chatterjee, S., Katz, N., Nelson, M. & Goldbaum, M. Detection of blood vessels in retinal images using two-dimensional matched filters. *IEEE transactions on medical imaging* **8**, 263-269, doi:10.1109/42.34715 (1989).

214   Soares, J. V., Leandro, J. J., Cesar Junior, R. M., Jelinek, H. F. & Cree, M. J. Retinal vessel segmentation using the 2-D Gabor wavelet and supervised classification. *IEEE transactions on medical imaging* **25**, 1214-1222 (2006).

215   Frangi, A., Niessen, W., Vincken, K. & Viergever, M. Multiscale vessel enhancement filtering. *Medical Image Computing and Computer-Assisted Intervention—MICCAI'98*, 130-137 (1998).

216   Patel-Hett, S. & D'Amore, P. A. Signal transduction in vasculogenesis and developmental angiogenesis. *The International journal of developmental biology* **55**, 353-363, doi:10.1387/ijdb.103213sp (2011).

217   Kleinfeld, D., Mitra, P. P., Helmchen, F. & Denk, W. Fluctuations and stimulus-induced changes in blood flow observed in individual capillaries in layers 2 through 4 of rat neocortex. *Proceedings of the National Academy of Sciences of the United States of America* **95**, 15741-15746 (1998).

218   Behm, B., Babilas, P., Landthaler, M. & Schreml, S. Cytokines, chemokines and growth factors in wound healing. *Journal of the European Academy of Dermatology and Venereology : JEADV*, doi:10.1111/j.1468-3083.2011.04415.x (2011).

219   Bao, P. *et al.* The role of vascular endothelial growth factor in wound healing. *The Journal of surgical research* **153**, 347-358, doi:10.1016/j.jss.2008.04.023 (2009).

220   Langham, M. E., Farrell, R. A., O'Brien, V., Silver, D. M. & Schilder, P. Blood flow in the human eye. *Acta Ophthalmologica* **67**, 9-13, doi:10.1111/j.1755-3768.1989.tb07080.x (1989).

221   Pries, A. R. A versatile video image analysis system for microcirculatory research. *International journal of microcirculation, clinical and experimental / sponsored by the European Society for Microcirculation* **7**, 327-345 (1988).

222   Intaglietta, M., Silverman, N. R. & Tompkins, W. R. Capillary flow velocity measurements in vivo and in situ by television methods. *Microvascular research* **10**, 165-179 (1975).

223   Lindken, R., Rossi, M., Gro & Westerweel, J. Micro-Particle Image Velocimetry ([small micro]PIV): Recent developments, applications, and guidelines. *Lab on a Chip* **9**, 2551-2567 (2009).

224   Drew, P., Blinder, P., Cauwenberghs, G., Shih, A. & Kleinfeld, D. Rapid determination of particle velocity from space-time images using the Radon transform. *Journal of Computational Neuroscience* **29**, 5-11, doi:10.1007/s10827-009-0159-1 (2010).

225   Dobbe, J., Streekstra, G., Atasever, B., van Zijderveld, R. & Ince, C. Measurement of functional microcirculatory geometry and velocity distributions using automated image analysis. *Medical and Biological Engineering and Computing* **46**, 659-670, doi:10.1007/s11517-008-0349-4 (2008).

226   Japee, S. A., Pittman, R. N. & Ellis, C. G. Automated method for tracking individual red blood cells within capillaries to compute velocity and oxygen saturation. *Microcirculation* **12**, 507-515, doi:10.1080/10739680591003341 (2005).

227   Barretto, R. P. *et al.* Time-lapse imaging of disease progression in deep brain areas using fluorescence microendoscopy. *Nature medicine* **17**, 223-228, doi:10.1038/nm.2292 (2011).

228   Turner, J., Belch, J. J. F. & Khan, F. Current Concepts in Assessment of Microvascular Endothelial Function Using Laser Doppler Imaging and Iontophoresis. *Trends in Cardiovascular Medicine* **18**, 109-116, doi:10.1016/j.tcm.2008.02.001 (2008).

229   Koch, E., Walther, J. & Cuevas, M. Limits of Fourier domain Doppler-OCT at high velocities. *Sensors and Actuators A: Physical* **156**, 8-13, doi:10.1016/j.sna.2009.01.022 (2009).

230   Sudheendran, N., Syed, S. H., Dickinson, M. E., Larina, I. V. & Larin, K. V. Speckle variance OCT imaging of the vasculature in live mammalian embryos. *Laser Physics Letters* **8**, 247-252, doi:10.1002/lapl.201010120 (2011).

231   Varghese, H. J. *et al.* Mapping of the functional microcirculation in vital organs using contrast-enhanced in vivo video microscopy. *American journal of physiology. Heart and circulatory physiology* **288**, H185-193, doi:10.1152/ajpheart.01022.2003 (2005).

232   Pries, A. R. *et al.* Resistance to blood flow in microvessels in vivo. *Circulation research* **75**, 904-915 (1994).

233   Davis, M. J. Determination of volumetric flow in capillary tubes using an optical Doppler velocimeter. *Microvascular research* **34**, 223-230 (1987).

234   Pries, A. R. *et al.* Structural adaptation and heterogeneity of normal and tumor microvascular networks. *PLoS computational biology* **5**, e1000394, doi:10.1371/journal.pcbi.1000394 (2009).

235   Hanna, G. *et al.* Automated measurement of blood flow velocity and direction and hemoglobin oxygen saturation in the rat lung using intravital microscopy. *American journal of physiology. Lung cellular and molecular physiology* **304**, L86-91, doi:10.1152/ajplung.00178.2012 (2013).

236   Tolner, E. A. *et al.* Five percent CO(2) is a potent, fast-acting inhalation anticonvulsant. *Epilepsia* **52**, 104-114, doi:10.1111/j.1528-1167.2010.02731.x (2011).

237   Morgan, W. F. Non-targeted and delayed effects of exposure to ionizing radiation: II. Radiation-induced genomic instability and bystander effects in vivo, clastogenic factors and transgenerational effects. *Radiation research* **159**, 581-596 (2003).

238   Morgan, W. F. Non-targeted and delayed effects of exposure to ionizing radiation: I. Radiation-induced genomic instability and bystander effects in vitro. *Radiation research* **159**, 567-580 (2003).

239   Dayal, D., Martin, S. M., Limoli, C. L. & Spitz, D. R. Hydrogen peroxide mediates the radiation-induced mutator phenotype in mammalian cells. *The Biochemical journal* **413**, 185-191, doi:10.1042/BJ20071643 (2008).

240   Hei, T. K. *et al.* Mechanism of radiation-induced bystander effects: a unifying model. *The Journal of pharmacy and pharmacology* **60**, 943-950, doi:10.1211/jpp.60.8.0001 (2008).

241   Badea, C. T. *et al.* Computed tomography imaging of primary lung cancer in mice using a liposomal-iodinated contrast agent. *PloS one* **7**, e34496, doi:10.1371/journal.pone.0034496 (2012).

242   Chatni, M. R. *et al.* Tumor glucose metabolism imaged in vivo in small animals with whole-body photoacoustic computed tomography. *Journal of biomedical optics* **17**, 076012, doi:10.1117/1.JBO.17.7.076012 (2012).

243   Ahn, G. O. & Brown, J. M. Role of endothelial progenitors and other bone marrow-derived cells in the development of the tumor vasculature. *Angiogenesis* **12**, 159-164, doi:10.1007/s10456-009-9135-7 (2009).

Biography

Andrew Nicholas Fontanella was born August 26th, 1982, and lived in the towns of Chinchilla and Clarks Green in Northeastern Pennsylvania until the age of 18. Upon graduation from Abington Heights High School, he attended Pennsylvania State University at the University Park campus from 2000 to 2005, where he was awarded an NSF sponsored Research Experience for Undergraduates fellowship. He received his B.S. in electrical engineering in May of 2005.

Upon graduation, Andrew enrolled as a graduate student in the Electrical and Computer Engineering department at Duke University. He completed his core M.S. coursework in the fall of 2006 and joined the lab of Mark Dewhirst the following spring. In 2008 he received a three-year pre-doctoral fellowship from the Department of Defense Breast Cancer Research Program. He completed his doctoral research in 2013 and was awarded a M.S in Electrical and Computer Engineering and a Ph.D. in Biomedical Engineering later that year.

Publications:

1. Hanna G, Fontanella A, Palmer G, Shan S, Radiloff DR, Zhao Y, Irwin DC, Hamilton KL, Boico A, Piantadosi CA, Blueschke G, Dewhirst MW, McMahon TJ, Schroeder T. "Automated measurement of blood flow velocity and direction and hemoglobin oxygen saturation in the rat lung using intravital microscopy". *Am J Physiol Lung Cell Mol Physiol*. 2012 Nov 16. PMID: 23161885.
2. Palmer GM, Fontanella AN, Shan S, Dewhirst MW. "High-resolution in vivo imaging of fluorescent proteins using window chamber models". *Methods Mol Biol.* 2012;872:31-50. PMID: 22700402.

3. Turley RS, Fontanella AN, Padussis JC, Toshimitsu H, Tokuhisa Y, Cho EH, Hanna G, Beasley GM, Augustine CK, Dewhirst MW, Tyler DS. "Bevacizumab-induced alterations in vascular permeability and drug delivery: a novel approach to augment regional chemotherapy for in-transit melanoma". *Clin Cancer Res.* 2012 Jun 15;18(12):3328-39. PMID: 22496203.

4. Palmer GM, Fontanella AN, Shan S, Hanna G, Zhang G, Fraser CL, Dewhirst MW. "In vivo optical molecular imaging and analysis in mice using dorsal window chamber models applied to hypoxia, vasculature and fluorescent reporters". *Nat Protoc.* 2011 Aug 18;6(9):1355-66. PMID: 21886101

5. Palmer GM, Fontanella AN, Zhang G, Hanna G, Fraser CL, Dewhirst MW. "Optical imaging of tumor hypoxia dynamics". *J Biomed Opt.* 2010 Nov-Dec;15(6):066021. PMID: 21198195

6. Skala MC, Fontanella A, Lan L, Izatt JA, Dewhirst MW. "Longitudinal optical imaging of tumor metabolism and hemodynamics". *J Biomed Opt.* 2010 Jan-Feb;15(1):011112. PMID: 20210438

7. Skala MC, Fontanella A, Hendargo H, Dewhirst MW, Izatt JA. "Combined hyperspectral and spectral domain optical coherence tomography microscope for noninvasive hemodynamic imaging". *Opt Lett.* 2009 Feb 1;34(3):289-91. PMID: 19183634

8. Fontanella A, Cao Y, Dewhirst M, "Vascular Endothelial Growth Factor (VEGF) Receptors." *Combining targeted biological agents with radiotherapy: Current status and future direction.* William Small (Ed.). Demos Medical Publishing. 2008

Conference Presentations:

1. Dewhirst M, et al. "Vascular response to microbeam radiation therapy in vivo using a murine window chamber tumor model." *Medical physics* 39.6. 2012: 3983.

2. Rajaram N, et al. "Effect of cycling hypoxia on vascular oxygenation and tumor glycolytic demand in preclinical breast cancer models." *Era of Hope (EOH) 2011 Proceedings.* 2011: 280-281

3. Fontanella A, et al. "Serial in vivo analysis of microbeam radiation therapy." *Era of Hope (EOH) 2011 Proceedings.* 2011: 808

4. Fontanella A, et al., "An algorim for quantification of hemodynamic properties in murine dorsal window chamber video images." *FASEB J* 25. 2011: 350

5. Turley, R. S., et al. "Systemic bevacizumab synergistically augments regionally delivered chemotherapy for malignant melanoma." *Journal of Surgical Research* 165.2. 2011: 290-291.

6. Fontanella A, et al., "In vivo optical assessment of microbeam radiation therapy response." *Radiation Research Society 2010 Annual Meeting.* 2010

7. Oldham M, et al. "Imaging the biological structure and characteristics of model tumors using optical computed transmission and emission tomography." *Medical Physics* 37. 2010: 3405.

8. Skala M, et al. "Combined hyperspectral and optical coherence tomography microscope for non-invasive hemodynamic imaging." *Novel Techniques in Microscopy*. Optical Society of America. 2009

9. Fontanella A, et al., "Optical methods for the investigation of anti-angiogenic induced changes in oxygen transport." *Radiation Research Society 2008 Annual Meeting.* 2008